Fine scale distribution of precipitation in the Voss area

Master thesis in Meteorology

by
Marie Pontoppidan

June 5, 2015

UNIVERSITY OF BERGEN
GEOPHYSICAL INSTITUTE

Photo on the front page is taken at Sandfjellet towards N on August 18th, 2014. Convective cumulus clouds are influencing the fine scale precipitation distribution in the campaign area.

Abstract

The precipitation in Western Norway is strongly affected by its position in the mid latitude conveyor belt of synoptic systems. When the warm and moist air impinges on the complex mountainous terrain, large variabilities in local precipitation amounts arise. This master thesis has examined the orographic modifications of precipitation in an area around the city of Voss in Western Norway. To do so, two observational campaigns with HOBO rain gauges have been conducted, resulting in a valuable dataset for the area with high horizontal and temporal resolution.

The observed precipitation has been studied and large areal variability was detected. In the period May to November 2014 a synoptic scale difference of 114 % was found between Vasslii (674 mm) and Hisdalen (1443 mm), whereas a smaller mesoscale signal shows a total precipitation difference of up to 40 % on gauges located within a distance of 10 km.

Mainly during high wind situations, defined as 10 ms^{-1} or above, the fine scale distribution of precipitation has large inhomogeneities. During lower wind situations, below 6 ms^{-1}, the precipitation pattern seems to be more homogeneous, but with some variability at the coastal stations. Topography importance has been investigated and the effects of up- and downwind barriers in the vicinity are discussed.

The dataset has also been used for a model validation and sensitivity test for the period of the major flooding event in late October 2014. Large sensitivity was found for grid resolution whereas the spectral nudging settings and terrain smoothing had less influence on the reproduced precipitation. The best model option for this study, judging by RMSE, was found to be the option with 1 hour relaxation time, with nudging of wavelengths larger than 677 km zonally and 609 km meridionally and a grid resolution of 1 km. The optimized model set up was capable of representing the observed precipitation amounts rather well with respect to absolute values, timing of events and spatial variability, but further optimization is still needed for a satisfactory performance at some complex terrain areas.

A closer investigation of the flooding event has been performed, both observational data and model data from WRF have been examined. For precipitation distribution, large scale driving mechanisms as stability, humidity and the seeder feeder effect have been identified as important factors. Furthermore smaller scale features, with a horizontal scale of less than 5 km, e.g. gravity waves, small scale forced ascent and spill over effects were found to have a major influence on the variability of the precipitation.

i

Acknowledgments

I am very happy that the opportunity of writing a master thesis based on my curiosity on precipitation differences was possible. A special thank you to my main supervisor Joachim Reuder who helped and encouraged me to form a thesis around my own suggestions. I would also like to thank my co-supervisor Stephanie Mayer. It has been a pleasure to work with you, and I am very grateful for the encouragement you both provided during the past years. There has always been time for my questions and a good advice.

Many thanks also to Anak Bhandari for technical introduction to the rain gauges, to Marius Oppsanger Jonassen for Matlab help and support and to Erik Kolstad for WRF support. In addition I would like to thank all of you who allowed a piece of your garden to become research area for a while. This includes Klaus Müller, Asbjørn and Elbjørg Helle, Trond Olav Strømme, Nils and Eli Klette and Joachim Reuder.

This thesis had not been possible without the support from my family. Thank you to my lovely husband Jostein and my two boys, Matias and Nikolai and my father in law, Svein Døsen for joining me on some of my many field trips. And finally, but not least, my mother in law, Gunvor Døsen who has taken her share of childcare and housework when I couldn't find the time.

Finally a thank to my co-students at the Geophysical Institute for 5 years of hard work and joy. I hope to see you all graduate and do well.

Contents

List of Figures

List of Tables

Chapter 1

Introduction

Western Norway is located in the prevailing belt of mid latitude cyclones. Synoptic low pressure systems with associated fronts passes the area on a regular basis, typically only a few days apart. When approaching the west coast of Norway the air is usually relatively warm and moist after passing over the Atlantic Ocean. The forced ascent of the mild and humid air over the mountain ranges of Southern and Central Norway, causes high precipitation amounts, exceeding annual averages of 3000 mm in several places, in Western Norway (Met.no).

The upslope mountainous terrain, just inland of the coast, enhances the precipitation when the mild and moist airflow interacts with the topography. The terrain is very complex, with high mountains, valleys of different width and steepness, and a large amount of smaller scale hills. This causes high spatial variability in the precipitation, due to local orographic modification. This is confirmed by large differences between climatological means, e.g. for the official measurement stations at Kvamskogen with 3151 mm and Voss with 1280 mm (Met.no). The stations are both located in mountainous terrain at a distance of less than 40 km apart.

The interest in the weather is caused by its severe impact on our daily lives. Both on a day to day basis, but also under a more vital point of view. Inhabitants of Norway are in danger of experiencing natural hazards, as landslides, floodings and avalanches, every year. Human lives are lost, and the economical costs are high, both for authorities and individuals. Prominent examples from the very recent past are the main road between Bergen and Voss that was closed several times in 2014, and lately twice in May 2015, due to landslides, and a large flooding event in parts of Western Norway in October 2014. A 200 year flooding event which caused widespread flooding along the river Vosso, including a large part of the city of Voss and a factory at Evanger. Other areas again were isolated when their only roads were washed away. The flooding also completely removed 5 houses from their ground in Odda when the river Opo went past its riverbanks. Economical cost were high and the rebuilding has yet to be completed, but fortunately no human lives were lost.

For me though, the original curiosity in the topic was triggered by pleasure. During several years of gliding in the area I have observed fohn gaps, and often a wall of precipitation while approaching Dale when returning home to Osøyro. The cottage I own at Sandfjellet in the Voss area is bought because

of its dryer climate compared to e.g. Kvamskogen.

Several studies of orographic precipitation and the theory behind have been performed. During the last decade the focus was on developing conceptual models (Smith, 1979, 2003; Smith and Barstad, 2004; Colle, 2004; Roe, 2005) with focus on microphysical time delay factors (Smith, 2003) and how other parameters, i.e. moisture, stability and vertical shear, affects the orographic enhancement (Colle, 2004; Medina et al., 2005). In unblocked cases they found high correlations between the simple linear models and observed precipitation. But the correlation decreases significantly when blocking occurs, because of its non-linearity that cannot be included in the linear models (Hughes et al., 2009).

Numerical models like the Weather Research and Forecasting model (WRF) may improve insight beyond the linear models and have been tested against observation campaigns, e.g. the Mesoscale Alpine Program MAP (Jiang, 2003; Colle, 2004), Improvement of Microphysical Parametrization through Observational Verification Experiment IMPROVE (Stoelinga et al., 2003) and the Stord Orographic Precipitation Experiment STOPEX (Fagerlid, 2007; Reuder et al., 2007). The STOPEX experiment is of particular interest because it was performed on the island of Stord, southwest of this thesis' campaign area in 2005 (STOPEX I) and 2006 (STOPEX II). A clear orographic signal was found (Reuder et al., 2007). The island has similar ambient conditions and the same prevailing upper flow direction during precipitating events as the campaign area in this thesis. The STOPEX II data were compared to a WRF run with 3 km and 1 km resolution. The domain with the highest resolution performed best, but with an underprediction of the total precipitation. However the ability to reproduce correct intensity on shorter intervals showed a slight overprediction. The conclusion was that the overall results were satisfying for the 1 km resolution (Barstad and Caroletti, 2013).

Especially the WRF model is widely used for research and several studies of the preferred settings have been performed to increase the representation of precipitation (e.g. Omrani et al. (2015); Spero et al. (2014); Pérez et al. (2014); Glisan et al. (2013)). This includes the spectral nudging settings, a widely used technique to force the model towards the driving field. The studies have confirmed the increased model performance by the use of spectral nudging, but the variable settings are yet to be optimized for best result.

The main aim of this thesis was to investigate and increase the understanding of the spatial variability of precipitation in complex terrain. To do so an observational campaign involving HOBO rain gauges was launched in the complex terrain between Bergen and Voss. 5 rain gauges were installed during autumn 2013, and additionally 7 rain gauges were mounted the following spring. A total of 12 rain gauges were operational from May to November 2014. In addition the numerical model WRF has been tested regarding to its sensitivity to topography smoothing, grid resolution and spectral nudging settings. The model runs are analyzed for a four day period, including the major flooding event in Western Norway late October 2014. The model results are compared to the observational dataset collected in the campaign area. Based on 3D fields of the relevant parameters (i.e. humidity, temperature, horizontal and vertical wind) from the optimized simulation, a detailed investigation of processes important for precipitation modification in a complex terrain is performed.

The thesis is organized as follows: Chapter 2 describes the theory behind orographic precipitation and gives a short description of factors that may enhance the effect. Chapter 3 contains the description of

the HOBO rain gauge, the calibration tests and a presentation of the field campaigns. The numerical model WRF, used in this work, is described in Chapter 4 including the experimental set up. Results from the observational field campaign are presented and discussed in Chapter 5. A sensitivity analysis of WRF with respect to topography smoothing, spectral nudging and grid resolution is presented in Chapter 6. The chapter also includes a case study of the flooding event of October 2014, based on the WRF simulations with the optimized setup. Finally a short summary and outlook is given in Chapter 7.

Chapter 2

Theory

2.1 Precipitation

An air parcel's capacity to adhere water vapor is essential for cloud and precipitation formation. Cloud and droplet formation is induced when partial water vapor pressure (e) reaches its saturation level (e_s). The saturation water vapor pressure is a function of temperature, and the equation of Claysius Clayperon states this dependency

$$\frac{de_s}{dT} = \frac{Le_s}{R_v T^2} \tag{2.1}$$

where R_v is the gas constant for water vapor and L is the latent heat. For temperatures in the range of $-35°C$ to $+35°C$ an approximation of e_s is given by (Roe, 2005)

$$e_s(T) = 6.112 hPa * exp\left(\frac{17.67 * T}{T + 243.5}\right) \tag{2.2}$$

The saturated water vapor pressure e_s is closely connected to the saturated specific humidity q_s. In the range of the atmospheric temperature it is given by

$$q_s(T, z) = 0.622 * \frac{e_s(T)}{p(z)} \tag{2.3}$$

where the assumption of $p >> e_s$ is applied. It follows from equation 2.3 that the saturated specific humidity is a function of temperature and pressure, and the adiabatic lifting of an air parcel therefore strongly influences this parameter. The rate of change of the saturated specific humidity is closely connected to the condensation rate. When saturation is reached, further increase in humidity leads to increased condensation rather than increased saturation, since the atmospheric saturation level rarely exceed 102% (Rogers and Yau, 1989). The rate of saturated specific humidity change is estimated by Roe (2005) as

$$C = -\frac{d(\rho q_s)}{dt} \simeq -\frac{\partial(\rho q_s)}{\partial z}\frac{dz}{dt} = -w\frac{\partial(\rho q_s)}{\partial z} \tag{2.4}$$

where ρq_s is the mass of the water vapor and w is the vertical velocity of the air parcel. From equation 2.4 it is clear that the vertical velocity of an air parcel, forced by e.g. orography, affects the condensation rate. The following reaction of the vertical parcel movement depends on multiple factors, e.g. the atmospheric stability, the barrier size and the flow velocity. A more thorough description of these parameters can be found in Section 2.2.

2.1.1 Droplet formation

When air masses rise and expand adiabatically, the pressure drops and the parcel cools. The specific humidity will eventually reach saturation and nucleation processes start. Homogeneous nucleation formation forms by diffusion of the water vapor itself, without any cloud condensation nuclei. Heterogeneous formation on the other hand, takes place when hydrometeors form on cloud condensation nuclei or ice nuclei. Homogeneous nucleation requires saturation levels of several 100 % which are not observed in the atmosphere. Therefore almost all hydrometeor formation is assumed to be from heterogeneous formation (Rogers and Yau, 1989).

Some hydrometeors reach their critical radius for droplet activation, dependent on the saturation level, and start to grow. Initially mainly by diffusion, but as the droplets grow larger, coalescence and collision effects increases and eventually dominate the droplet growth. In cold clouds i.e. clouds with temperature lower than the freezing point, water and ice particles can co-exist, allowing ice particles to grow at the expense of water droplets. This is due to the difference in saturation pressure for ice and water, the Bergeron-Findeisen effect (Rogers and Yau, 1989). After an ice particle reaches a certain size, and thus a considerable vertical velocity, riming, deposition and aggregation dominate the crystal growth.

As the hydrometeor sizes increase, the fall speed of the hydrometeors becomes so large that the updrafts are insufficient to keep them inside the cloud. Evaporation takes place outside the cloud where the partial water vapor pressure is lower, and eventually the non-evaporated part of the hydrometeors reach the ground as precipitation. In cumulus clouds precipitation can form and fall to the ground in only 20 minutes on a favorable day, for stratiform clouds the corresponding timescales are longer.

2.2 Orographic precipitation

An air parcels vertical motion over a barrier causes additional condensation on the ascending hill side. When the background water vapor pressure is near saturation, this condensation enhancement leads to increased precipitation due to topography. We classify this as orographic enhanced precipitation. Many effects contribute to orographic precipitation and studies the past decades have increased our knowledge level significantly. To simplify, Smith (1979) classified the orographic precipitation in 3 main categories: Large scale upslope precipitation, seeder-feeder effects and convective situations. In Smith (1989) the convective class was further split into diurnal convective development and triggering of potentially unstable air parcels. This classification however, is rather artificial and simplified.

Recent reviews (e.g. Roe (2005); Houze Jr. (2012)) summarize with a less strict classification. The fundamental factors and some basic processes are described in the following paragraphs, a thorough description can be found in Houze Jr. (2012).

2.2.1 Fundamental factors

Barrier size and microphysics time scale

The barrier profiles and microphysical time scales are important for the lateral precipitation distribution. The microphysical processes, during cloud and hydrometeor formation, suggest a time delay on the precipitation formation and fall out. Smith (2003) includes this by parameterization of a cloud- and fall out time delay factor τ_c and τ_f, often combined as one time delay parameter τ. Increasing τ increases the advection distance of the hydrometeors and thereby shifts the precipitation pattern downstream towards the hilltop. For low narrow hills, this may enhance precipitation on the downhill side, i.e. the spill over effect (e.g. Barstad and Smith (2005)). For larger mountains the spillover effect is expected to be minimal. An evaluation of the linear model of Smith and Barstad (2004) were done by Barstad and Smith (2005). It showed a precipitation shift downstream when increasing τ, but also a decrease in amplitude compared to the original raw upslope model. The model tests corresponded well with the compared observational campaigns.

On a climatological time scale Pavelsky et al. (2012) confirms the importance of the time delay factor from Smith and Barstad (2004) by research into the effect of an earlier snow melting in the Sierra Nevada mountains. As a consequence of the global warming it is expected that snow will be replaced by rain in this area. The effects on fall speed of hydrometeors, in particular on the fall out time, changes the distribution of precipitation dramatically.

Dynamical flow

Whether an air parcel is blocked by topography or remains unblocked is a major factor for the lateral precipitation distribution. The linear model from Smith (2003) does not include the non-linear blocking and shows low correlation for the events where blocking is dominant (Hughes et al., 2009). A way of diagnosing whether an airflow is prone to be blocked or not, is by calculating the non dimensional mountain height

$$M = \frac{NH}{U} = \frac{1}{Fr} \tag{2.5}$$

where U is the upstream main flow, N is the Brunt-Vaisala frequency and H is the barrier height, Fr is the Froude number known from fluid dynamics. For a high M, i.e. $M > 1.7$ the flow tend to be blocked whereas a lower M, i.e. $M < 1.4$ favor an unblocked flow (Jiang, 2003). Typical values in the campaign area are $H = 1000$ m and $N = 0.01$ s^{-1}. A rough estimate indicates blocking for $U \leq 6$ ms^{-1} and unblocked events for $U \geq 7$ ms^{-1}. Wind speeds observed during precipitation events in the campaign period indicate that both blocked and unblocked events have been present.

When blocking occurs the air piles up ahead of the mountain. The incoming air is forced above and the parcel ascent starts well ahead of the mountain. This moves the enhanced precipitation pattern

further upstream. The air pocket on the upwind side of the mountain also enhances vertical wind shear. The shear may induce turbulent overturning in the shear layer, which produce small areas of increased liquid water content (LWC). Consequently hydrometeors grow quicker and the time delay factor introduced by Smith (2003) is reduced, creating small regions of enhanced precipitation (Houze Jr., 2012).

Thermodynamics

Moisture in the lower layers decreases the density and therefore destabilizes the flow. In the linear model (Smith, 2003), assuming a dry atmosphere, this effect is not considered. The implementation of moisture decreases the critical mountain height M compared to the dry cases, and thereby imposes a strong delay in blocking events (Jiang, 2003). However modeling the moist cases causes challenges for simple models, since the moist Brunt-Vaisala frequency N_m, varies strongly both vertically and horizontally and the choice of a representative N_m for a larger area is very challenging (Jiang, 2003).

2.2.2   Basic processes

It is evident that the fundamental factors described above influence the orographic precipitation in the vicinity of a terrain barrier. In spite of the complexity, extensive research has enabled the identification of basic structures that affect precipitation in mountainous terrain. Processes relevant for this assignment are shortly described below, a detailed description can be found e.g. in Roe (2005); Houze Jr. (2012).

Smooth forced ascent

Stable flow towards a barrier, larger or minor, forces laminar flow over the mountain. On the windward side the positive vertical perturbation enhances condensation and produces or strengthens a cloud, leading to possibly increased precipitation. On the lee side evaporation is enhanced by negative vertical motion, fohn gaps may appear if the air parcel humidity reduces sufficiently. This may happen in isolated cases or possibly embedded in frontal systems.

The cross barrier flow may also trigger gravity waves in stable conditions. If the gravity waves are trapped, the waves tilt upstream with height, and thereby shifts the region of upward motion further upstream. The enhanced precipitation area is correspondingly forced upstream. Additionally the gravity waves force downward motion aloft near the mountain crest, which seeds hydrometeors into the moist lower layer. The hydrometeors ensure faster growth in a lower cloud. This seeder-feeder effect was first mentioned by Bergeron in 1965.

Convection triggered by forced ascent

Potentially unstable air masses may be lifted by forced ascent to the level of free convection. In deep moist layers this results in large cumulus nimbus clouds, whereas in a shallow moist layer the convective clouds may be embedded. In both cases enhanced heavy precipitation is a likely result upwind of the barrier (Houze Jr., 2012). The convective triggering was found to be the case in approximately 50%

of the rain events in the STOPEX II campaign which took place in Norway in 2006 (Barstad and Caroletti, 2013).

Diurnally forced convection

Orographic controlled convective clouds favor to form slightly shifted downwind on mountain plateaus and valley sides. Night time convective storms are not common in the campaign area. Because of the limited lateral resolution, rain gauge measurements are not very useful to study this phenomenon. The assignment will not be concentrated on this, but it is mentioned here since the summer months of the campaign 2014 were highly affected by convective events. For readers interested in the subject, an observational campaign specifically dedicated to diurnal forced convection, the Convective and Orographically-induced Precipitation Study (COPS), took place in the summer of 2007 (Wulfmeyer et al., 2011).

Chapter 3

Instrumentation and measurements

3.1 HOBO RG2-M rain gauge

3.1.1 Technical description

The rain gauge used in this field campaign is the HOBO-RG2-M. It is a tipping bucket type rainfall collector, including a battery driven event data logger. The gauge is designed with a collector screen on top, to avoid debris to contaminate and clog the orifice. The catch area is circular and has a diameter of 15.4 cm, resulting in a collection area of 186.3 cm^2. A funnel guides the precipitation into the tipping buckets. The bucket tips for every 0.2 mm of precipitation, and a magnetic switch actuates so the logger record the corresponding date and time. The logger records 8000 tips, i.e. 1600 mm of precipitation, before it starts to override previous timestamps. The accuracy is highly dependent on level mounting. If mounted in level, the accuracy given by the manufacturer is $\pm$ 2.0% (Onset, 2001) up to a maximum precipitation rate of 20 mm hour^{-1}. An experiment conducted by Skjerdal (2009) has verified this accuracy of the rain gauges. The protective screen on top of the funnel, can cause splash and wetting errors (See details in Section 3.2). For accurate measurement in low precipitation conditions the manufacturer recommends to remove the screen. The low rain rate discrepancy has been investigated by Sulen (2009) who compared the HOBO rain gauges with the gauge used by the Norwegian Meteorological Institute (Met.no) at Bergen Florida. This study shows that discrepancies occur, but mainly at low rain intensities. The HOBO rain gauge is not heated and is therefore limited to liquid precipitation sampling for reliable data. This is the reason that both measurement periods in this master project have been confined to snow-free situations.

3.1.2 Calibration of HOBO rain gauge

Before mounting in the field, a calibration check was performed on each rain gauge in the basement of the Geophysical Institute (GFI) in Bergen. Exactly 373 ml of water were filled into a container

with a flow controller in the bottom. The controller was regulated to a flow that corresponded to a tipping interval of minimum 36 s, simulating a rain rate of 20 mm hour^{-1} or below. The 373 ml of water should correspond to 100 ± 2 tips, but in reality the variation was greater. Rain gauge (20806) was calibrated again due to long run through time. The second calibration showed similar results with lower run trough time. Rain gauge number 21073 was calibrated in Hagavik with a different flow controller. A replacement gauge was needed due to a malfunction of logger 20818 during the field campaign.

After the field campaign a recalibration check was performed, and for rain gauges within the accuracy of $\pm$ 2 tips, given by the manufactor, an average correction factor was calculated by

$$CF = \frac{\frac{100}{p} + \frac{100}{k}}{2} \tag{3.1}$$

where CF is the correction factor, p is the number of tips before the campaign, and k is the number of tips after the campaign. For rain gauges with larger discrepancies a second calibration was performed. If discrepancies were persistent, a linear gradual change were assumed, and the data were corrected using the following formula

$$CF = \frac{100}{p} + \frac{\frac{100}{k} - \frac{100}{p}}{t_{tot}} * t \tag{3.2}$$

where t_{tot} refer to the total hours of operational time of the rain gauge and t refers to the hour of the data corrected. In both cases an average of multiple calibrations have been used for p and k if applicable.

Table 3.1: Calibration test of HOBO rain gauge RG2-M.

Serial #	Test Date	Tips before	Time before	Tips after	Time after
21077	20.03-14	98	1h 01m	91,92	1h 02m,1h 18m
20821	24.03-14	96	1h 12m	92,92	1h 17m,1h 20m
20818	24.03-14	96	1h 33m	none	none
20857	23.04-14	96	1h 15m	100	1h 05m
20805	23.04-14	100	1h 30m	94,93	1h 42m,0h 52m
21058	23.04-14	97	0h 56m	98	1h 27m
21072	23.04-14	97	1h 27m	90,90	1h 42m,1h 29m
21074	23.04-14	100	1h 28m	91,90	1h 22m,2h 03m
20806	24.04-14	98,95	2h 06m,1h 30m	90,91	1h 02m,1h 14m
20820	24.04-14	100	1h 02m	101	1h 17m
21076	24.04-14	98	1h 08m	98	1h 36m
21078	24.04-14	99	1h 34m	96	1h 03m
21073	29.07-14	95	1h 08m	97	1h 42m

3.2   Known errors of precipitation measurement

The wind speed, at the level of the gauge, has a large impact on the accuracy of precipitation measurement. Instrument induced turbulence and flow disturbances can deflect hydrometeors around the collector, therefore gauges in general have increasing undercatch with increasing wind speed (Nešpor and Sevruk, 1999). In addition to the wind induced flow disturbance, the efficient catch area is also affected. If the wind speed is neglectable, the catch area is circular. But when wind velocity increases, the angle α, between the horizontal collector area and the trajectory of the falling rain drop, decreases. The efficient catch area becomes oval and is reduced by a factor of $\sin(\alpha)$. The wind effect on HOBO rain gauges was investigated in a small scale study by Sulen (2009). It revealed undercatch in the order of 20-50% for wind speeds in the range of 5-10 ms^{-1} and 50-80% for 10-15 ms^{-1} wind. The magnitude of the wind induced error for the HOBO rain gauges, is comparable to other types of rain gauges previously investigated by the World Meteorological Organization(WMO) (Sulen, 2009; Sevruk et al., 2009; Mekonnen et al., 2014). During solid precipitation events the fall speed of the snow is reduced significantly compared to liquid droplets. This increases the wind induced errors considerably. Effective collection rates can be as low as 20% (Rogers and Yau, 1989).

A strong correlation exist between the wind speed and the catchment of the precipitation gauge. It is therefore important to place the gauge in a suitable area in the field. Some wind shield is desirable, but not so close that it affects the catch area. Field campaigns including several rain gauges are prone to a placement error due to different ambient surroundings of the gauges. The placement error induced can be reduced by installing the rain gauges in similar areas whenever possible.

Depending on the type of precipitation gauge, other errors can have large impact as well. Evaporation losses can be significant if the exposed water surface is large. The protective screen on the HOBO rain gauge increases the water surface and the evaporation losses, compared to the removed screen scenario. The removal of the screen will increase the risk of funnel contamination though. Because of the placement of the field stations in this campaign the increased risk of contamination was considered too large to remove the screen.

At high precipitation rates when droplet sizes are large, some droplets hitting inside the catch area may be splashed outside again. To avoid this, the gauge can be designed with steeper funnel and larger vertical sides. This however may increase the wind induced error and increases the wetting, where some water sticks to the inside, without reaching the measuring device itself. The wetting error is at the largest at a low rain intensity, but can be reduced with rain repellent coating in the collection area (Habib et al., 2010).

Two main correction methods for precipitation sampling have been suggested. One using an empirical correction formula, where average wind speed is the only parameter. The other is to use fluid dynamic simulations to approach a numerical correction formula, which have variables for wind speed, droplet size and rain intensity. The major advantage of the numerical method is that it can be used on the smallest time scale where rain rate is obtained, whereas the empirical formulas are designed for longer temporal scales as hourly to monthly averaged values (Habib et al., 2010). None of these corrections methods have been used in the field campaign due to a lack of reliable wind data at the sites. However

we estimate the error to be minor, due to the carefull placement in shielded areas.

Even after considering all these known errors the conclusion is that rain gauges still are the most accurate point measurement method for rain fall. It is inexpensive, simple to operate and gives a fairly accurate low cost dataset (Habib et al., 2010). The largest error in the field campaign is estimated to be wind induced, but care was taken during the station placements to reduce this error. Therefore an overall uncertainty in precipitation amounts for the field campaign is estimated to be in the order of 10-15%.

3.3   Field campaign descriptions

The pre campaign took place during autumn 2013. 5 HOBO rain gauges (P7-P11) were placed in the terrain around Voss. The purpose was to study the fine scale precipitation distribution in the Voss area. The field station areas were selected where one would expect variability in precipitation due to an orographic influence. The pre campaign showed interesting features, so the main campaign was launched in the same area in May 2014. Additionally a transect towards the W-SW was selected to investigate the mesoscale precipitation reaching the fine scale area. The direction selected is the prevailing wind direction during precipitation events in the area. The main campaign included 12 rain gauges, 5 stations at the same locations as during the pre campaign, and 7 in additional areas. The exact location of the stations is given in Figure 3.1 and Table 3.2. Pictures of the gauges in the terrain can be seen in Figure 3.2. In the field the rain gauges were mounted on a mast approximately 1 m above ground. Similar station areas were preferred to minimize the placement error by having comparable ambient conditions.

To optimize the campaign lenghts, nearby field observations from met.no mountainous stations, as Kvamskogen (455 amsl) and Øvstedal (316 amsl) have been consulted. The concern was to ensure positive ambient temperatures and precipitation in liquid form during precipitation events. The pre campaign started the 2nd of September 2013 and ended on the 1st of November. At the proceeding day, November the 2nd, snow was observed at the gauge at Sandfjellet. Øvstedal and Kvamskogen also reported snow and snow depth on the 2nd of November. To avoid contaminated data, no data after these events were used, and the gauges were dismounted a week later. For the main campaign in 2014 data were used from the 25th of May at 12 UTC until 16th of November at 00 UTC for the same reasons.

Table 3.2: HOBO rain gauges, stations with details.

Identity	Name	Lat	Long	Altitude	Serial number
P1	Hagavik	60°10.568′N	005°24.159′E	48 m	20806
P2	Nesttun	60°19.164′N	005°22.358′E	58 m	20857
P3	Hisdalen	60°23.829′N	005°41.389′E	140 m	21078
P4	Dale	60°35.362′N	005°49.756′E	91 m	21074
P5	Kaldestad	60°33.230′N	006°01.074′E	521 m	21058
P6	Evanger	60°38.821′N	006°06.623′E	27 m	20820
P7	Steine	60°40.039′N	006°11.991′E	485 m	21073
P8	Sandfjellet	60°36.422′N	006°12.696′E	620 m	20821
P9	Hodnaberg	60°33.638′N	006°12.811′E	618 m	21077
P10	Dyrvedalen	60°39.180′N	006°20.126′E	355 m	21076
P11	Flyane	60°36.112′N	006°19.128′E	436 m	20805
P12	Vasslii, Voss	60°38.671′N	006°26.681′E	79 m	21072

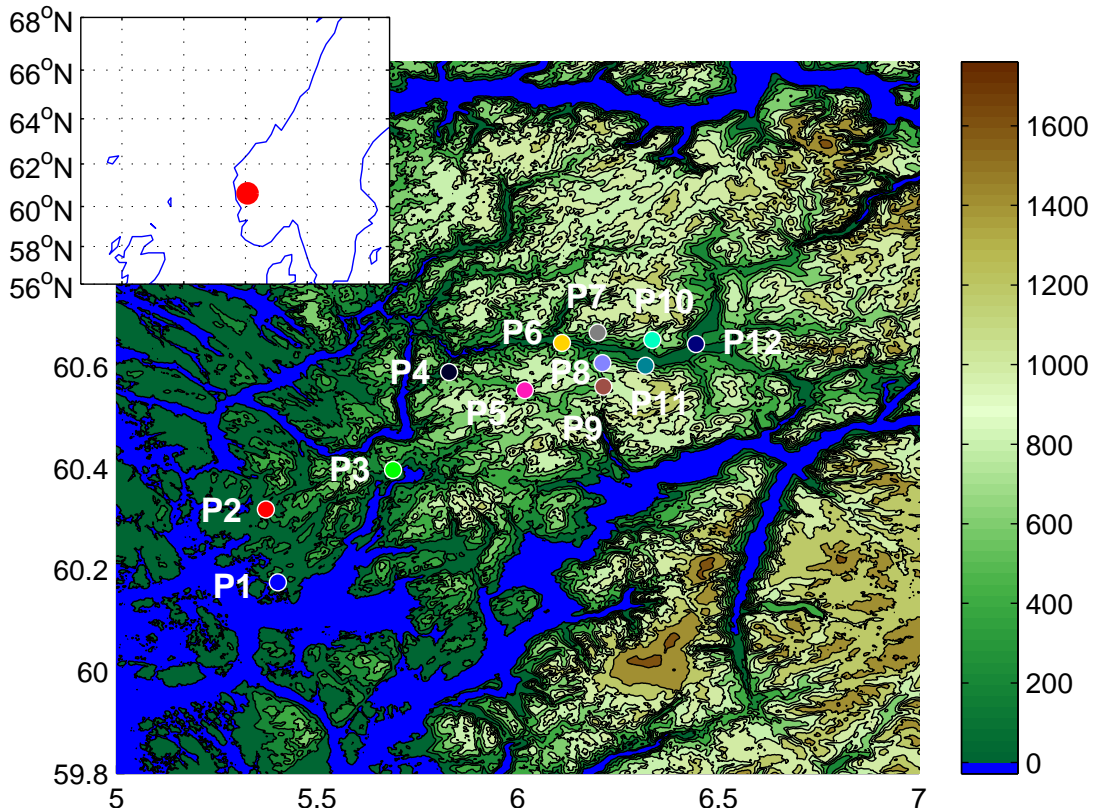Figure 3.1: Map with exact locations of the stations in the campaign. Overview map in the upper left corner, and a detailed map of the experiment area on the Norwegian west coast in the right for the exact locations and identifiers of the HOBO rain gauges.

(a) P1 Hagavik.

(b) P2 Nesttun.

(c) P3 Hisdalen, photo Klaus Müller.

(d) P4 Dale.

(e) P5 Kaldestad.

(f) P6 Evanger.

Figure 3.2: Stations P1-P6 in the terrain.

(g) P7 Steine.

(h) P8 Sandfjellet, assistent Nikolai Pontoppidan.

(i) P9 Hodnaberg.

(j) P10 Dyrvedalen, assistents J. & S. Døsen.

(k) P11 Flyane.

(l) P12 Vasslii.

Figure 3.2: Stations P7-P12 in the terrain.

3.4   Data processing

Data processing is an important part of a research project. To be able to reproduce the results shown in this thesis, the data process is described in this section.

The observational data were downloaded from the HOBO rain gauge via a shuttle in the field. The shuttle data were transferred to a PC via the BoxCar Pro program provided by Onset. A data reading routine has been programmed in Matlab to prepose the data for further analysis. As an initial step the correction factor described in Section 3.1 has been applied to the raw data. The precipitation data have been integrated over one hour and six hours (00-06 UTC, 06-12 UTC, 12-18 UTC and 18-24 UTC). The time stamp of the integrated data has been set to the end of the summation period. Data from the station at Steine is missing until the 30th of July at 18 UTC and is replaced with NaN's in the calculations. Likewise for the datalogger at Evanger, which ran out of battery the 13th of October after 18 UTC.

Chapter 4

Weather Research and Forecasting model
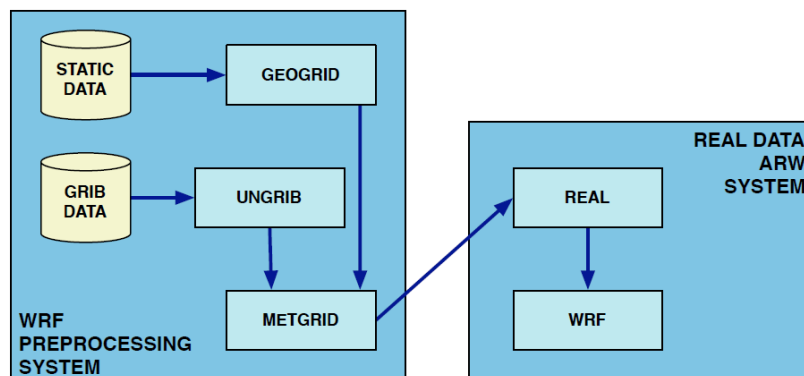
4.1   Description

Figure 4.1: Schematic view of the WRF Preprossesing System (WPS) and Advanced Research WRF (ARW) solver in the WRF model (Skamarock et al., 2008).

The Weather Research and Forecasting (WRF) model is a numerical atmospheric model applicable for both operational weather forecasting and case study based atmospheric research. It is well established and widely used for atmospheric research throughout the world. The development has been a multi agency corporation and its multiple physics and dynamics options are a result of the large scientific community using the model. A simplified schematic of the model is shown in Figure 4.1. The system consists of the WRF Preprosesing System (WPS) and the Advanced Research WRF (ARW) solver. The following chapter describes some of the main features in the model, more thorough descriptions may be found in Skamarock et al. (2008).

4.1.1 Governing equations

The Advanced Research WRF (ARW) solver uses the fully compressible non-hydrostatic Euler equations. They include complete curvature and coriolis terms and are presented in flux form with variables that have conserving properties. The linearly perturbed version of the governing equations are used as input for the ARW solver. The perturbation is done to reduce truncation errors in the horizontal pressure gradient and to reduce machine round-off errors in the vertical pressure gradient and buoyancy terms. The vertical coordinate is denoted by η and is similar to the terrain following hydrostatic-pressure σ coordinate, which is widely used in atmospheric models. It values from 1 at the surface to 0 at the upper boundary of the model domain and is defined as

$$\eta = \frac{p_h - p_{ht}}{p_{hs} - p_{ht}} \tag{4.1}$$

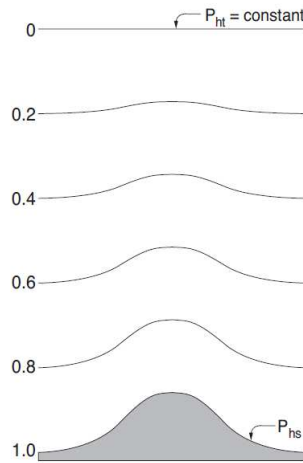where p_h is the hydrostatic pressure, and p_{ht}, p_{hs} refers to the top and surface values respectively.

Figure 4.2: Vertical coordinate η in the ARW solver (Skamarock et al., 2008).

4.1.2 Temporal discretization

The time integration in the ARW is realized by a time-split integration scheme. The meteorological modes use the 3. order Runge Kutta scheme. The gravity waves and the faster propagating horizontal acoustic modes are integrated using an implicit forward-backward scheme to avoid instability. Vertical buoyancy oscillations and acoustic modes are integrated using a vertically implicit scheme. The fast propagating modes are included in the Runge Kutta integration scheme in the form of a correction.
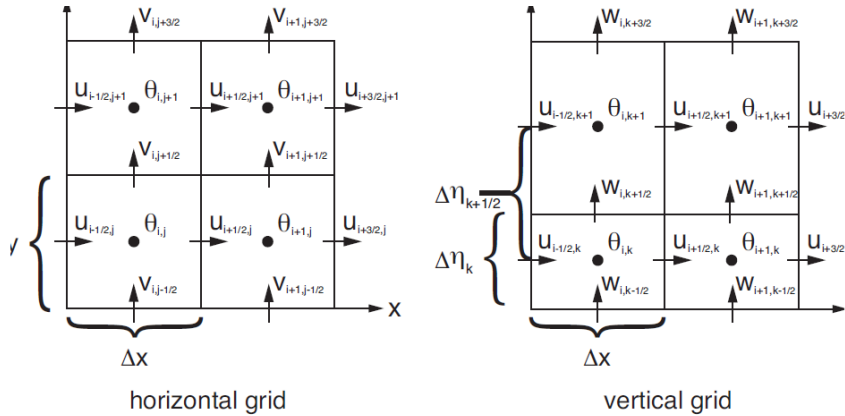
Figure 4.3: Horizontal and vertical Arakawa C grids as used in the ARW solver (Skamarock et al., 2008).

4.1.3 Spatial discretization

Spatial discretization in the ARW is realized by the Arakawa C grid. This implies that the thermodynamic variables are located in the mass points (i, j) in the center of a grid cell, whereas the velocity variables are located on the grid boarders in the points labeled u, v and w. These are staggered one-half grid cell from the mass points as shown in Figure 4.3. Geopotential ϕ, defined in w points, moisture q_m and column mass μ both defined in the mass points, are not shown on Figure 4.3. Diagnostic variables, such as pressure p and inverse density α, are also computed in the mass points on the grid. The main advantage of using grid staggering is that the time step of the model can be increased, without violating the stability criteria.

4.1.4 WRF preprocessor system

To prepare the model for operation it includes a preprocessor system (WPS). In the governing namelist file the physical grids are defined, this include projection, location on the globe, number and grid resolutions and nesting domains if applicable. Real meteorological input data can be used to create the initial- and lateral boundary conditions. A 3-step process makes the grid and data ready for the ARW solver. First the static terrestrial field is interpolated onto the defined grid. Next the external meteorological data is reformatted to a WRF intermediate format, and finally the data is interpolated to the grid setup. The output is a series of snap shots of the 3 dimensional state of the atmosphere for the selected time slides, including variables as temperature, relative humidity and the horizontal components of momentum. It also includes the 2 dimensional static fields and 2 dimensional time dependent fields, such as surface and sea-level pressure, layers of soil temperature and soil moisture, snow depth, skin temperature and sea surface temperature.
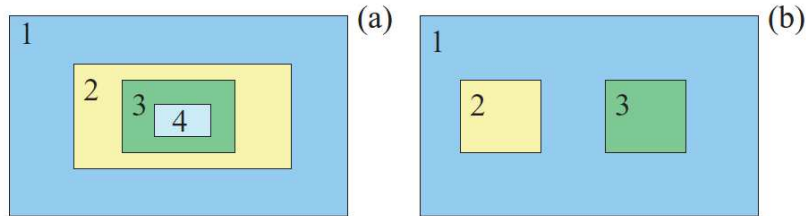
4.1.5 Nested domains

Figure 4.4: Possible options for nesting in the ARW solver. Either downscaling with nest as parent, or several nests with same parent domain (Skamarock et al., 2008).

Increased horizontal resolution is possible by introducing nests. Selected rectangular areas inside the parent domain can be run with higher spatial resolutions and correspondingly shorter time steps. Further downscaling is possible trough defining several nests, using the coarser nests as parents for finer grids as depicted in Figure 4.4a. Another nesting option is to define several areas of focus which have the same parent domain as depicted in Figure 4.4b. Nesting in the ARW solver can be either one way or two way, it refers to how the coarse and the finer grid interacts. For one way nesting the interaction is only through the interpolation of the coarse grid to the finer grid creating boundary conditions, whereas the two way nesting includes feedback from the finer grid to the coarse grid. Moving nests is also an option in the ARW solver, useful for e.g. tracking of storms or other moving features of interest. In this study the first option described in Figure 4.4a is used.

4.1.6 Boundary conditions

For the specified boundary option the ARW solver creates a boundary file. In the file four lateral boundaries are specified, defined as N, S, E and W of the parent domain. The variables included in the file are u, v, θ, q_v, ϕ' and μ'_d. Each variable has an initial term valid at the specific time, and a tendency term towards the next time step boundary condition. To avoid discontinuities in the boundaries a relaxation zone can be specified. In Figure 4.5 the outermost grid row and column are defined solely by interpolation from the external model. The next four grid rows and columns are the relaxation zone where the model is nudged towards the coarser grid environment. The size of the relaxation zone is a run time option specified in the namelist.input file. Boundary conditions for nested domains are interpolated from their respective parent domains. In addition to variables included in the coarse boundary condition, these also include microphysical variables. The specified rows and columns behave similar as for the coarse domain, for nests however the relaxation zone is not active. As an alternative a high resolution external dataset can be implemented as boundary conditions for nested domains.
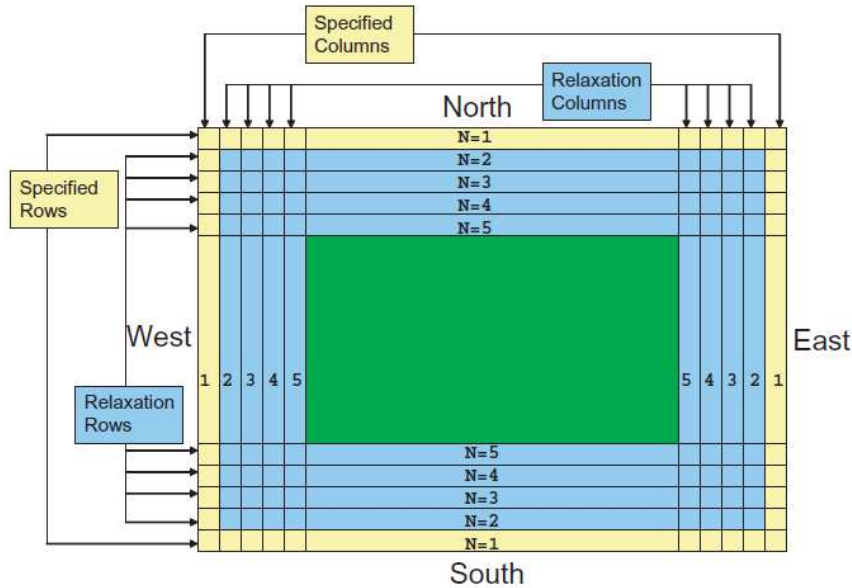
Figure 4.5: One specified row and column entirely from interpolation of external model and four relaxation rows and columns (Skamarock et al., 2008).

4.1.7 Parameterization

The grid size limits in general which physical processes in the atmosphere that can be solved explicitly in a simulation. Features that are not solved explicitly have to be included by parameterizations. The ARW solver includes five physical categories. The schemes are:

- Microphysics
- Long- and shortwave radiation
- Planetary boundary layer (PBL)
- Land surface model
- Cumulus convection

Common for all parameterization schemes in WRF is that each grid column is treated individually, i.e. there is no transfer of information between grid cells (Skamarock et al., 2008). Below is a short description of the parameterization schemes used in this study, a more detailed overview of the available schemes can be found in Skamarock et al. (2008).

Microphysics scheme

The Thompson scheme (Thompson, 2004; Thompson et al., 2008) is a bulk microphysical parameterization (BMP) scheme which explicitly predicts 5 mixing ratios for cloud water, cloud ice, rain, snow and graupel. As a second moment it also predicts the number of cloud ice concentration. Most BMP's parameterize snow as spherical, whereas this scheme assumes snow as fractal-like aggregated

crystals. This approach correlates better with observational studies (Thompson et al., 2008). Unique in this scheme is that the rain size distribution shifts depending on whether the rain originates from melted snow or warm rain created by collision and coalescence processes. This improves the classical Marshall-Palmer distribution which tends to make the fall speed too large when the snow starts melting (Thompson et al., 2008). By the use of look up tables the Thompson scheme also incorporates much more sophisticated techniques normally only found in spectral and bin parameterization schemes. These features, combined with relatively low computational demands compared to the more sophisticated bin schemes, make the Thompson scheme one of the widely used microphysical parameterization schemes, in particular for studies on orographic precipitation influenced by complex terrain (e.g. Nugent et al. (2014); Pérez et al. (2014); Weckwerth et al. (2014); Barstad and Caroletti (2013)).

Radiation scheme

For long wave radiation the rapid radiation transfer model (RRTM) (Mlawer et al., 1997) has been used. The model divides the long wave radiation into spectral bands. The molecular species treated in the model are water vapor, carbon dioxide, ozone, methane, nitrous oxide and halocarbons (Mlawer et al., 1997).

The short wave radiation scheme Dudhia (Dudhia, 1989) is based on a simple downward integration of the radiation flux. It is dependent on solar zenith angle and the values for albedo and absorption in clouds are incorporated from a look up table. Clear air water vapor absorption is based on a similar integrated-difference calculation, while the clear air scattering is set to be uniform in the atmosphere, proportional to the mass path length (Dudhia, 1989).

Planetary boundary layer scheme

Turbulence in the planetary boundary layer and in the free atmosphere is represented by the MYJ scheme (Mellor and Yamada, 1982; Janjic, 2002). The scheme is a nonsingular implementation of the Mellor-Yamaha Level 2.5 turbulence closure model (Mellor and Yamada, 1982). An upper limit dependent on turbulent kinetic energy, buoyancy and shear is imposed on the master length scale. This ensures a representative depth, dependent on the stability of the boundary layer. The PBL scheme is tied together with the Eta surface layer scheme which includes parameterizations for a viscous sub-layer. The surface fluxes are calculated iteratively with the use of variable roughness heights for humidity and temperature (Janjic, 2002; Skamarock et al., 2008).

Land surface model

The land surface model (Noah LSM) is a 4 layer soil temperature and moisture model, reaching a total soil depth of 2 meters. The inputs are from other parameterizations schemes as radiation, precipitation from the microphysics and convective scheme, and atmospheric information from the surface layer scheme. Noah LSM predicts root zone, evapotranspiration, soil drainage, runoff, soil ice and fractional snow cover effects. It considers differences between vegetation categories, monthly vegetation fraction, soil texture and surface emissivity properties. The scheme provides sensible and latent heat fluxes for the PBL scheme (Skamarock et al., 2008).

Cumulus convection scheme

Convective schemes are necessary for the representation of convective precipitation and shallow clouds on a sub grid scale. It represents the unresolved updrafts by vertical fluxes and operates coloumnwise in grid cells when triggered. It is not recommended for grid sizes lower than 5 km when the model is expected to resolve the convective eddies explicitly (Skamarock et al., 2008). For this study the Kain-Fritsch convective scheme has been used. This scheme uses a trigger function to identify potential convective layers. The up- and downdrafts are represented by a entrainment-detrainment plume model, which is active until 90 % of the convective potential energy (CAPE) is removed(Kain, 2004).

4.1.8 Spectral nudging

Large scale features of the atmospheric conditions may drift during the model run. To avoid this, spectral nudging (SN) can be applied to constrain the model towards the driving external field. By choosing the minimum wavelengths to be nudged, only the large scale features are constrained, whereas the shorter wavelengths are allowed to develop freely. Mathematically this is performed by extending the governing equations with artificially nudging terms for zonal and meridional wind components, temperature and geopotential height. The current version of WRF does not allow for SN of humidity. Recent work by Spero et al. (2014) suggests that WRF could improve the representation of precipitation by incorporating SN on humidity. But this have yet to be done.

The benefit of SN has been examined in a number of studies. Miguez-Macho (2004, 2005) found that without nudging the precipitation was dependent on the domain size and location. This bias was removed when SN was applied to the model run. Glisan et al. (2013) investigated the influence of SN on several domains in WRF and found reduced biases on nearly all examined variables. Another study (e.g. Alexandru et al. (2009)) has shown a negative tendency in the ability to represent extreme precipitating events when the model is nudged to strong towards the large scale dataset. However, for small scale features and precipitation Liu et al. (2012) concludes that SN performs better than grid nudging by only affecting the large scales and is therefore the preferred nudging strategy. Omrani et al. (2015) confirms this model improvement by using nudging. According to Omrani et al. the key variable to nudge is the tropospheric horizontal wind.

It has been argued that too strong nudging may filter out extreme events since nudging pushes the model towards a smoothed large scale (Alexandru et al., 2009). However, the study of Colin et al. (2010) suggests that SN generally does not degrade the model with respect to heavy precipitation and thereby should be able to represent the extreme events. It is, however, desirable to find an optimal nudging regarding cut-off wavelengths and relaxation time[1], which forces adequate towards the large scale, but still allows the model to develop freely. The optimal relaxation time has been studied with results indicating that the default values in WRF may be too high. This is due to the disharmony of the relaxation time of 1 hour and the higher temporal resolution of the external dataset (Omrani et al., 2012a,b). A relaxation time of 6 hours correlates best with observed values for their selected studies. Coefficients lowered by an order of magnitude show improved correlations with precipitation

---

[1]Relaxation time is the inversed nudging coefficient

observations (Glisan et al., 2013). Further studies in WRF nudging settings and the influence on model output are needed to find optimal settings, but so far studies confirm the improvement of model representation by the use of SN, and it is therefore a preferred strategy in recent work.

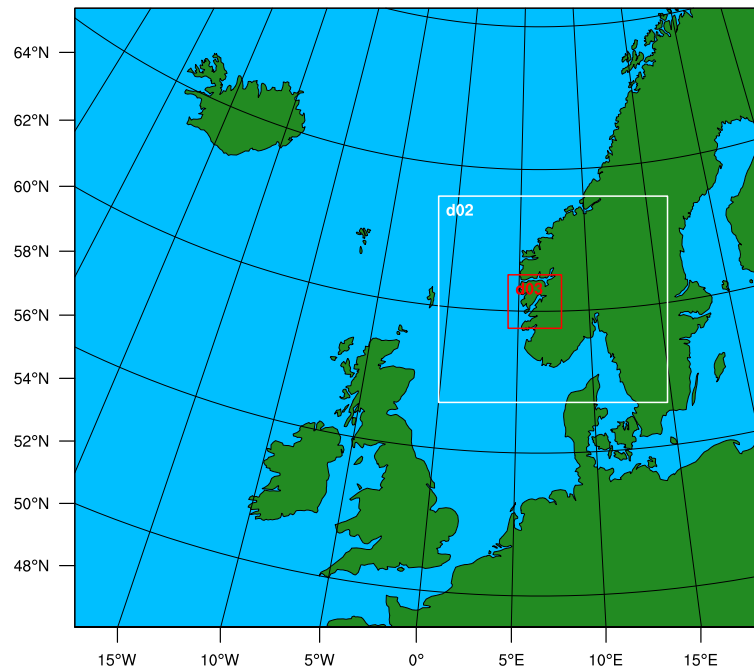## 4.2 Experimental set up

Figure 4.6: Model domain set up. Domains 1, 2, 3 have 9, 3, 1 km grid resolution.

The WRF model version 3.5.1 has been used for a case study of the flooding event (Chapter 6). The type of map projection used is the Lambert projection with true latitude on N60°. The outer domain has 301×271 grids, with a grid resolution of 9 km resulting in a domain of 2709 km in the east west direction, and 2439 km in the north south direction, the temporal resolution was set to 45 seconds. The nested domains 2 and 3 have a grid resolution of 3 km and 1 km and were run with time steps of respectively 15 and 3 seconds. The 301×271 grid points of domain 2 result in a domain size of 903×813 km, while domain 3 has an extension of 211×211 km. Grid resolution as low as 1 km have been chosen since earlier studies indicate that 3 km grid resolution is insufficient in complex terrain as Western Norway (e.g. Mesquita and Barstad (2006); Barstad and Caroletti (2013)). Two way nesting has been used, where boundary conditions are interpolated from their respective parent domains. All domains have 70 vertical levels with a top of 50 hPa. Figure 4.6 shows the location of domain 2 and 3 with respect to domain 1.

The terrain has been smoothed in the simulation (See section 6.3.1). Ideally the WRF topography should not be smoothed. However, the steep topography in model domain 3 caused stability errors. With time steps as low as 2 seconds the model was unable to run without smoothing the topography. The minimum smoothing, which allowed the model to avoid stability errors, was found to be the special smoothing desmoothing option with 2 smoothing passes over the terrain. The smoothed terrain compared to ASTER Global Digital Elevation Model (GDEM) Version 1 (Tachikawa et al., 2011), for part of the innermost domain, is shown in Figure 4.7.
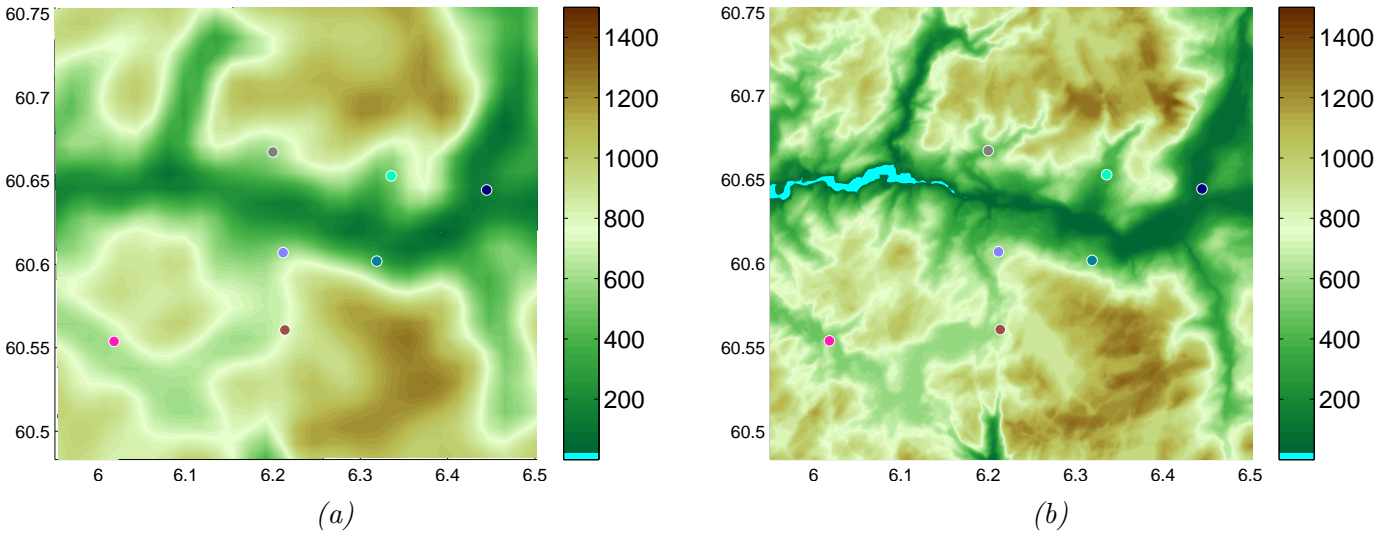

Figure 4.7: Comparison of WRF terrain, (a) smoothed by the smooth-desmooth special option and (b) ASTER GDEM v1 satellite measured terrain.

The parameterizations selected for the simulations in this work are listed in Table 4.1 and have been described previously in Section 4.1.7. These have been used throughout the three domains with the exception of the convective cumulus scheme. Barstad and Caroletti (2013) studies the effect on a 3 km grid resolution and find better correlation with the observed values during the run without the convective scheme active. For this reason the cumulus parameterization was limited to the outer domain.

Table 4.1: Parametrization schemes.

Category of physics	Parametrization schemes used
Microphysics	Thompson (Thompson, 2004; Thompson et al., 2008)
Short wave radiation	Dudhia shortwave (Dudhia, 1989)
Long wave radiation	RRTM longwave (Mlawer et al., 1997)
Planetary boundary layer	MYJ (Janjić, 2000)
Land surface model	Noah LSM
Cumulus	Kain Fritsch (Kain, 2004)

Initial and boundary conditions for the outer domain have been interpolated from the ERA-Interim dataset provided by ECMWF (Dee et al., 2011). ERA-Interim is a global reanalysis dataset with a horizontal grid resolution of 0.75°×0.75°, interpolated to 0.25°×0.25°. Vertically WRF was initialized with 60 model levels from the ERA-Interim. The outer boundary conditions and the sea surface temperature are updated in WRF every 6 hours during the simulation period. Spectral nudging was applied to the horizontal wind components, the temperature and the geopotential height. It was applied in the outer domain only, and trough the full simulation length. One simulation without nudging was conducted for comparison (Section 6.3.3). An overview of the different spectral nudging settings are listed in Table 4.2.

Table 4.2: Overview of the different model runs and their spectral nudging settings.

Nudging	Relaxation time [h]	Nudging coefficients [s^{-1}]	Wavelengths nudged [km] Zonally (Z), Meridionally (M)
No	N/A	N/A	N/A
Yes	1	3.0×10^{-4}	338 Z, 304 M
Yes	1	3.0×10^{-4}	677 Z, 609 M
Yes	1	3.0×10^{-4}	903 Z, 812 M
Yes	6	4.62×10^{-5}	677 Z, 609 M
Yes	24	1.16×10^{-5}	677 Z, 609 M

4.2.1   WRF data analysis

After removal of 24 hours of spin up time, the data from WRF were analyzed with the use of the NCAR Command Language (NCL). An exception was the ts list, containing the position of the 11 operational stations, which was compared to observational data utilizing Matlab. When analyzing the point precipitation in a model, representativeness error could have an influence on the output. To minimize these errors four points in addition to the actual grid point were averaged to represent the position of each observational station. These points were chosen as the ones one km to the N, S, E and W of the selected station grid point. Figure 4.8 shows the original grid point precipitation along with the mean calculated. The gray band shows the model spread within the five points. Large variations are seen at stations in steep and sloping terrain, (e.g. P3, P4, P10 and P11) where the grid altitude varies considerably between the adjacent grid points. However, all stations have a mean precipitation rather close to the center point precipitation. Therefore the mean precipitation has been chosen to represent the point precipitation at the individual stations. For the 3 km and 9 km domain a mean of the nearest grid points are assumed to contaminate the fine scale signals, and therefore only the grid points are used when analyzing these domains.

To analyze the performance of the WRF simulations with a statistical approach, the root mean square error (RMSE), the mean absolute error (MAE) and the mean error (ME) are calculated. Values for
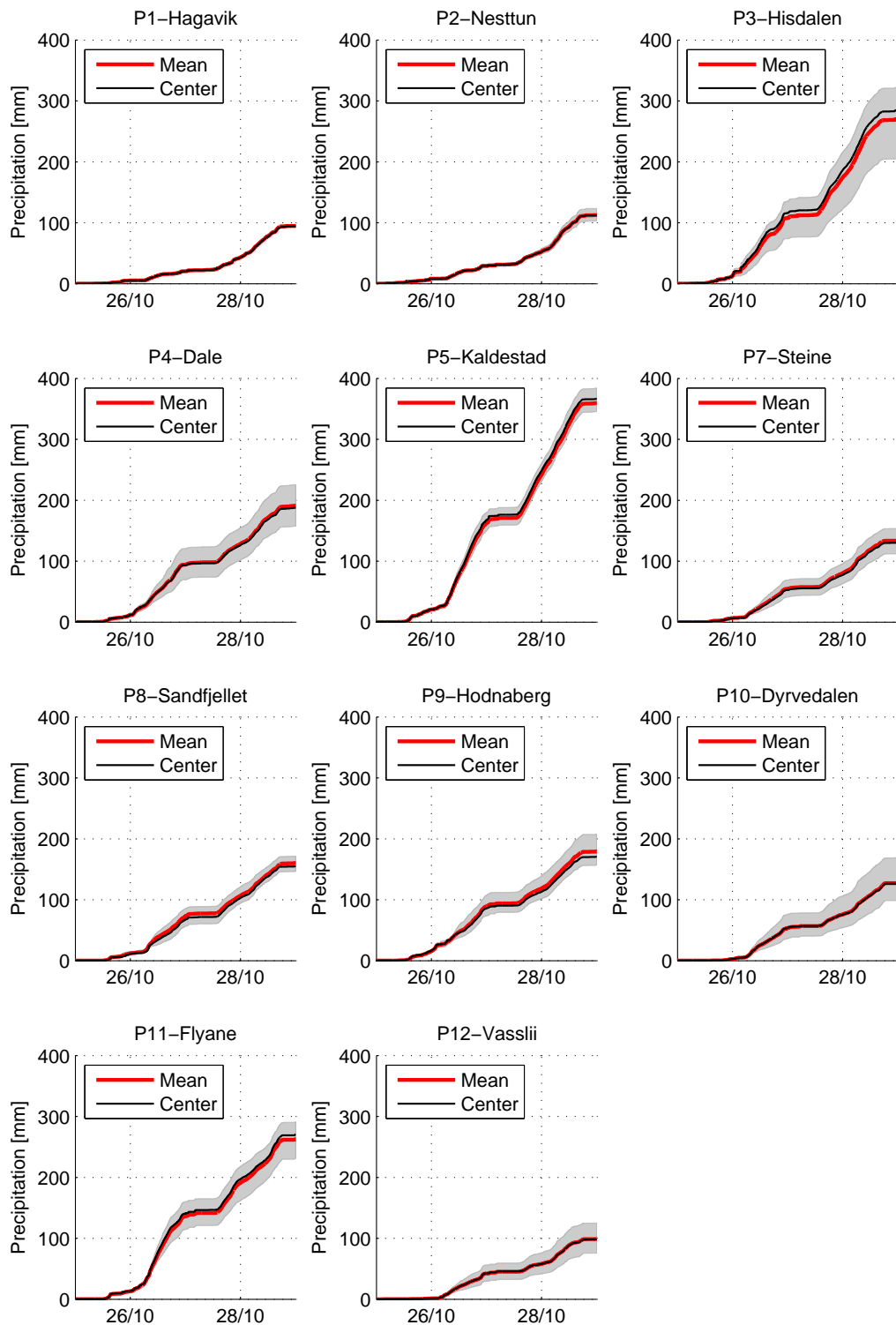
Figure 4.8: A comparison of the mean and center point precipitation on each station. The gray shading indicates the range of precipitation from the five points 1 km N, E, S and W of the center point.

each model run has been calculated using the following formulas

$$RMSE = \sqrt{\frac{1}{n}\sum_{i=1}^{n}(f_i - o_i)^2} \tag{4.2}$$

$$MAE = \frac{1}{n}\sum_{i=1}^{n}|(f_i - o_i)| \tag{4.3}$$

$$ME = \frac{1}{n}\sum_{i=1}^{n}(f_i - o_i) \tag{4.4}$$

where f are the forecasted values, o are the observations and n is the number of equal timestamps. Positive values of ME indicates the model is overestimating, negative values indicates underestimation.

Chapter 5

Measurement results

In the following chapter the precipitation observations will be presented and analyzed. The investigation is based on 6 hourly integrated precipitation amounts, for a direct comparison with reanalysis data of the same time resolution. In a first section the time series and the accumulated precipitation for the different station will be presented and discussed individually for the pre- and main campaign. After that, the observed precipitation data set will be statistically analyzed with respect to a wind speed and wind direction dependency in the complex topography of the area.

5.1 Pre campaign

An overview of the pre campaign is presented as time series in Figure 5.1. It shows the precipitation amount based on 6 hour accumulation intervals in the lower panel, together with the wind conditions at 850 hPa, taken from the ERA Interim reanalysis in the upper panel. Several separated precipitation events can be detected. The signal shape of the events is similar for all stations, indicating that the precipitation mainly origins from synoptic scale frontal systems rather than from mesoscale showers. The strongest precipitation events are primarily associated with higher wind speeds from S-SW.

The largest amount of precipitation during a 6 hour period was observed at Steine on the 7th of October with 22.5 mm measured from 6 to 12 UTC. The period was part of a precipitating event (6th-9th of October), which was strongly influenced by orographic effects. The station at Steine collected 95 mm during this event, whereas the other stations measured 53-64 mm of precipitation. The largest differences arose on the 6th and 7th. The prevailing wind direction in the 850 hPa level was SW during the majority of the event, veering slightly towards west at the end. The wind speed was 10-15 ms^{-1} on the 6th and 7th, reducing to below 10 ms^{-1} on the 8th. The stronger winds were associated with the largest differences in precipitation amounts between the stations. On the 8th the wind speed decreased and the station measurements became more homogeneous. Other examples of high wind situations are the 16th of September, 23th of October and 28th of October, all resulting in considerable precipitation variability between the stations.

One precipitation event with low wind speed shows small variability in the measurements between different stations. The 7th of September has SE wind of around 6 ms^{-1} and indicates very similar precipitation amounts at all stations. The 22nd of September also has homogeneous measurements between stations, but at a higher wind speed of approximately 10 ms^{-1}. One would have expected larger variability due to the relative high wind speed.
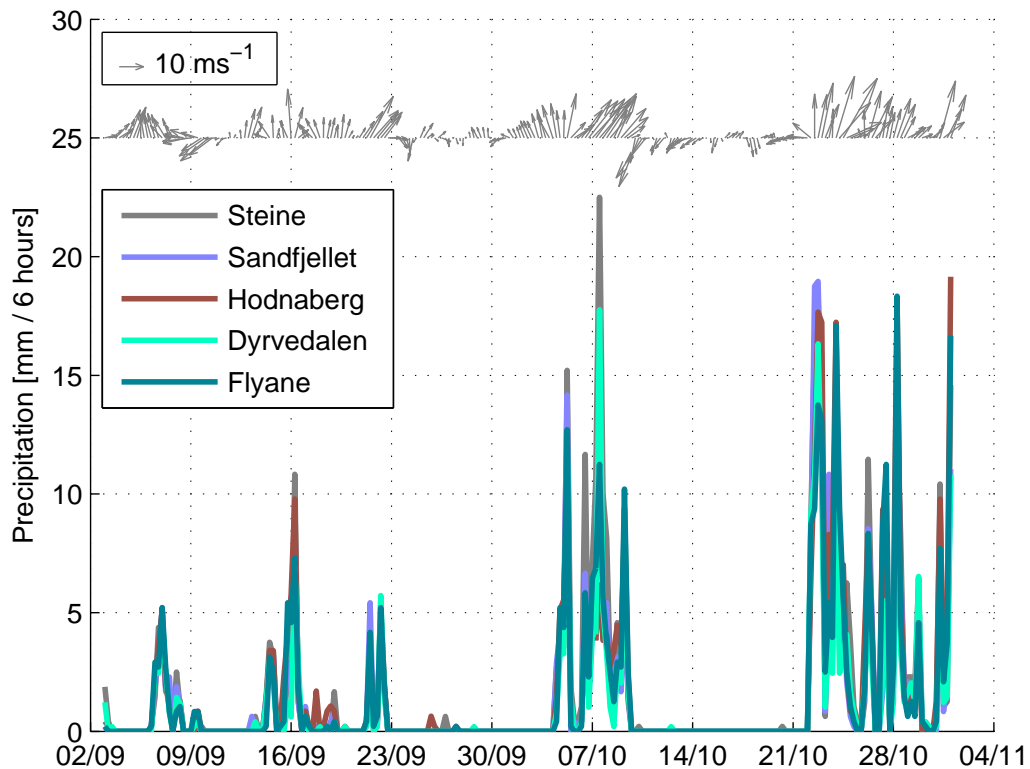

Figure 5.1: Time series of precipitation accumulated over 6 hours (lower panel), and corresponding wind conditions at 850 hPa from ERA-Interim (upper panel).

Figure 5.2 presents the accumulated precipitation, both in absolute values (left) and normalized by the total precipitation amounts for each station (right), during the pre campaign period. The absolute values show a considerable variability of around 40 % between Dyrvedalen (267.3 mm) and Steine (375.2 mm). The normalized figure indicates that the majority of the difference arose during the event 6th-9th of October.
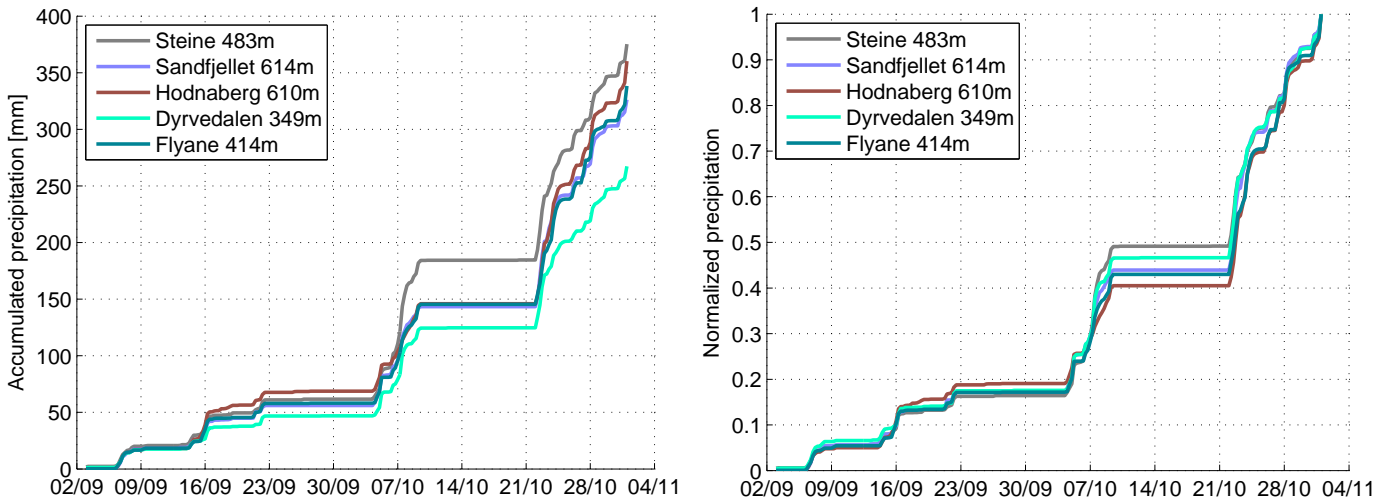
Figure 5.2: Accumulated precipitation amount during the pre campaign 2013. Total sums are given in the left panel, the normalized values in the right panel.

5.2 Main campaign

The corresponding time series of the main campaign are presented in Figure 5.3. As in the pre campaign the overall shape of the individual station signals are similar and the major precipitation events are associated with a flow from S-W. The summer months have some higher variability among the stations, probably caused by local convective precipitation events, while the autumn months again have a more homogeneous precipitation signal, indicating mainly synoptic scale originated precipitation. In the period 27-29th of October a major flooding event took place in Western Norway. This event is characterized by large local differences and is analyzed in detail in Chapter 6.

Figure 5.4 shows the accumulated precipitation in the campaign period. It varies from Vasslii (P12) with only 674 mm to Hisdalen (P3) with 1443 mm, an increase of 114 %. From the stations located at the plateau, the highest collecting rain gauge was Kaldestad (P5) with 1326 mm. The stations Hisdalen (P3), Dale (P4) and Kaldestad (P5) all collected large amounts of precipitation, the stations are located partly in sloping terrain and are expected to have orographic enhanced precipitation. Dyrvedalen (P10) and Vasslii (P12) are on the downwind side of the Hamlagrø plateau and show reduced precipitation in comparison to the upwind stations.

The autumn values have been examined separately to include Steine in the evaluation. The data acquisition here started on the 30st of July because of a rain gauge failure earlier in the campaign period. This also has the advantage of minimizing the influence of diurnal convective situations, and therefore focusing on the forced ascent aspect of orographic precipitation. The left panel of Figure 5.5 shows the accumulated values from August to November 2014. The stations Hisdalen (P3), Dale (P4) and Kaldestad (P5) have the largest amounts of precipitation during the autumn. Dyrvedalen (P10) and Vasslii (P12) have the lowest amounts. The precipitation amount at Hisdalen is more than
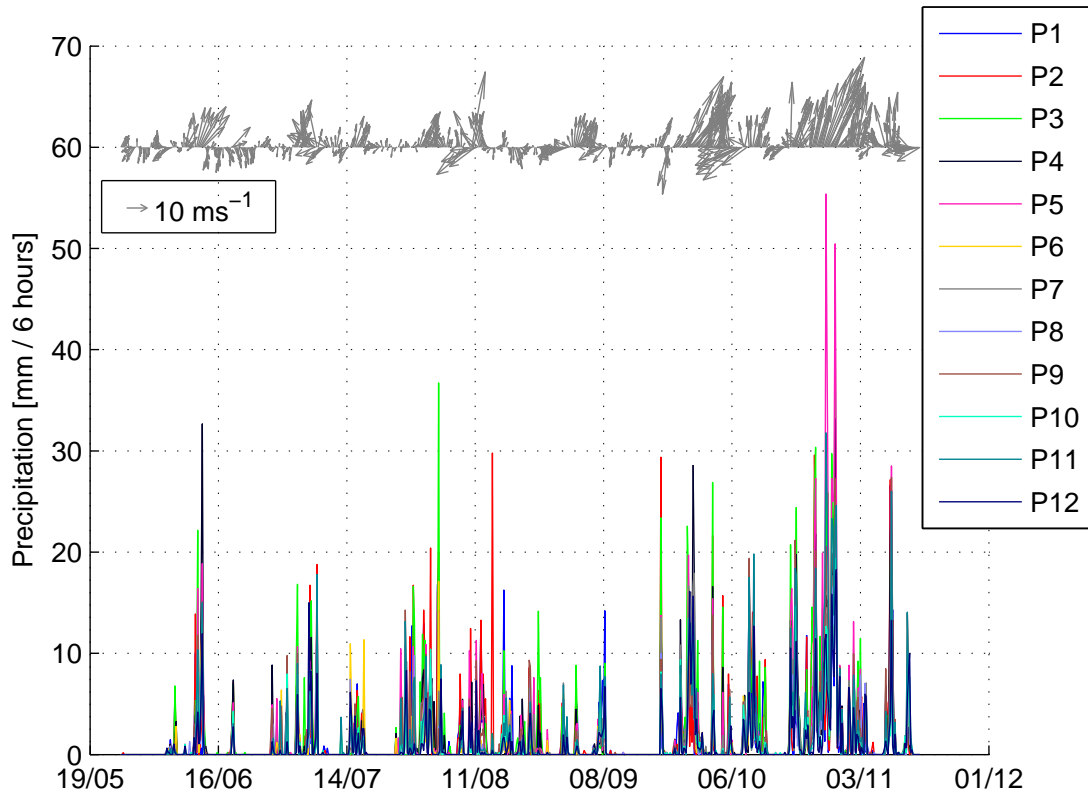
Figure 5.3: Time series of the 6 hour accumulated precipitation values (lower panel) and the ERA-Interim wind conditions from the 850 hPa level (upper panel).

a factor of 2 larger than at Vasslii. The accumulated autumn signals are similar to the signals for the complete period, indicating that the synoptic orographic effect is dominating both during the summer and autumn seasons.

In the right panel of Figure 5.5, the normalized accumulated precipitation for August to November is presented. The stations Hagavik (P1) and Nesttun (P2) have similar profiles with a larger amount of the precipitation during the first half of the period, differing from the remaining which catch up in particular during the late stage of the period. The two stations are located near the coast, and the first part of the period was affected by strong convective situations, mainly at the coast. Additionally the synoptic scale precipitation reaching the stations are similarly affected because of their upwind position of the mountainous terrain. The remaining stations are further inland and each are prone to different orographic effects. In particular the month of October, including major rain events, shows a considerable variability among the remaining stations.
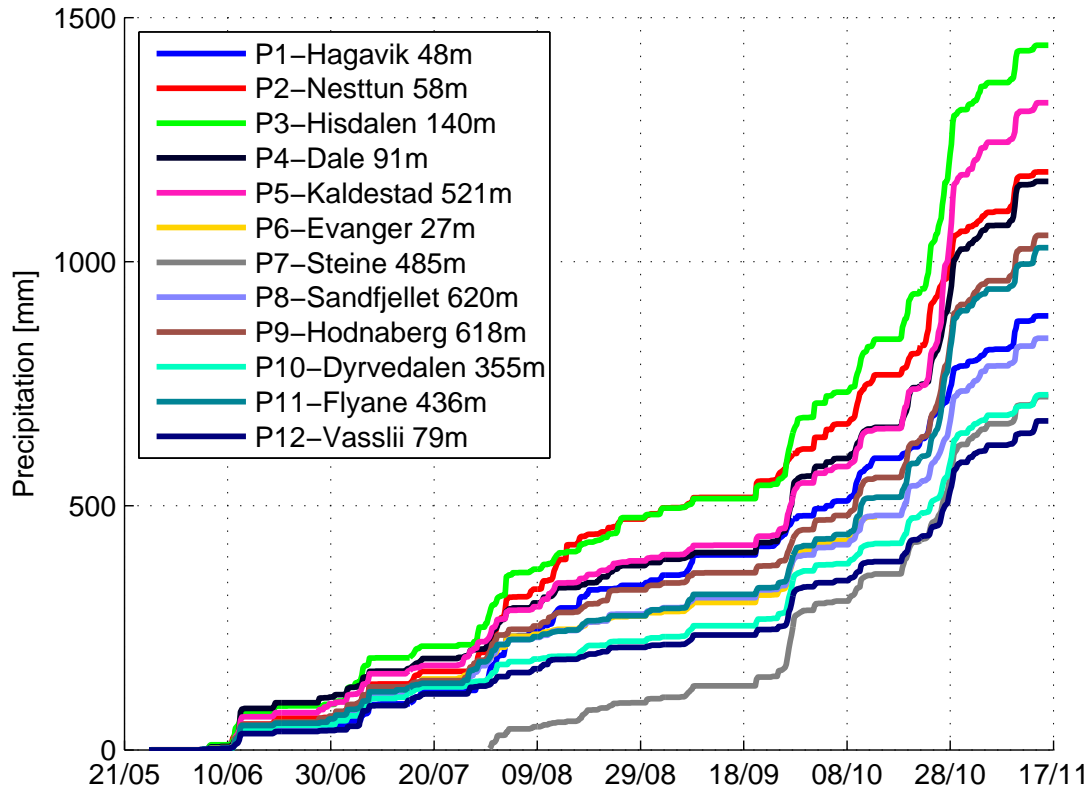
Figure 5.4: Accumulated precipitation for the stations in the main campaign 2014.

5.3 Wind analysis

The critical mountain height M in equation 2.5 indicates that the wind speed is an important factor for orographic modification of precipitation. Likewise influences the topography in the wind direction the flow field and thereby the distribution of precipitation. Thus wind and topography will be used in the following to separate the precipitation events into different regimes. As the dataset collected during the campaigns does not include own wind measurements, several available data sets[1] have been considered to find a representative wind proxy for the campaign area. Finally the ERA-Interim reanalysis from the European Centre for Medium-Range Weather Forecasts (ECMWF) was chosen. It provides meteorological parameters every 6 hours on a horizontal resolution of 0.75° (Dee et al., 2011). It was selected as the best compromise between horizontal and temporal resolution. The grid point chosen to represent the area is N 60.5° and E 006°, positioned in the western part of the Hamlagrø plateau. The wind data is taken from the 850 hPa level to minimize a local topographic disturbance of the wind field, and is used as a proxy for the synoptic scale flow in the area. Precipitation amounts are integrated over 6 hours from 0-6, 6-12, 12-18 and 18-24 UTC. The 6 hourly wind data from

---

[1]NCEP reanalysis, ECMWF forecast, Sola radiosonde and ERA-Interim reanalysis
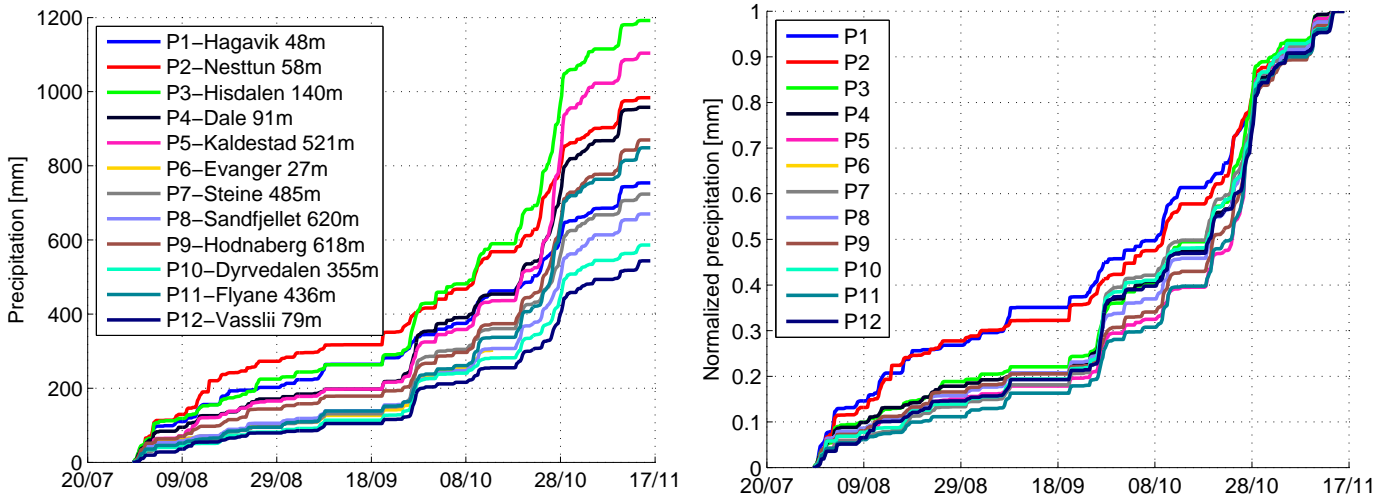
Figure 5.5: Accumulated precipitation amount during the autumn of the main campaign. Total sums are given in the left panel, the normalized values in the right panel.

ERA-Interim, available at 0, 6, 12 and 18 UTC, have been interpolated to the center times of the precipitation periods, i.e. 3, 9, 15 and 21 UTC.

The prevailing wind direction on the Norwegian west coast is from SW, the campaign periods are no exception. Figure 5.6a gives an overview of the wind conditions in the campaign periods. The figure shows prevailing wind directions from SW, with a secondary maximum at ENE. Nearly 75 % of the periods have wind speeds below 7 ms^{-1}, and only less than 4 % have higher wind speeds than 15 ms^{-1}. Wind directions and speed for periods with precipitation on any of the stations are shown in Figure 5.6b. The prevailing precipitating wind direction is also SW, whereas the secondary maximum at ENE reveals to be mainly non precipitating. The majority of the precipitating periods are still associated with low wind speeds, 62 % is at or below 7 ms^{-1}. The corresponding results for strong precipitating periods, defined as a station mean of more than 5 mm per 6 hours, are shown in Figure 5.6c. The prevailing wind direction from SW is now nearly the only direction producing those high precipitation events. The corresponding wind speed histogram now peaks in the region of 10-15 ms^{-1}, in which 49 % of the high precipitation events are found.

## 5.3.1 Influence of wind speed and direction

While Figure 5.6 focused on the general features of precipitation in the area in dependency of wind speed and direction, this section is now focusing on the corresponding results on the individual station level. The precipitation amounts presented are normalized to enable comparability between stations, unaffected by whether they were included in the pre campaign or not. The evaluation of the individual stations is presented by separating into different wind speed regimes. With an critical mountain height of approximately 1200 m, the corresponding low wind situations, expected to represent blocked
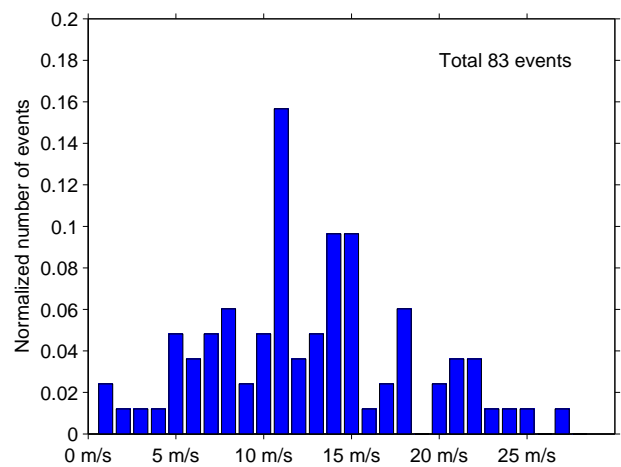
(a)

(b)

(c)

35
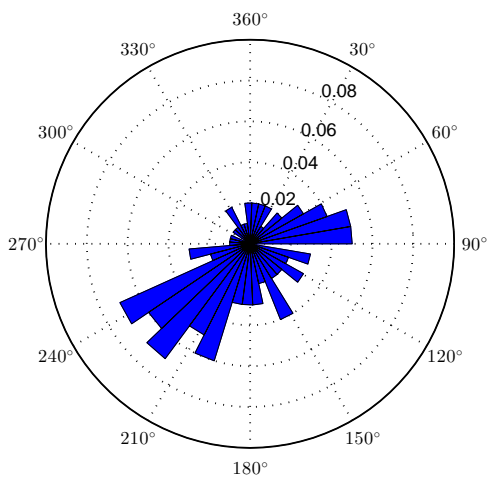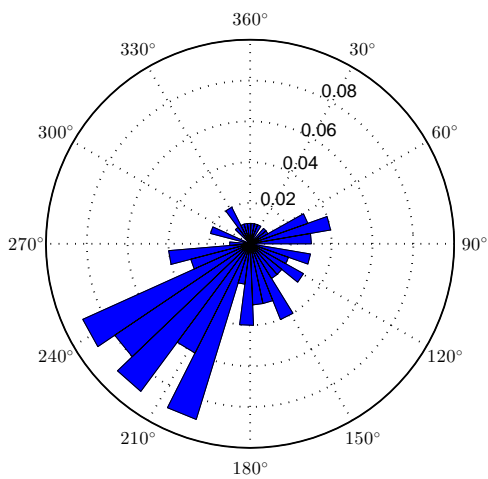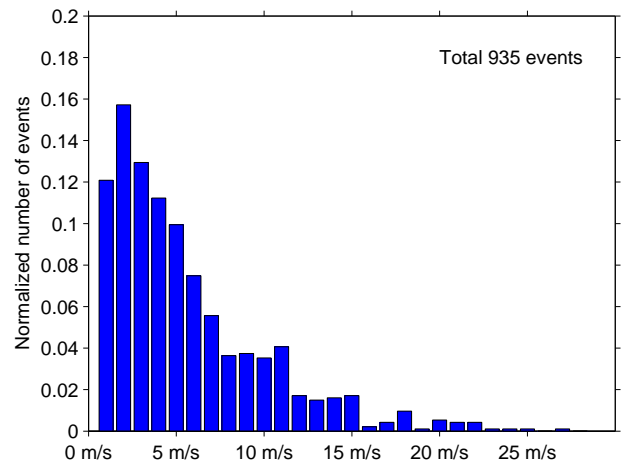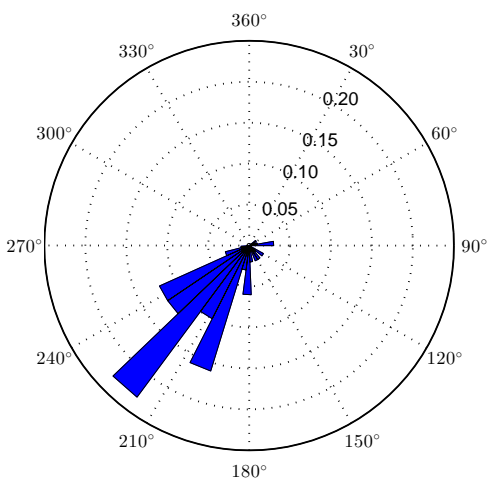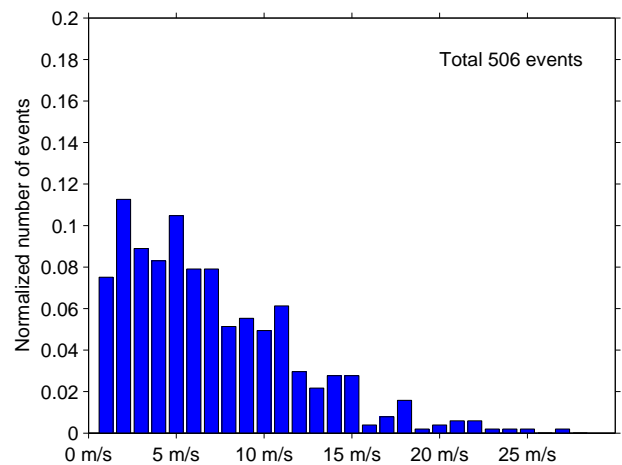
Figure 5.6: Wind rose and wind speed histograms for (a) the whole pre- and main campaign period, (b) for precipitating events only, and (c) for heavy precipitation events.

situations, are defined as 0-6 ms^{-1} (see Section 2.2). The higher wind situations, corresponding to unblocked flow conditions, have been categorized by a wind velocity of 10 ms^{-1} or above. This is a slightly higher wind speed threshold than directly resulting from the calculation, but has been chosen to ensure a clear separation between the regimes. The low wind cases are colored blue, the high wind cases red, and the intermediate cases green.

Figure 5.7 presents the normalized precipitation amounts on each station, dependent on wind directions. The percentage of precipitation for the high and low wind cases are indicated in the figure. Each panel also shows the total amounts of precipitation collected during the pre campaign, indicated by P, and the main campaign, indicated by M.

The station signals are similar, all with the majority of the precipitation collected for wind directions between 180° and 250°. All stations have a clear maximum at 220°. This correspond to the highest number of events (see Figure 5.6b), but also includes 40-70 % of the precipitation from the major flooding event, described in detail in Chapter 6. The exception is Evanger (P6), whose rain gauge was inoperative during the flooding event. Of the remaining 11 stations, Hagavik (P1) and Nesttun (P2) show a different behavior with respect to the precipitation distribution between high and low wind speed situations. More than 30 % of the precipitation is related to low wind situations whereas the remaining stations have around 20 % of their observed precipitation during these events. The stations are located at low elevation near the coast. The larger portion of low wind speed related precipitation is potentially caused by the higher amount of coastal convective precipitation that is usually associated with low wind speeds. In addition it may be caused by a pile up of air upstream of the mountainous terrain during blocked situations, forcing the positive vertical velocity perturbations and therefore also the precipitation patterns to move further upstream.

Figure 5.8 presents the total amount of precipitation for each wind speed interval during the campaign periods. As previously the percentage of total precipitation for wind speeds at or below 6 ms^{-1} is presented in the left hand corner of the figures, likewise for the events with wind speeds at or above 10 ms^{-1} in the right hand corner.

All stations have precipitation distributed over a wide range of wind speeds, and the histograms look rather spiky. This is assumed to be caused by the relatively short sampling period, where single events can have large effects on individual wind speed bins. A weak indication of a bi-modal distribution can be seen, with a second maximum around 20 ms^{-1}, mainly related to the flooding event, where 60-85 % of this precipitation was collected. Apart from Evanger (P6) with less data, all stations have a distinct peak at 11 ms^{-1}. This peak is not related to a single precipitation event, but rather a collection of several precipitating periods. 7 periods with an station mean of more than 10 mm per 6 hour are included in this bin. The increased low wind related precipitation at the near coast stations Hagavik (P1), Nesttun (P2) and partly Hisdalen (P3) are again detectable. Stations further inland have a larger portion of precipitation related to situations with wind speeds at or above 10 ms^{-1}. Station P5 has the highest high wind percentage of 68 %, and is mainly related to the large precipitation amounts during the flooding event on this particular station.

To investigate the effect of topography on the precipitation distribution further, a terrain categorization has been performed for each station. For that purpose topography cross sections from the
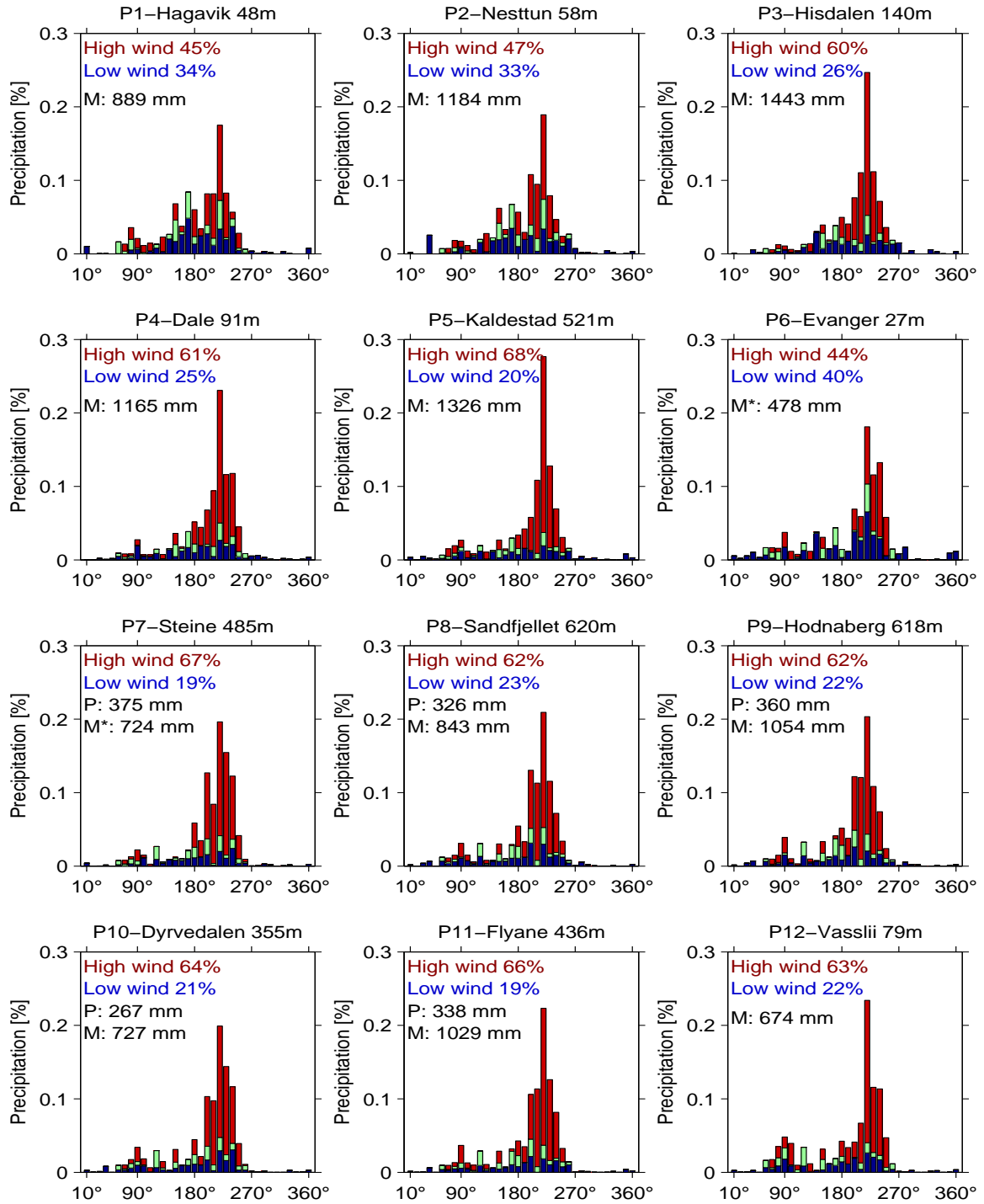
Figure 5.7: Normalized precipitation amounts as function of wind direction. Low wind cases ($V \leq 6$ ms^{-1}) in blue, high wind cases ($V \geq 10$ ms^{-1}) in red. The green cases (6 $ms^{-1} < V < 10$ ms^{-1}) indicate intermediate winds. The total collected precipitation amounts at each station for the pre campaign (P) and the main campaign (M) are shown in each window. Only stations P7-P11 were also operative during the pre campaign. P6 and P7 were inoperative during parts of the main campaign (∗), and have therefore a reduced data base.
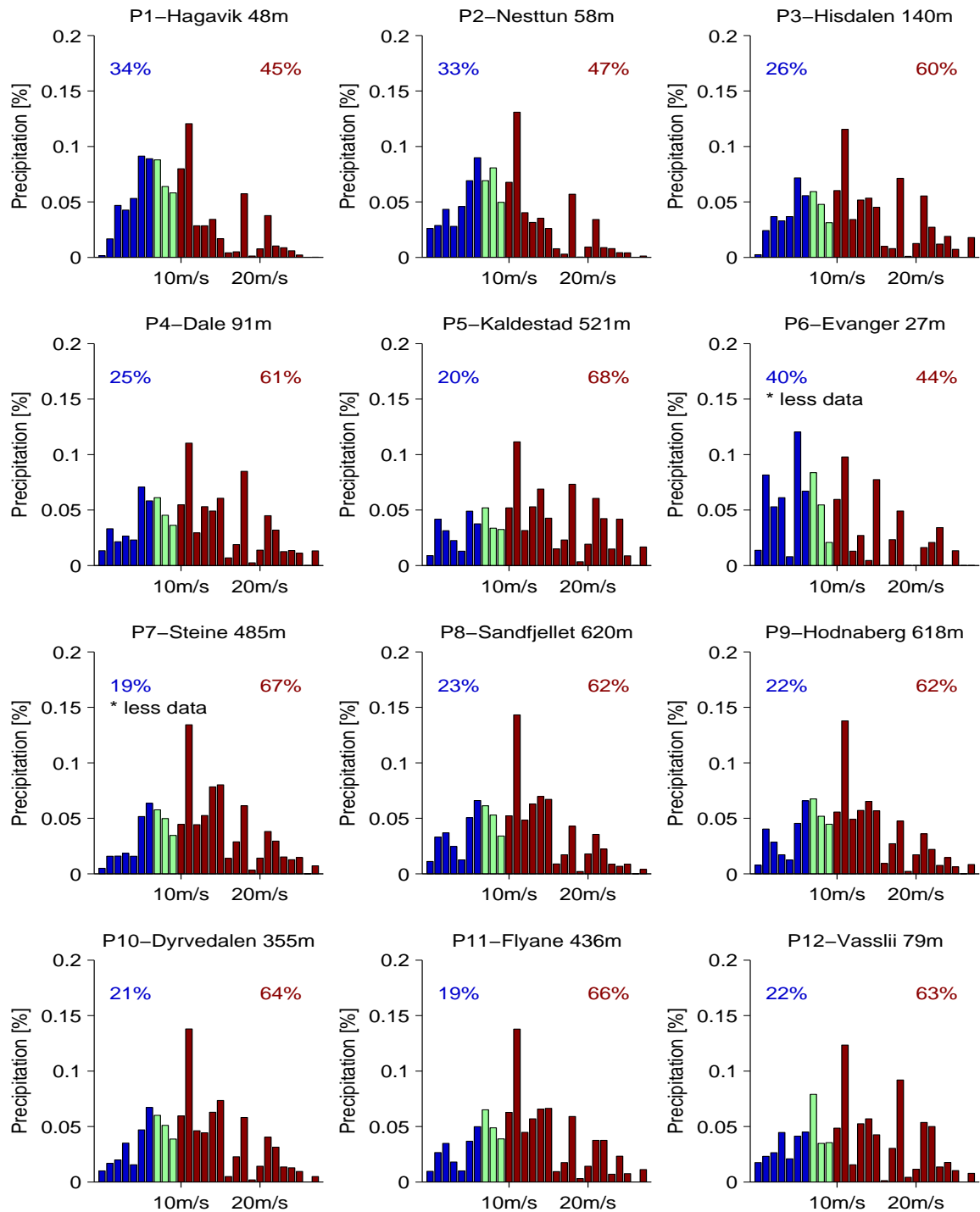
Figure 5.8: Normalized amount of precipitation depending on the wind speed for each of the 12 stations.

ASTER GDEM v1 dataset have been derived. The time scale factors for cloud formation and fall out time, incorporated by Smith (2003), indicates a possible spill over effect up to 20 km behind a terrain feature[2]. The cross sections have therefore been selected to include a distance of 20 km upstream and downstream of each station. Cross sections of selected stations, discussed in more detail, are shown in Figure 5.9. The remaining terrain profiles can be found in appendix A.

Hagavik (P1) and Nesttun (P2) are coastal stations at low elevation with flat terrain upstream and moderately high and steep terrain downstream. Hisdalen (P3), Dale (P4), Kaldestad (P5) and Evanger (P6) are also located at low elevation, but with steep terrain up- and downstream. Mountainous stations as Sandfjellet (P8), Hodnaberg (P9) and Flyane (P11) are situated at higher elevation and have high terrain up- and downstream. Kaldestad (P5) could be placed in both the steep terrain category and the mountainous category. Due to its measurements similarity with Hisdalen (P3) it is categorized in the upsloping terrain category. The remaining stations Steine (P7), Dyrvedalen (P10) and Vasslii (P12) are positioned on the north side of a valley, in upsloping terrain. They all have massive barriers upstream and high terrain downstream. Table 5.1 summarizes the features.

Table 5.1: Categorization of measurements stations.

Station	Elevation	Upstream	Downstream	Category
P1	Low	Flat	Moderately	Coast
P2	Low	Flat	Moderately	Coast
P3	Low	Moderately	High	Steep terrain
P4	Low	High	High	Steep terrain
P5	High	High	High	Steep terrain
P6	Low	High	High	Steep terrain
P7	Upsloping	High, valley	High	North valley
P8	High	High	High	Mountainous
P9	High	High	High	Mountainous
P10	Upsloping	High, valley	High	North valley
P11	High	High	High	Mountainous
P12	Upsloping	High, valley	High	North valley

For each summation period of 6 hours the area mean of all stations has been calculated. The wind analysis includes both the pre campaign and the main campaign values to increase the amount of data for statistics. Periods with no precipitation on all stations have been removed from the data set for this analysis. Wind directions have been separated into 36 directional bins, each sector includes the labeled wind direction $\pm 5°$.

The deviation of the individual stations from the area mean is presented in Figure 5.10 for low wind situations (V $\leq$ 6 ms^{-1}), and 5.11 for high wind situations (V $\geq$ 10 ms^{-1}). It shows the mean as a rectangular box and whiskers corresponding to a standard deviation of 1 σ. The number below the

---

[2]Combined time scale factor $\tau =$ 2000 s $* 10$ ms^{-1}
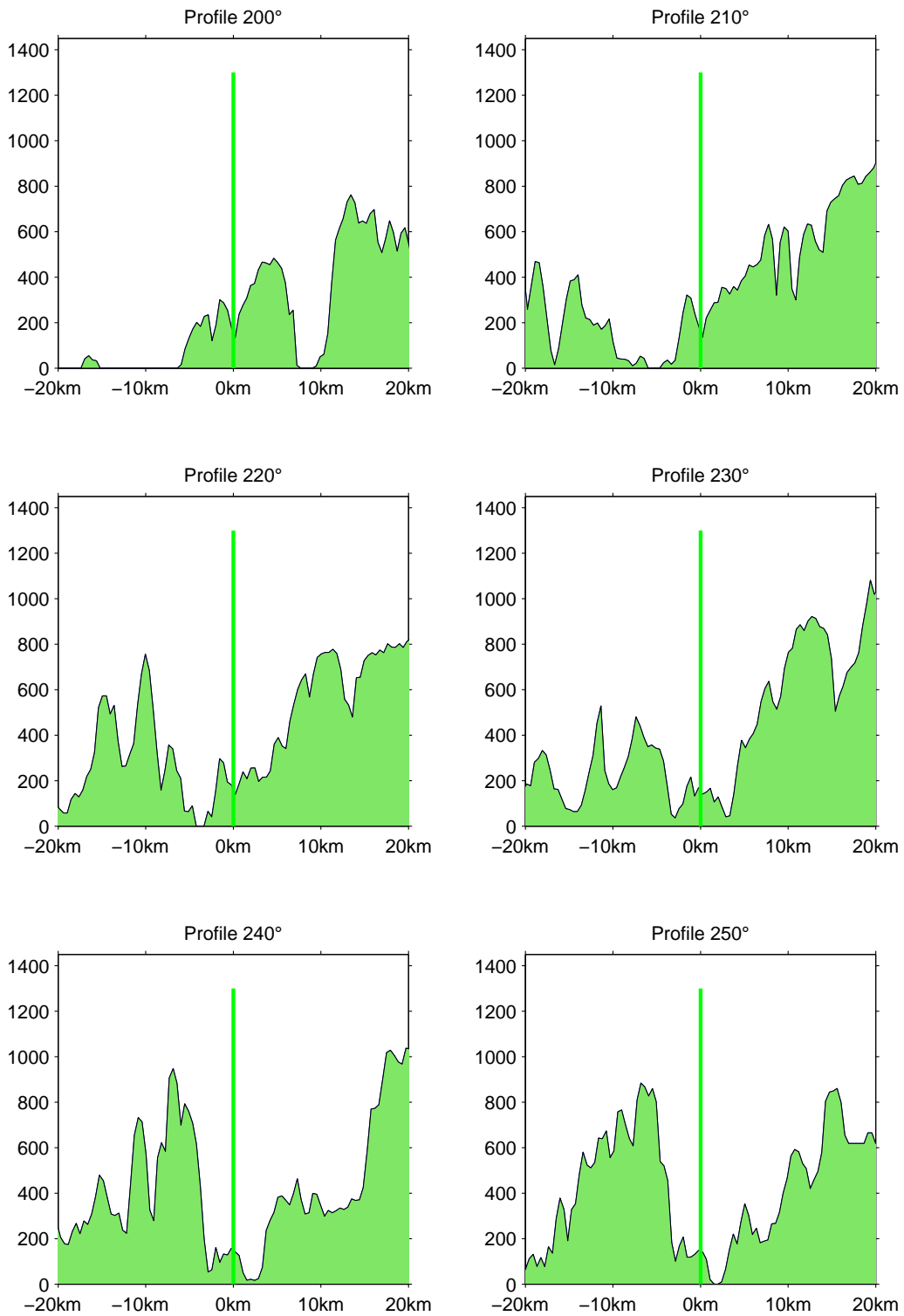
P3–Hisdalen 140m

Figure 5.9: Terrain profile from P3, Hisdalen. The panels corresponds to wind directions from 200°
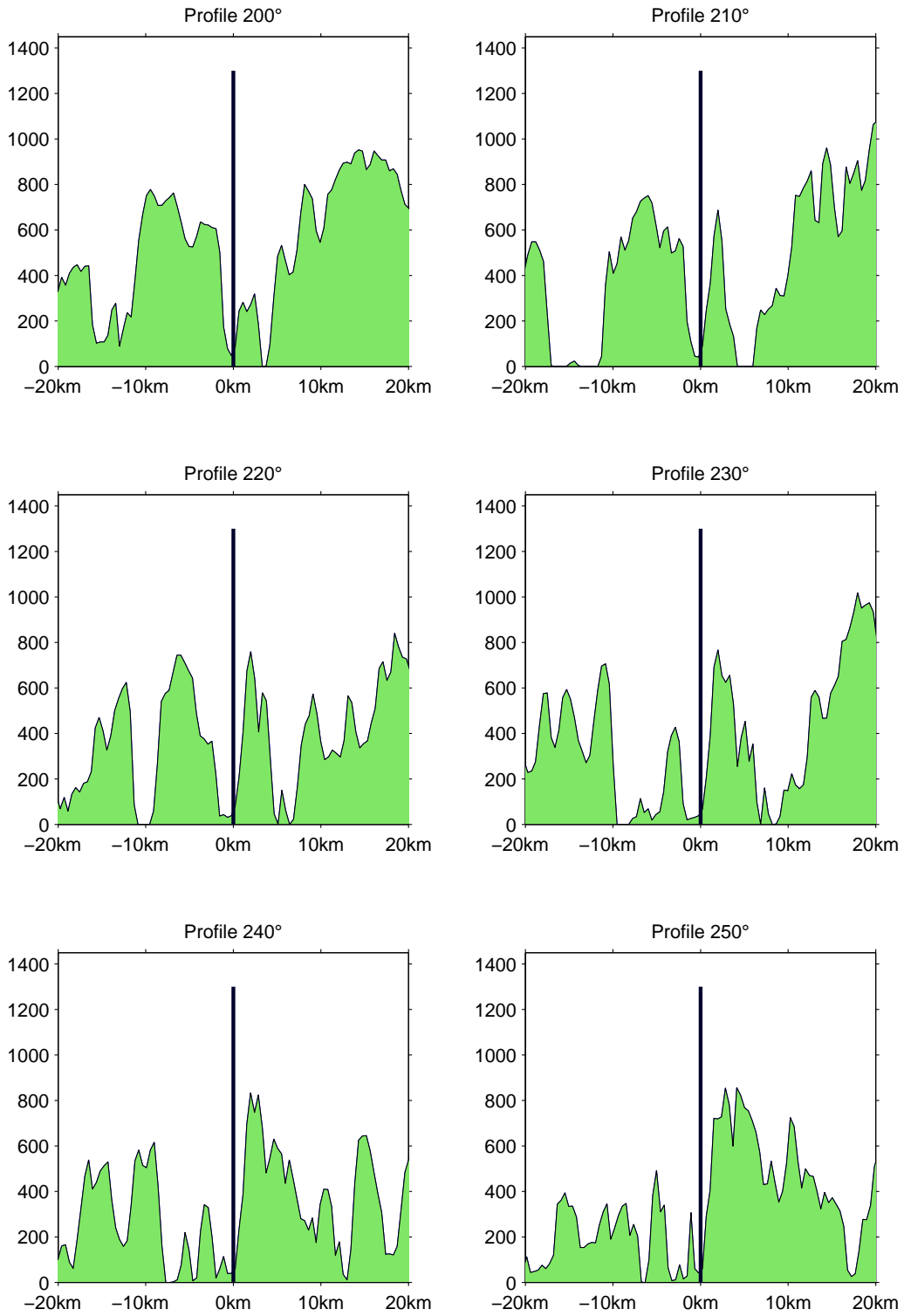to 250 °.

P4–Dale 91m

Figure 5.9: Terrain profile from P4, Dale. The panels corresponds to wind directions from 200° to 250°.
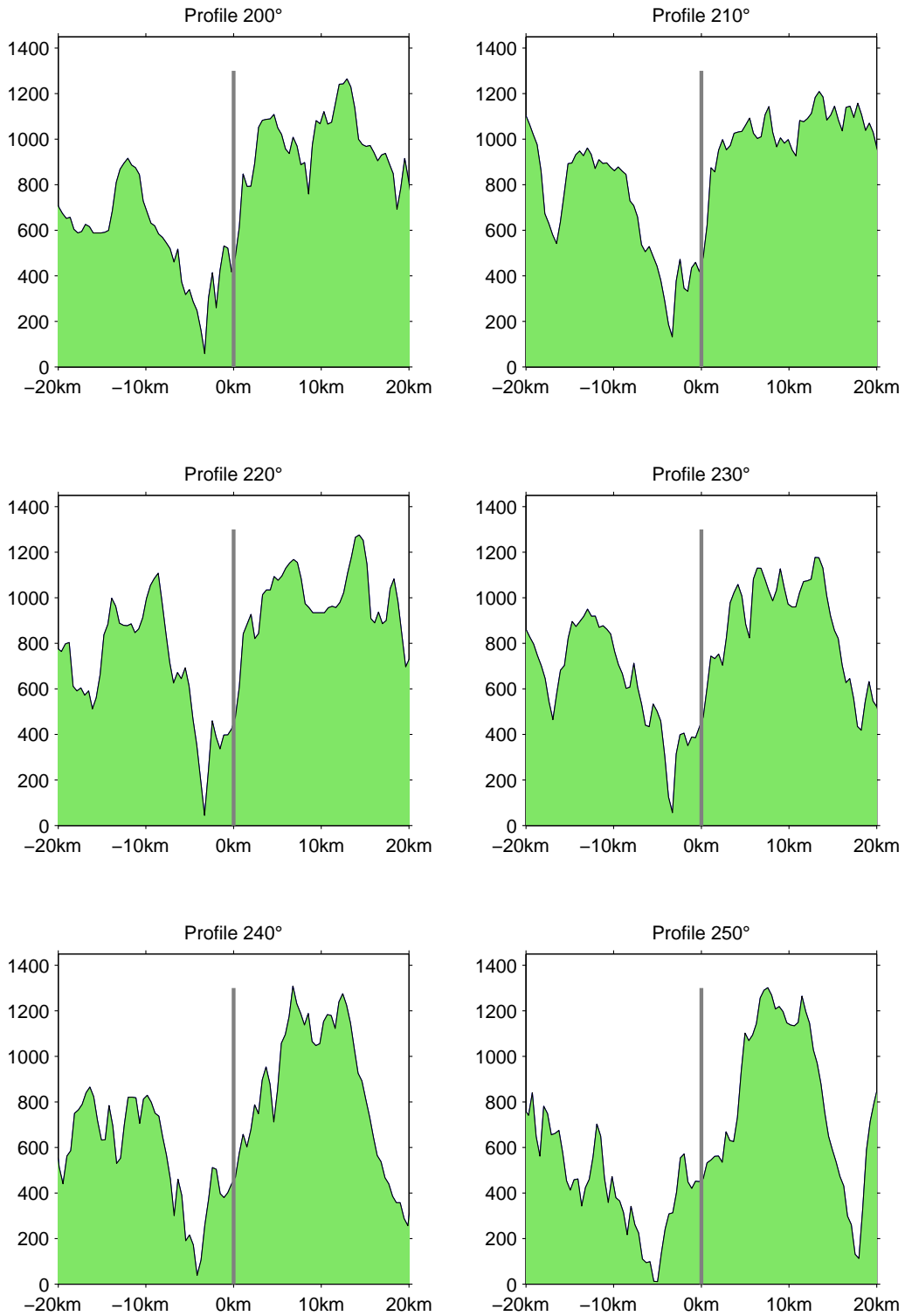
P7–Steine 485m

Figure 5.9: Terrain profile from P7, Steine. The panels corresponds to wind directions from 200° to 250°.

P8–Sandfjellet 620m

Figure 5.9: Terrain profile from P8, Sandfjellet. The panels corresponds to wind directions from 200°
to 250°.

bar represents the number of 6 hour periods with precipitation for the given wind direction. High wind situations with precipitation were not observed for wind directions more northerly than 260°.

The weak wind cases show an overall low standard deviation, and also none or only a weak wind direction dependency. The bin averaged data are in general close to the areal mean. The coastal stations Hagavik (P1), Nesttun (P2) and partly Hisdalen (P3) however have larger variability and a tendency of precipitation amounts above average. This could be related to the aforementioned convective situations for the SE wind directions and the pile up tendency, with more precipitation at the prevailing wind directions from S to W. The remaining stations have no clear wind direction dependency.

The higher wind cases mainly have data between 70° and 260° and show a tendency of two different precipitating regimes. One with wind directions from 70° to 170° with low variability, and the second regime, at 180° to 240°, with significantly higher standard deviations. The exception is Evanger (P6) which has less data assembled. The variability of wind directions from 70° to 200° could possibly be explained by the low number of cases and related higher uncertainty, whereas the range 210° to 240° is densely populated and therefore statistically more robust. The continued analysis will consequently mainly focus on the high variability area (210°-240°) with the dense data coverage. Sandfjellet, Hodnaberg, Flyane and Dyrvedalen (P8-P11) have a higher amount of precipitating periods than the remaining stations because they were operational in the pre campaign as well.

The closer investigation of Figures 5.9 and 5.11 together reveals the complexity of orographic precipitation. Of the basic processes described in Chapter 2, the synoptic scaled forced ascent is the clearest detectable. This orographic signal is visible as general increase in precipitation amounts from the coastal stations Hagavik (P1) and Nesttun (P2) to Hisdalen (P3).

Mesoscale features related to smaller barriers are responsible for the large variability with respect to wind directions for the stations situated further inland in the complex terrain. As described in Section 2.2.2 main mechanisms as forced upslope ascent and spill over effects increases precipitation whereas the enhanced evaporation on the lee side may create fohn gaps and decreases local precipitation. Some of these effects can be identified and explained by the available dataset. At Hisdalen (P3) for example, the large scale ascent is assumed to increase the overall precipitation. For wind directions up to 230° the deviations are approximately 4 mm per 6 hours above average, at 240° the precipitation deviation decreases significantly, now close to the areal mean. This coincides with a considerable altitude increase in the barrier upstream while the downstream orographic forcing remains rather constant or is even slightly decreasing. This behaviour indicates the presence of a lee side fohn effect for these specific wind directions.

Dale (P4) shows about average precipitation for 210° with a tendency of positive precipitation anomalies for wind directions towards W. In the 210° direction the valley is steepest and less than 4 km wide. One speculation is that the valley is too narrow and the flow over the barrier remains rather unaffected by its presence. When the valley widens out, the lee side descending air parcel is forced upward again when impinging the upsloping terrain directly downstream of the station. This could lead to the observed increase in precipitation when wind directions are veering towards W.

The northern valley stations Dyrvedalen (P10) and Vasslii (P12) have similar signals. The precipita-

tion deviation is approximately 3 mm per 6 hour below the areal average for wind directions from 210°
and increases towards the areal mean as the wind directions are veering towards W. The altitude of
the massive terrain barrier upstream (i.e. the Hamlagrø plateau) is decreasing, leading to less conden-
sation over the upstream barrier. Due to the reduced condensation ahead of the stations the humidity
concentration is assumed to be larger, which again increase precipitation amounts, when lifted at the
stations. The same tendency can be observed at Steine (P7), but its precipitation deviation at 210°
is only 2 mm per 6 hours, increasing to 2 mm per 6 hours above the areal mean. The difference
between Steine (P7) and Dyrvedalen (P10), Vasslii (P12) could arise because Steine (P7) is situated
closer to the coast whereas Dyrvedalen (P10) and Vasslii (P12) are further inland, resulting in less
precipitation than Steine (P7).

Sandfjellet (P8), Hodnaberg (P9) and Flyane (P11) are situated on the plateau with less precipitation
deviation observed. However a tendency of precipitation below average can be seen at P8 with wind
directions towards W. The station is located at a slightly downsloping terrain. At the prevailing wind
directions the downstream terrain is less massive, allowing for a lee side fohn effect without additional
lifting immediate downstream of the station.

The largest deviations in precipitation within the prevailing wind directions are at 220°. This direction
includes the majority of 6 hour periods during the flooding event, and has a large portion of high
wind periods as described earlier in this section. Figure 5.12 shows the same topography profiles as
previously, but to ease comparison for this single direction it is here displayed with stations P1 to P6
on one page and the remaining stations on the following page. The corresponding topography profiles
from 200° to 250° can be found in Appendix B.

The synoptic scale orographic modification is seen by a negative deviation in the flat coastal terrain
at Hagavik (P1) and Nesttun (P2). The large positive deviation at Hisdalen (P3) corresponds to the
upsloping terrain immediate downstream of the station, whereas the positive deviation at Kaldestad
(P5) could be related to either a spill over effect from the upsloping ahead, or a forced ascent from
the barrier downstream. Smaller deviations are found between the mountainous stations Sandfjellet
(P8) and Hodnaberg (P9). Sandfjellet (P8) is situated in downsloping terrain, possibly resulting in
precipitation reduction because of the fohn effect, whereas Hodnaberg (P9) is in a valley between
higher terrain. The steep rising topography of Dyrvedalen (P10) should force increased precipitation,
but this is not seen in the observations. It is believed to be because of the general reduced synoptic
precipitation inland, which also is detectable at Vasslii (P12). For Flyane (P11) this reduced synoptic
precipitation could potentially be washed out by a spill over effect.

5.4   Observational summary and conclusions

For the first time a precipitation dataset with fairly high horizontal resolution has been collected in
the area around Voss. It enabled a study of fine scale distribution in a rather complex mountainous
terrain. A terrain which previously, to our knowledge, has not been investigated on this level of detail.
The dataset includes a pre campaign from August to November 2013 and an extended main campaign

from May to November 2014.

Both campaigns indicate a large spatial variability in the total precipitation collected. On a synoptic scale a difference of 114 % was found between Vasslii (P12) and Hisdalen (P3), whereas a smaller mesoscale signal shows a total precipitation difference of up to 40 % on gauges located within a distance of 10 km.

The wind speed and direction are believed to have significant influences on the precipitation distribution. Therefore an investigation of the prevailing wind speeds and directions was performed. The prevailing precipitating wind directions are found to be from S-W, in agreement with previously campaign studies in Western Norway (e.g. Fagerlid (2007); Skjerdal (2009); Sulen (2009)). Situations with wind speeds at or below 6 ms^{-1} are responsible for more than 30 % of the observed precipitation in the coastal areas, possibly related to coastal convective situations and blocked conditions resulting in a upwind displaced precipitation pattern. Stations further inland have a larger portion of precipitation related to situations with wind speeds at or above 10 ms^{-1}, which is believed to represent unblocked situations. These events also have the largest horizontal variations and wind direction dependencies.

Investigation of the topography influence on the precipitation distribution has confirmed the established knowledge of the synoptic scale forced upslope ascent enhancement. For the smaller scales, additional signals of evaporative fohn effects and the competing spill over effects have been detected. By these observations this study has added value to the established knowledge of orographic modified precipitation.

However, the complexity of the terrain together with the relatively short observation periods makes the fine scale analysis difficult and to some degree incomplete. The area selected has shown large synoptic scale variability, and the interactions between mesoscale and synoptic scaled precipitation has made it difficult to identify clear mesoscale signals. Additionally it appeared to be a major challenge to find a wind dataset with sufficient temporal and horizontal resolution. The high variability amongst the available datasets reveals an uncertainty in the wind data, and the selected dataset is a compromise, which could have some influence on the analysis performed in this thesis.
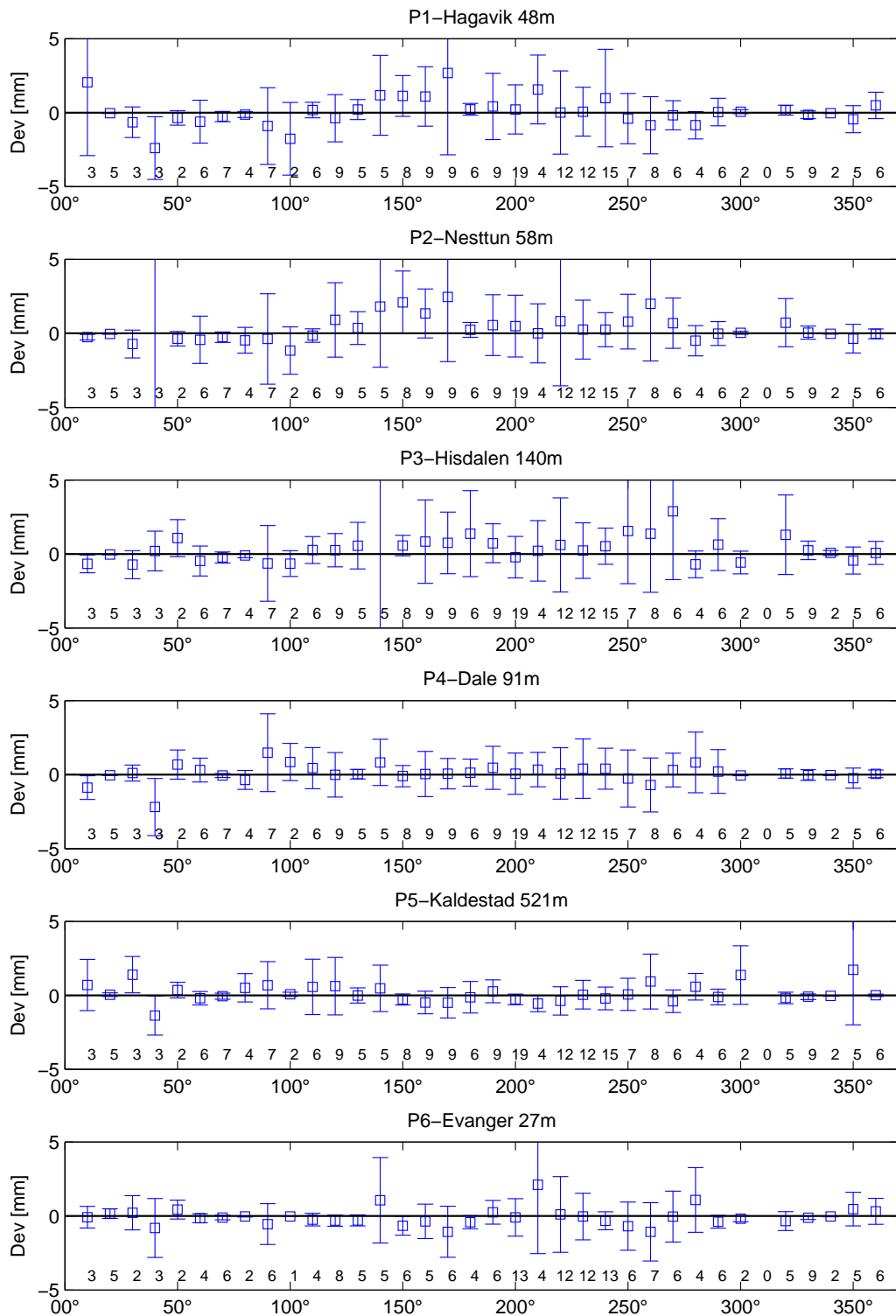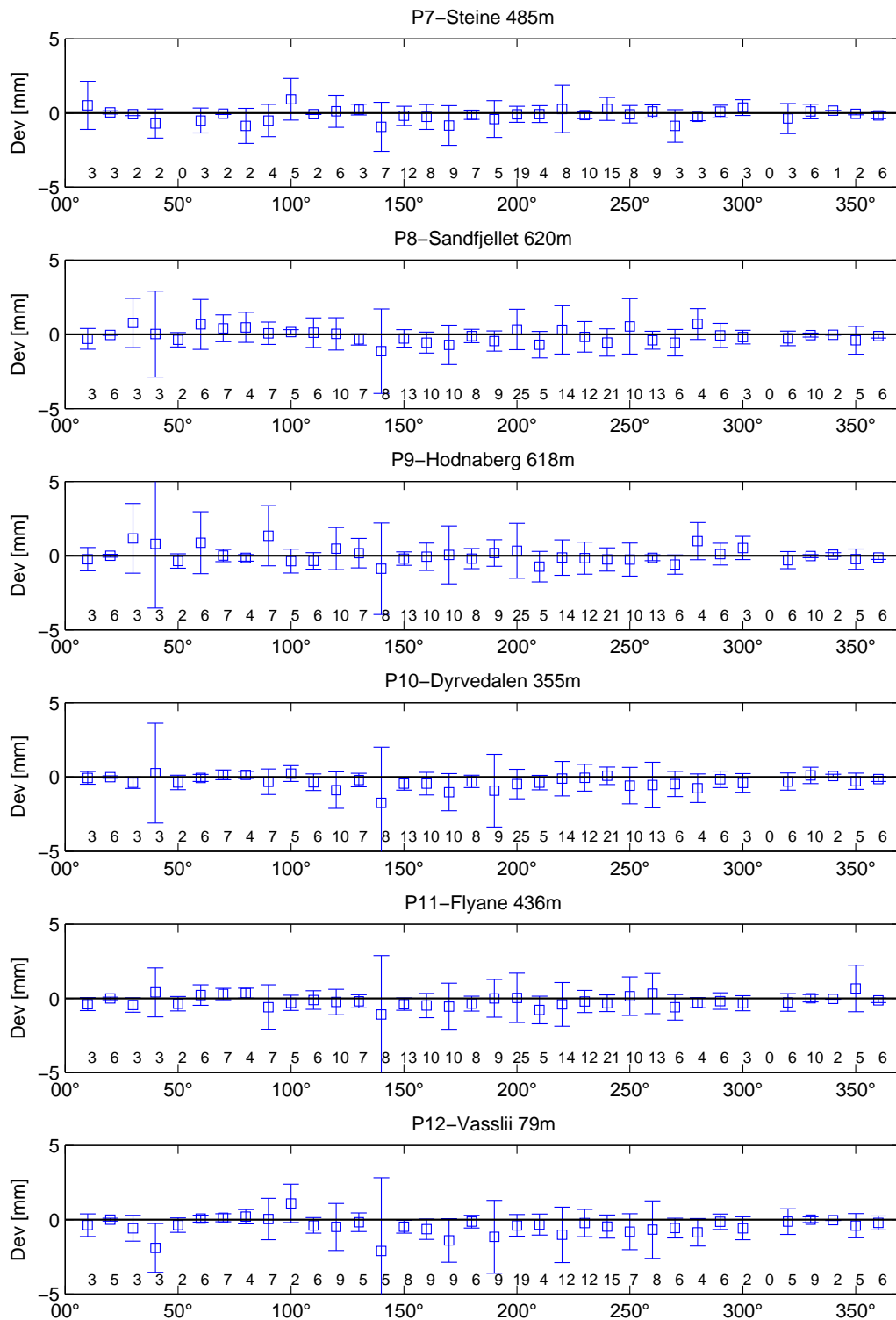
Figure 5.10: The deviation from mean precipitation on the stations during low wind precipitating events. Wind directions are denoted along the x-axis. Numbers correspond to numbers of 6 hour values included in the wind direction bin. Mean and whiskers of 1 σ are plotted.
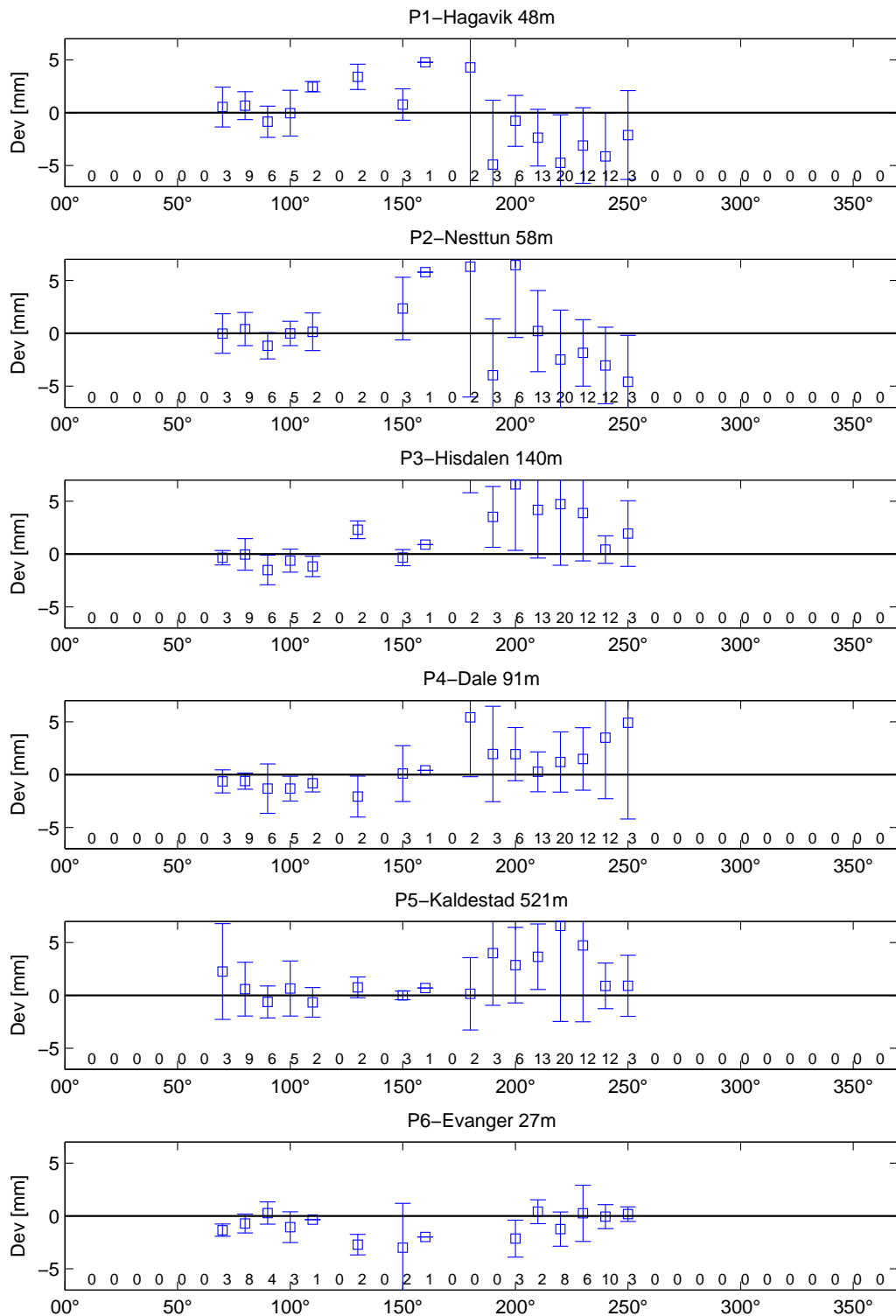
Figure 5.10: The deviation from mean precipitation on the stations during low wind precipitating events. Wind directions are denoted along the x-axis. Numbers correspond to numbers of 6 hour values included in the wind direction bin. Mean and whiskers of 1 σ are plotted.
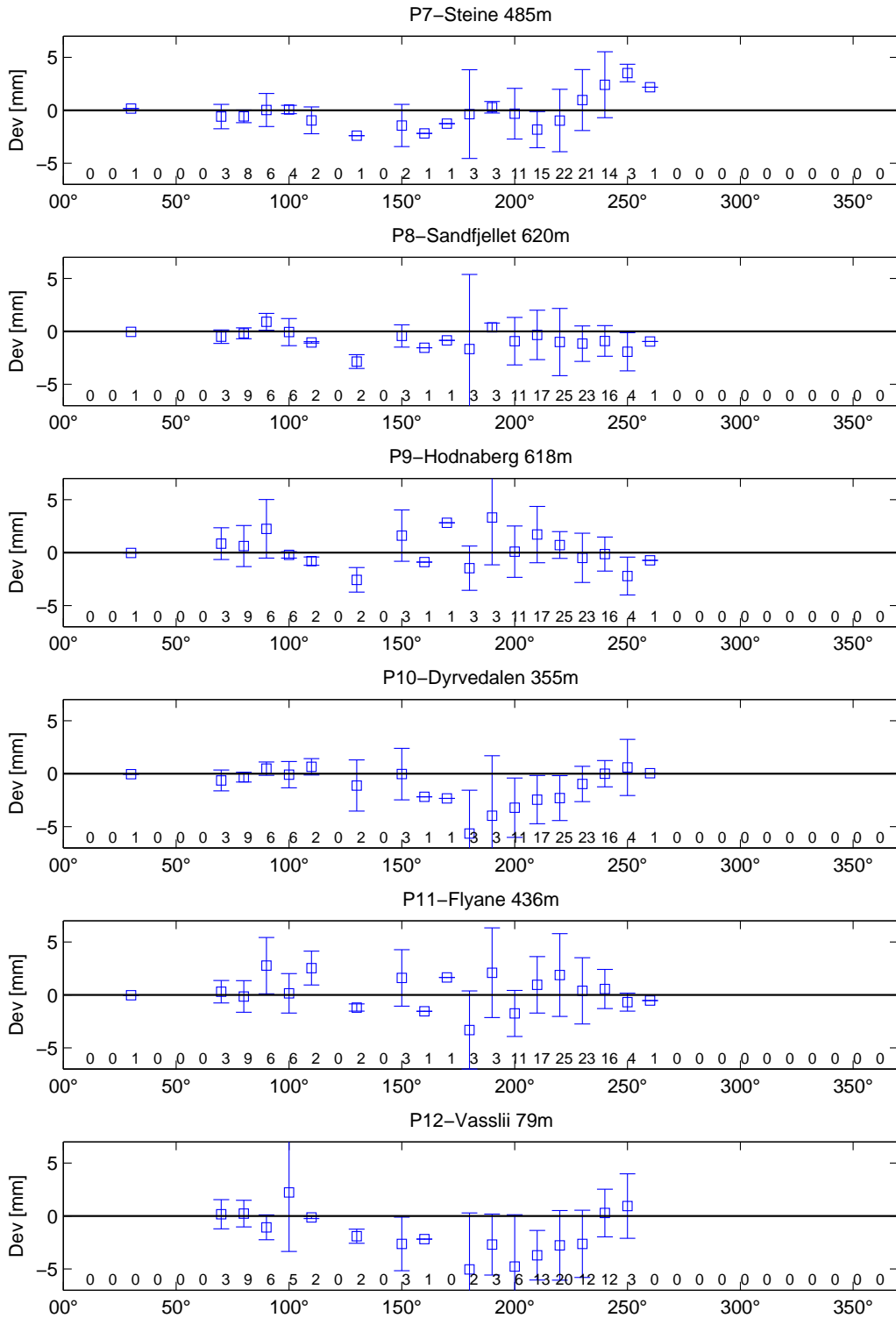
48

Figure 5.11: The deviation from mean precipitation on the stations during high wind precipitating events. Wind directions are denoted along the x-axis.Numbers correspond to numbers of 6 hour values included in the wind direction bin. Mean and whiskers of 1 σ are plotted.

49

Figure 5.11: The deviation from mean precipitation on the stations during , high wind precipitating events. Wind directions are denoted along the x-axis. Numbers correspond to numbers of 6 hour values included in the wind direction bin. Mean and whiskers of 1 σ are plotted.
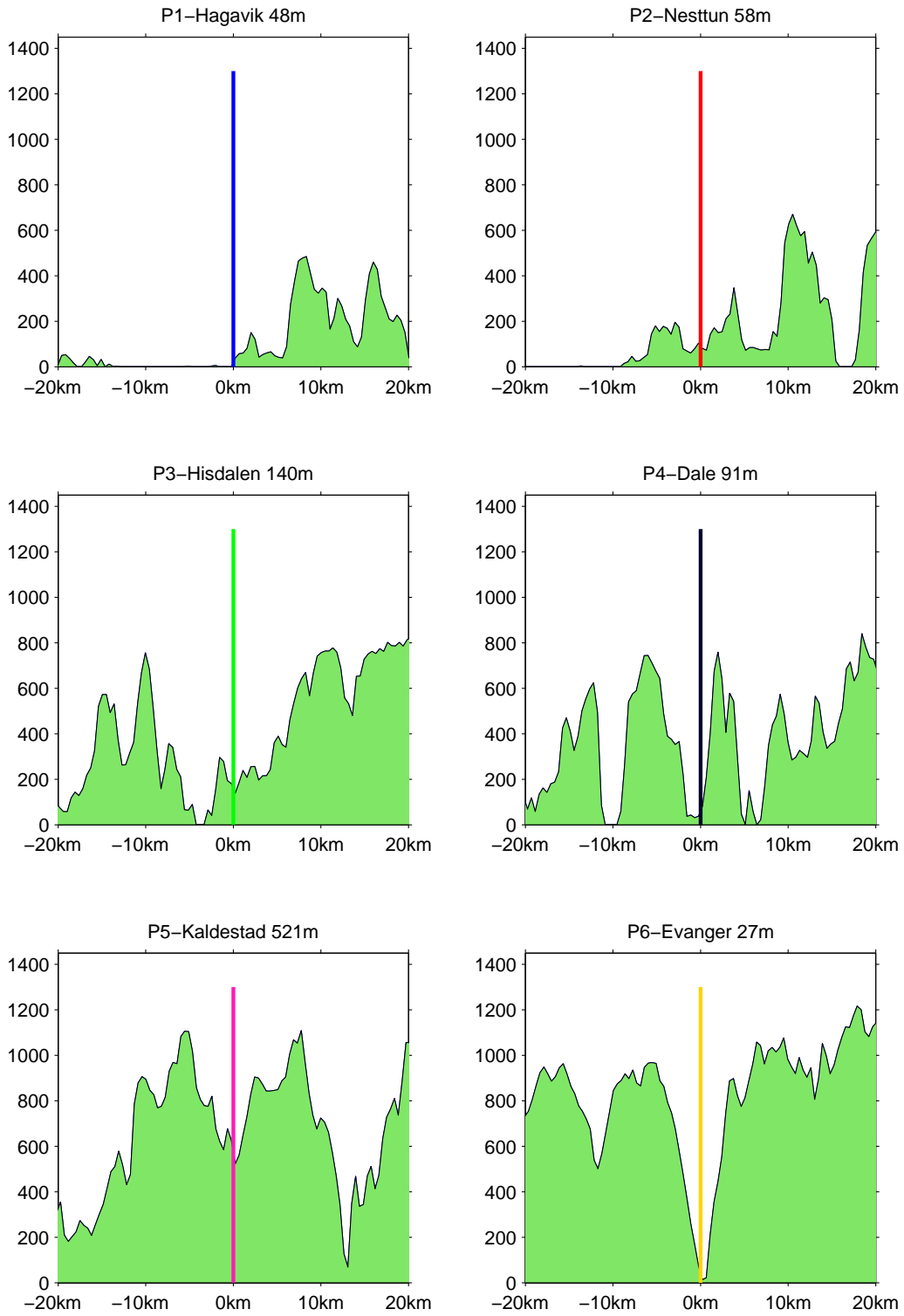
Profile direction 220° – 40°

Figure 5.12: Terrain profiles for stations P1-P6, direction is 220°.

Profile direction 220° – 40°

Figure 5.12: Terrain profiles for stations P7-P12, direction is 220°.

Chapter 6

# Case study of the flooding event

In late October 2014 several consecutive days of heavy precipitation caused widespread flooding in Western Norway. One of the hardest affected areas were located along the river Vosso, and the Voss area faced a 200 year flooding event on October 28. The official stations operated by Met.no in the area reported, between 6 UTC October 26 and 6 UTC October 29, a 3 day total precipitation of 111 mm for Voss, 133 mm for Evanger and 249 mm for Kvamskogen (Met.no). A combination of the large amounts of precipitation over several days, which saturated the top layers of the surface, and the fact that the surface was not yet covered by snow, which could have absorbed some of the water at higher elevations, resulted in large run off and a widespread flooding.

6.1 Synoptic situation

Figure 6.1 shows the surface analysis maps for 00 UTC from the 26th to the 29th of October. On the 26th an intense low pressure system with a core pressure of 963 hPa was located just S of Iceland. The following days the low pressure weakened and moved slowly towards E. Initially Norway was located on the E side of the low pressure system in a sector of SW strong winds, but towards the end of the period the winds were weakening and veering towards W. The frontal zones were more or less consistent from the subtropics to our latitudes and continuously forced warm and moist air from the Caribbean towards Western Norway. The moisture transport is confirmed in Figure 6.2 where the specific humidity in 850 hPa from the ERA-Interim reanalysis is depicted.

The weather situation in the study area during the 4 days was characterized by the passage of multiple frontal systems associated with in part heavy precipitation. A diffuse frontal system with instabilities was situated over Western Norway on October 26. The system led to considerable amounts of precipitation during the day, especially around noon. A cold front passed the area at 00 UTC, October 27 leading to a relatively dry period behind the front. Meanwhile, the disturbance over Scotland grew and moved towards Norway, which situated Western Norway in a warm sector with large amounts of continuous precipitation from 12 UTC, October 27 to 17 UTC, October 28. The associated cold front
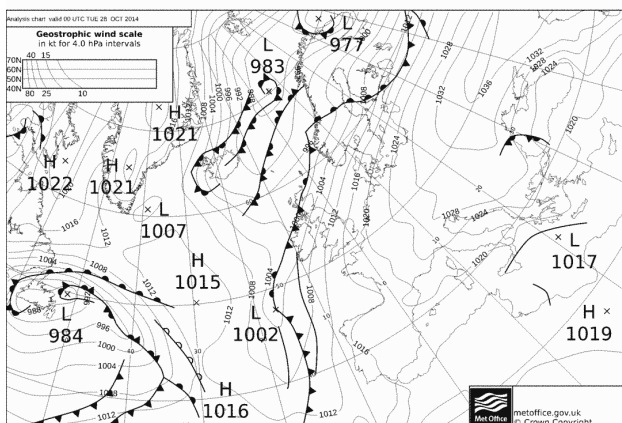
passed the Bergen area in the afternoon and precipitation amounts decreased behind. The result of several days of more or less continuously precipitation, was a flooding top in the early evening October 28.
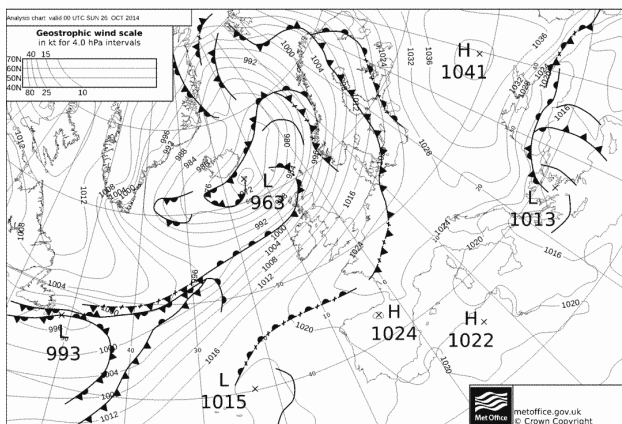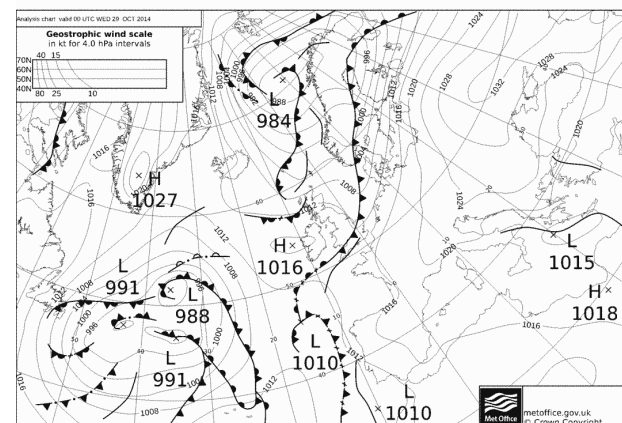

(a) 26th of October 00 UTC.
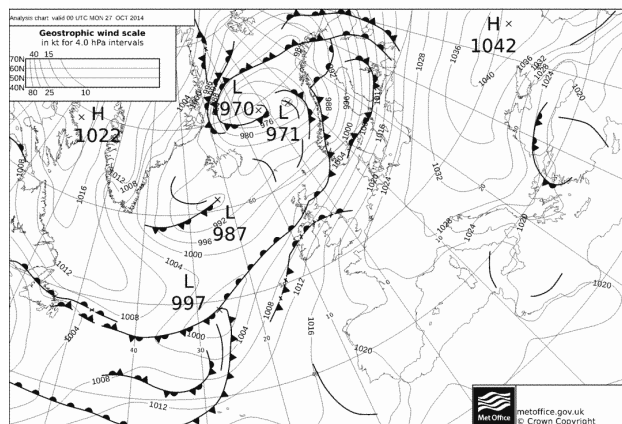
(b) 27th of October 00 UTC.

(c) 28th of October 00 UTC.

(d) 29th of October 00 UTC.

Figure 6.1: Surface analysis charts from UK Metoffice, valid at 00 UTC on October 26-29. Downloaded from http://www.wetterzentrale.de/topkarten/tkfaxbraar.htm.

6.2 Measurements

Figure 6.3 presents the corresponding observations from 00 UTC, October 25 to 00 UTC, October 29. It shows the accumulated precipitation of the 11 stations operational during the campaign, based on
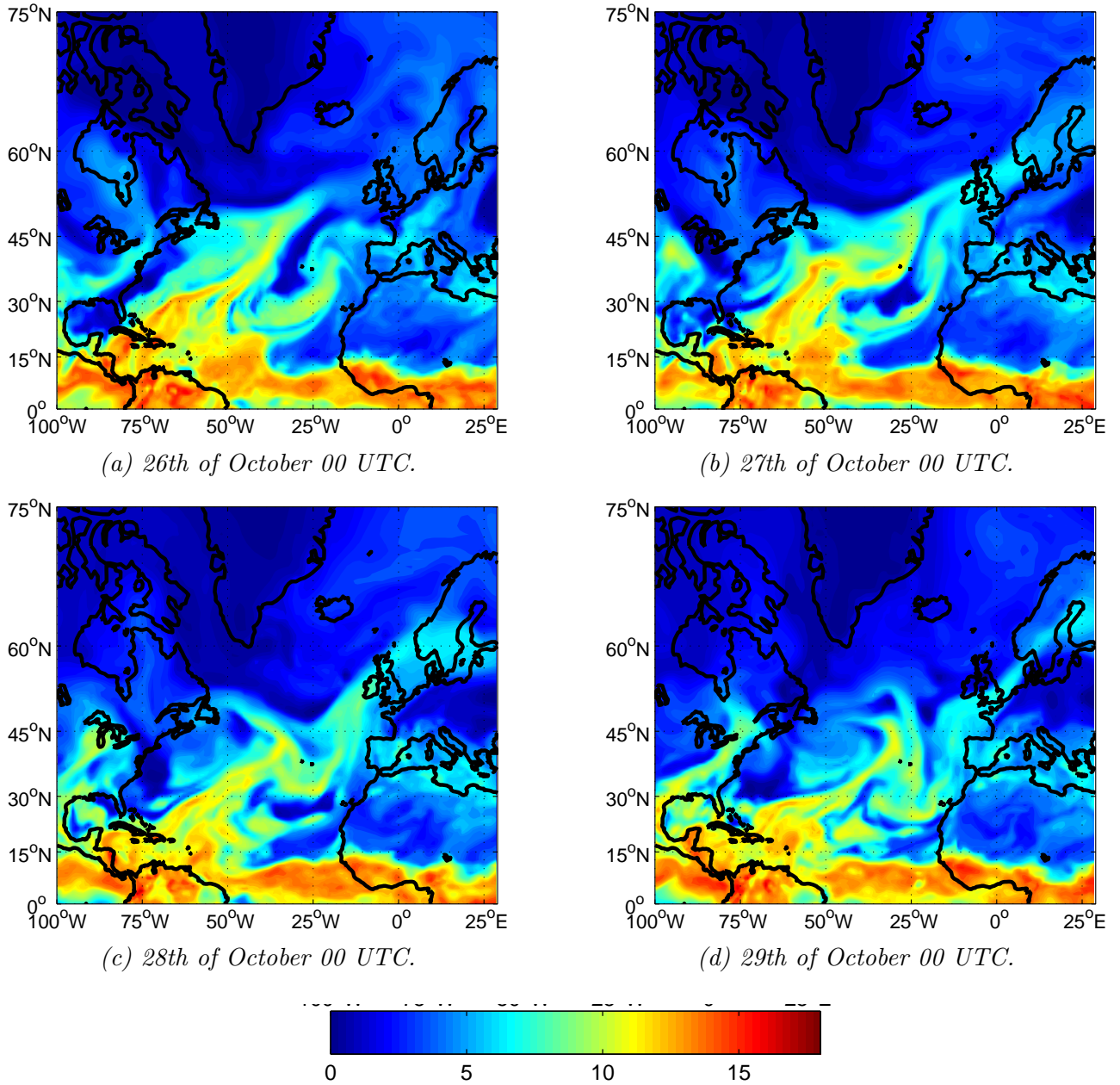
(a) 26th of October 00 UTC.

(b) 27th of October 00 UTC.

(c) 28th of October 00 UTC.

(d) 29th of October 00 UTC.

Figure 6.2: Specific humidity [g kg^{-1}] at 850 hPa during the flooding event. Data is from the ERA-Interim reanalysis.

an integration period of 1 hour. The wind from the ERA-Interim reanalysis is presented in the upper panel of the figure. The precipitation measurements show a large areal variability. The coastal station Hagavik (P1) collected a total of 96 mm of precipitation, whereas Kaldestad (P5) received 338 mm, i.e. a factor of 3.5 higher, or an absolute difference of 242 mm.
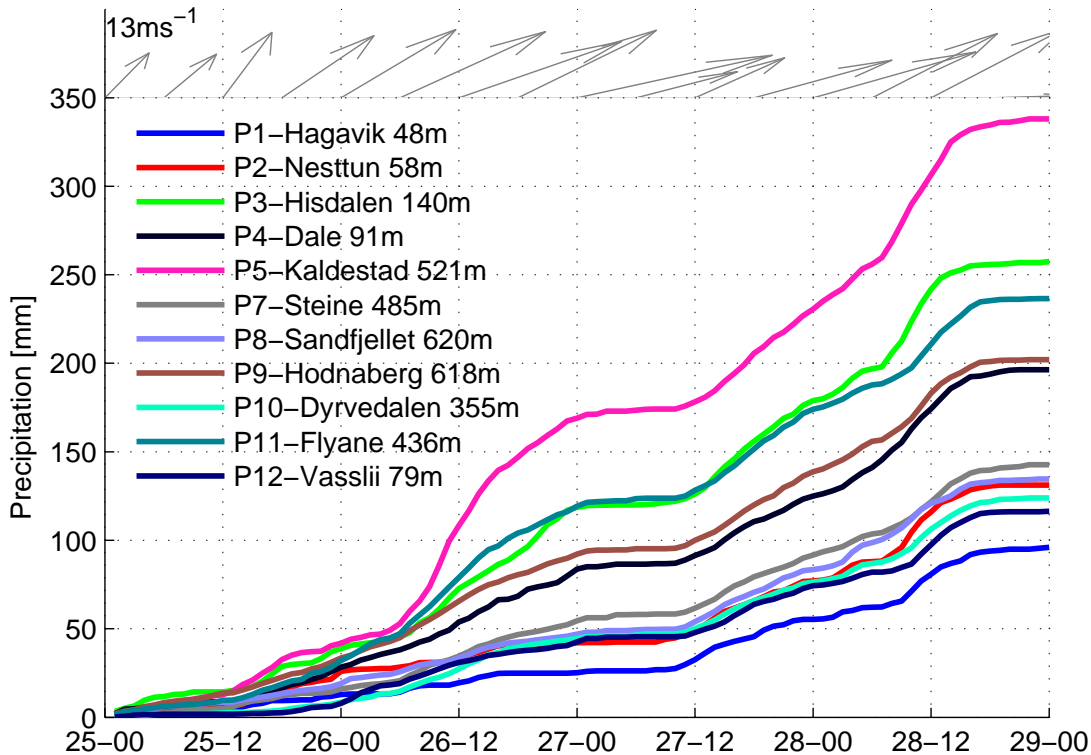

Figure 6.3: The accumulated precipitation during the 200 year flooding event in Voss (lower panel) together with the wind reanalysis from ERA-Interim (upper panel). The temporal resolution is 1 hour for the precipitation and 6 hours for the wind.

6.3   WRF model runs

The extended rain gauge network deployed for this master thesis provides a unique data set for model validation. For sensitivity testing different model runs have been performed to investigate the effects of terrain smoothing, spectral nudging and horizontal grid resolution on the model results. The model set up is described in detail in Section 4.2. Table 6.1 shows the variable settings for the sensitivity runs performed. The model was initiated at 00 UTC, October 24. 24 hours of spin up time have been removed, resulting in an analysis window from 00 UTC, October 25 to 00 UTC, October 29. To compare the results against observed precipitation, grid points have been chosen to represent the observational stations as described in Section 4.2.1. In the following these grid points and the

observational stations will be presented as station number, e.g. P1-P12, instead of the full station name.

Table 6.1: Settings for the model runs. 1-2-1 smoothing (1-2-1) was conducted with 3 passes and smth-desmth special (sds) was conducted with 2 passes.

Terrain Smoothing	Nudging Coefficient [s^{-1}]	Relaxation time [h]	Wavelengths [km] Zonally (Z), Meridionally (M)
sds	3.0×10^{-4} s^{-1}	1	> 903km Z, 812km M
sds	3.0×10^{-4} s^{-1}	1	> 677km Z, 609km M
sds	3.0×10^{-4} s^{-1}	1	> 338km Z, 304km M
sds	4.62×10^{-5} s^{-1}	6	> 677km Z, 609km M
sds	1.16×10^{-5} s^{-1}	24	> 677km Z, 609km M
sds	No nudging	N/A	N/A
1-2-1	3.0×10^{-4} s^{-1}	1	> 677km Z, 609km M
1-2-1	1.16×10^{-5} s^{-1}	24	> 677km Z, 609km M
1-2-1	No nudging	N/A	N/A

The total accumulated precipitation from the second option in Table 6.1 is shown as an example in Figure 6.4. This model run is chosen because of its overall lowest RMSE, compared to the remaining model runs. This will be presented in Section 6.5. A comparison of Figure 6.3 and Figure 6.4 reveals a rather good representation of the observed precipitation values. Overall the model seems to be able to reproduce the horizontal variability well. This variability is also presented later in Figure 6.17.

6.3.1 Topography smoothing

The steep topography and the high horizontal resolution of domain 3 made a smoothing of the topography necessary (See Section 4.2). To investigate the influence of the smoothing, two WRF smoothing options were compared. Figure 6.5 shows the more smoothed 1-2-1 option with three terrain passes with the less smoothed smth-desmth special with two terrain passes. The 1-2-1 smoothing was run with a 5 second time step whereas the smth-desmth special was run with time steps of 3 seconds to avoid stability issues during the integration.

Figure 6.6 shows a comparison of the accumulated precipitation for the two smoothing options with the observations. In general the choice of the smoothing option seems only to have a minor effect. The largest total deviations between model outputs were found at stations P7, P10 and P11 and were in the order of 10 % or below. Comparing the model results against the observed precipitation amounts it is surprising that the less smoothed option seems to overestimate P5 and P11. At these stations the more smoothed option represents the point precipitation better. Both stations are possibly affected by spill over effects, the overestimation could potentially be related to this phenomena. At P8 both
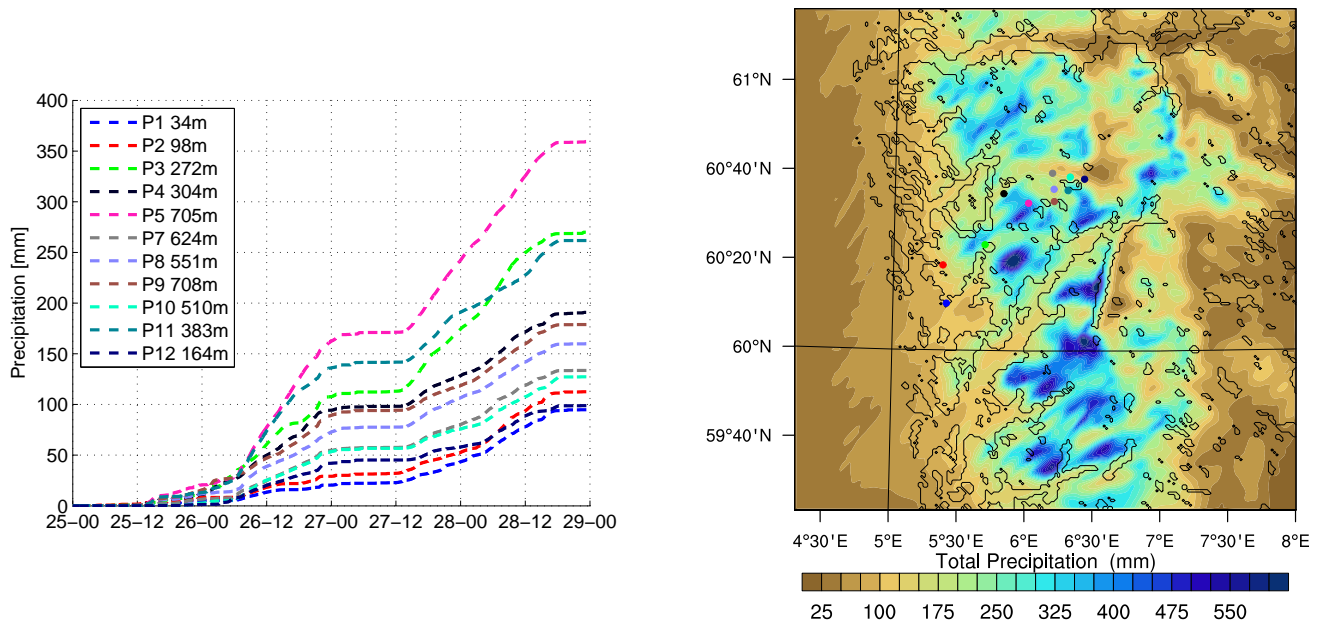
Figure 6.4: Time series of the accumulated model precipitation at each station with model altitude in the legend (left panel), and accumulated precipitation over the entire event in the inner domain with the campaign stations marked with colored dots (right panel). The data are from the model run with the smth-desmth special smoothing option, spectral nudging on wavelengths longer than 677 km zonally and 609 km meridionally, a relaxation time of 1 hour and a grid resolution of 1 km.

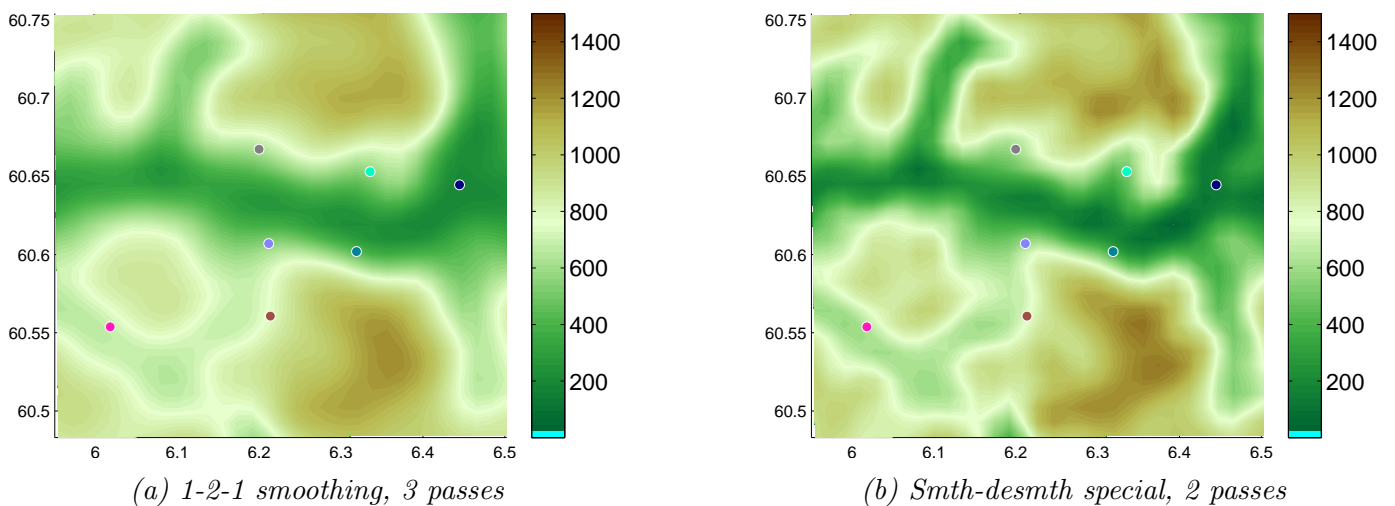(a) 1-2-1 smoothing, 3 passes
(b) Smth-desmth special, 2 passes

Figure 6.5: Visualization of the two terrain smoothing option compared. The area shown is part of the innermost domain in the WRF simulation, this part includes 7 of the campaign stations, each marked with a colored dot.

model runs overestimate the observed precipitation, whereas other stations as P2, P9 and P12 seem to be underestimated during the entire integration time.

A comparison of RMSE and ME for each station is presented in Table 6.2. The RMSE and ME are shown as a percentage of the total observed precipitation. Hourly values have been used for the calculation. Positive ME indicates that the model is overestimating precipitation. Altitude differences between GPS altitude and a mean of the 5 grid cells used for the station calculations in domain 3 (See Section 4.2.1) are also given in Table 6.2. Positive values indicate higher terrain in the WRF topography than indicated by GPS at the corresponding station.

Both smoothing options have RMSE values below 10 % for most stations. Only P2 and P8 have larger RMSE and ME. Judging by RMSE, 8 out of 11 stations increase altitude accuracy by a decrease in the terrain smoothing. The gain in altitude precision by less smoothing is however limited, for P3 it is even deteriorated. For the stations mainly in mountainous terrain (P7-P10), RMSE and ME are reduced when the topography is less smoothed, their station altitudes are also slightly better reproduced in the less smoothed option. Stations P11 and P12 have lowest RMSE and ME in the more smoothed option, this is a bit surprising, but corresponds with the visualization in Figure 6.6. Especially P11 shows a deterioration in the less smoothed option, which was expected to represent the precipitation better. All further investigation have been done based on the model runs with the less terrain smoothed option due to its more accurate representation of the mountainous topography and stations.

Table 6.2: RMSE and ME [%] for topography smoothing. Δz is given by the difference between the mean of the 5 grid points used from WRF domain 3 and the GPS altitude of the stations. Lowest RMSE are marked in bold.

| Station	1-2-1			Smth-desmth special		
	RMSE	ME	Δz [m]	RMSE	ME	Δz [m]
P1	**7.04**	-6.11	+5	7.75	-6.46	-3
P2	**10.85**	-9.92	+53	12.81	-11.86	+31
P3	**5.06**	-2.87	+101	5.19	-2.76	+116
P4	5.33	+0.13	+337	**4.31**	-0.70	+260
P5	**4.96**	-3.11	+205	5.26	-1.27	+181
P7	7.31	-6.02	+129	**5.32**	-4.48	+132
P8	15.67	+10.81	-93	**13.77**	+8.54	-78
P9	9.64	-8.2	+154	**7.62**	-6.81	+120
P10	6.14	-4.64	+243	**4.06**	+0.43	+192
P11	**3.52**	-1.37	+18	6.80	2.49	-39
P12	**7.58**	-5.96	+125	8.50	-6.77	+87
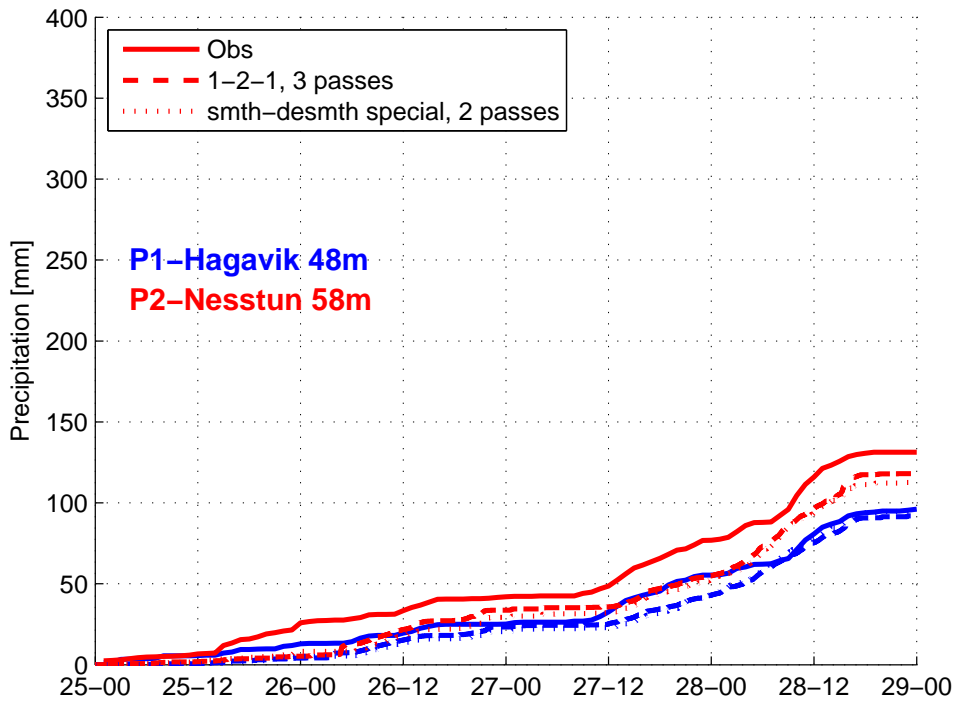
(a) Comparison for the two coastal stations.
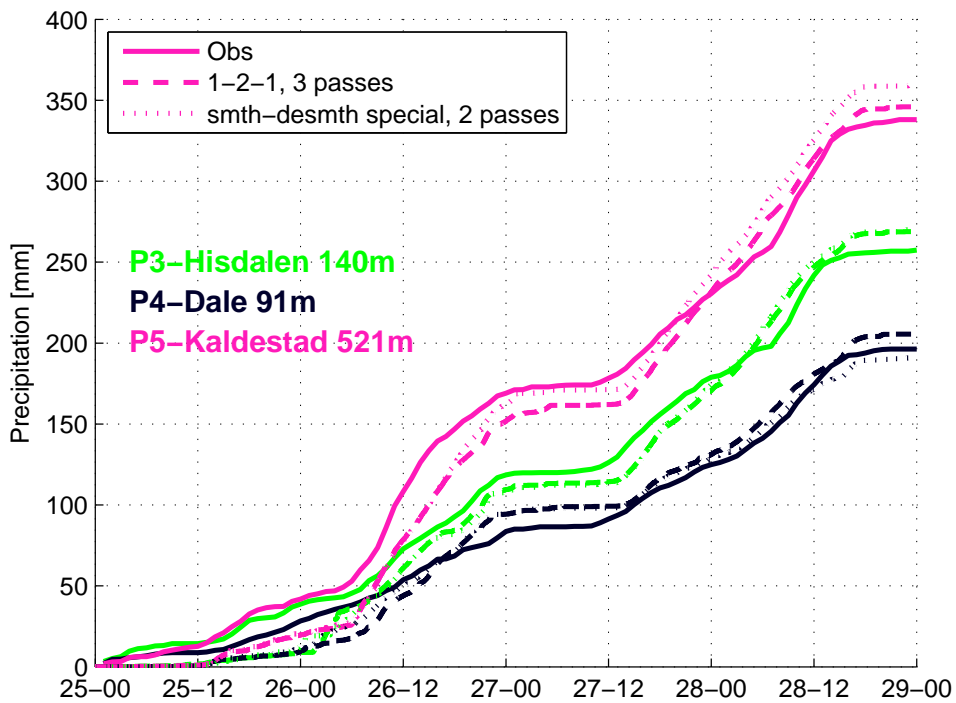
(b) Comparison for the three steep terrain stations.
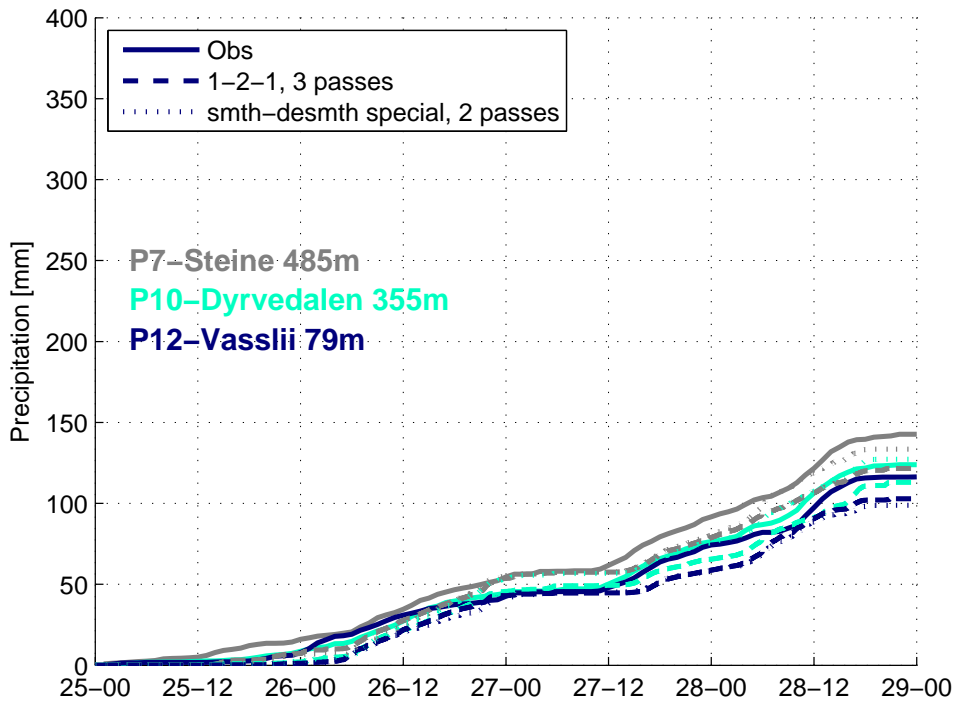
(c) Comparison for the three stations north in the valley.
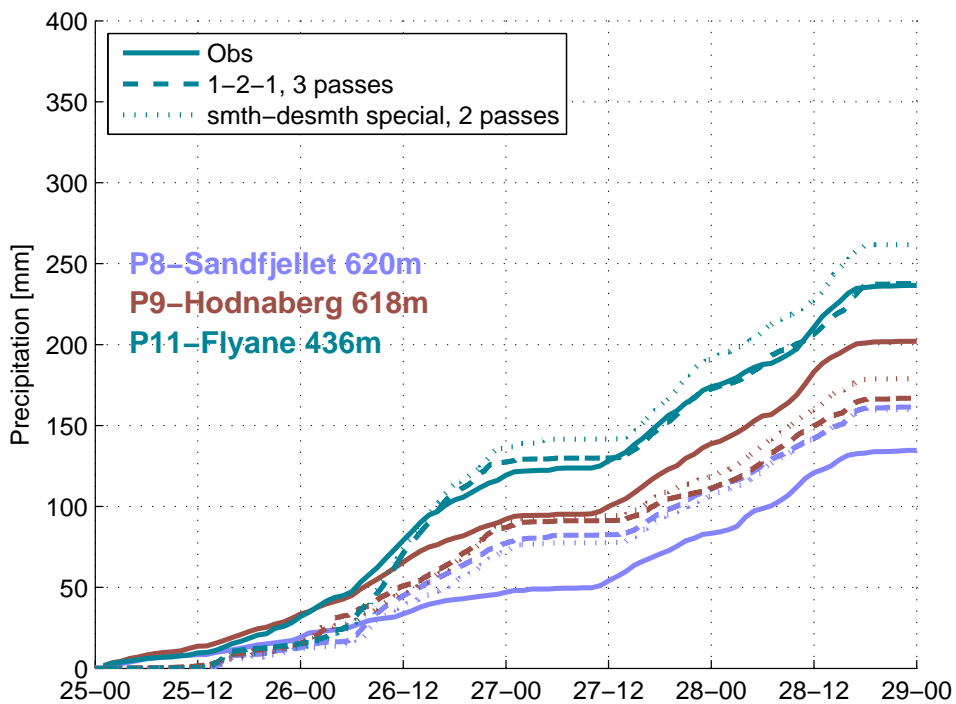
(d) Comparison for the three mountain stations.

Figure 6.6: Topography smoothing and its effect on point precipitation at the campaign stations.

## 6.3.2 Spectral nudging options - effect of wavelengths

As already discussed in Section 4.1.8 one disagreement is whether nudging including shorter wavelengths destroys the models ability to represent extremes (Alexandru et al., 2009; Glisan et al., 2013). In the following the sensitivity to spectral nudging, using 3 different cut-off wavelengths, is investigated. The shortest cut-off wavelengths are in the lower part of the expected minimum resolved wavelengths in the driving dataset[1]. In all cases a grid resolution of 1 km and a relaxation time of 1 hour were used, because of the lowest overall RMSE and MAE as presented later in Table 6.4 and Section 6.5.

Figure 6.7 presents the time series for the inner domain. The shortest cut-off wavelengths produces the highest precipitation amounts and overestimates the precipitation on most inland stations. The two other options are more comparable with each other and the observations. The largest discrepancies between the different cut-off wavelengths are found at the steep terrain stations, where also the largest precipitation amounts are observed. Table 6.3 presents the RMSE and ME values for each station. The table supports the overestimating with short cut-off wavelengths. Only the coastal stations and P12 have their lowest RMSE and ME for this choice. RMSE and ME reduces in general with longer cut-off wavelengths at inland stations. This indicates that the model precipitation is dependent on smaller scales, developed freely in the model with less nudging. On the other hand, the coastal stations are better represented when nudged at shorter wavelengths. Most of the precipitation there is related to synoptic scales, already appropriately resolved in the initial and boundary conditions.

Table 6.3: RMSE and ME [%] for nudged wavelengths. For all nudged cases a relaxation time of 1 hour (coefficient of 3.0×10^{-4} s^{-1}) was applied. Lowest RMSE are marked in bold.

Station	> 338 km Z, 304 km M		> 677 km Z, 609 km M		> 903 km Z, 812 km M	
	RMSE	ME	RMSE	ME	RMSE	ME
P1	**5.34**	+0.28	7.75	-6.46	10.07	-8.62
P2	**8.05**	-6.55	12.81	-11.86	13.44	-12.21
P3	8.09	+1.84	**5.19**	-2.76	6.05	-0.69
P4	11.20	+7.50	4.31	-0.70	**3.74**	-2.26
P5	8.40	+3.28	**5.26**	-1.27	5.38	-1.25
P7	5.40	+0.92	5.32	-4.48	**5.00**	+0.54
P8	19.38	+12.72	13.77	+8.54	**11.53**	+5.85
P9	7.84	-6.98	**7.62**	-6.81	12.04	-10.82
P10	10.16	+6.11	**4.06**	+0.43	4.09	-1.85
P11	6.22	+2.38	6.80	+2.49	**4.87**	-2.22
P12	**6.18**	-4.36	8.50	-6.77	8.84	-7.14

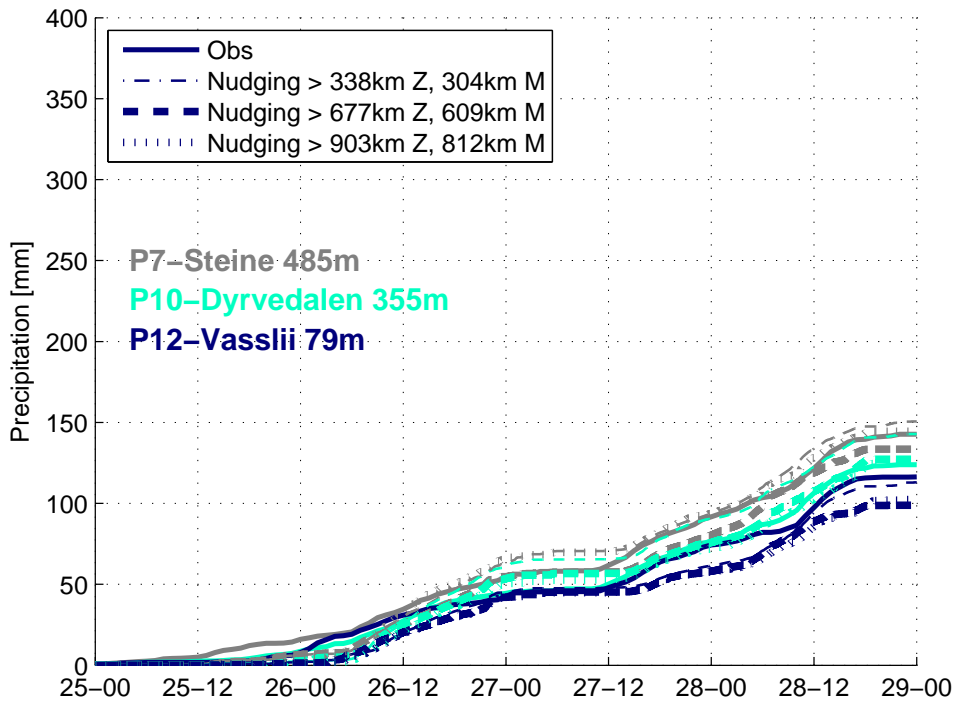[1]Minimum resolved wavelengths are expected to be approximately 10 × gridsize, which is 0.75° (Warner, 2011)
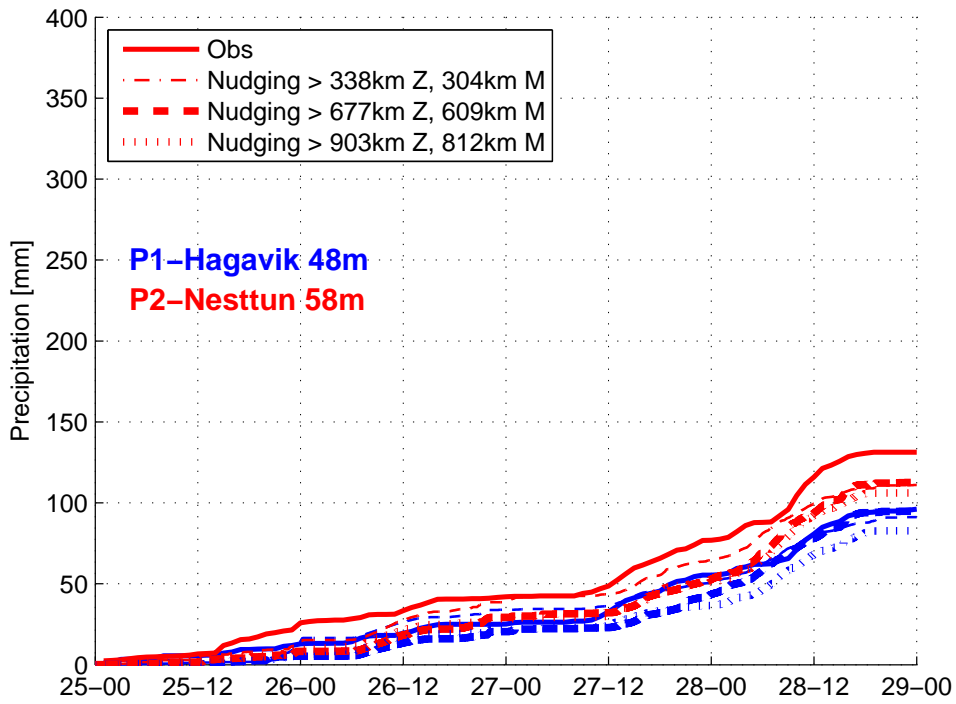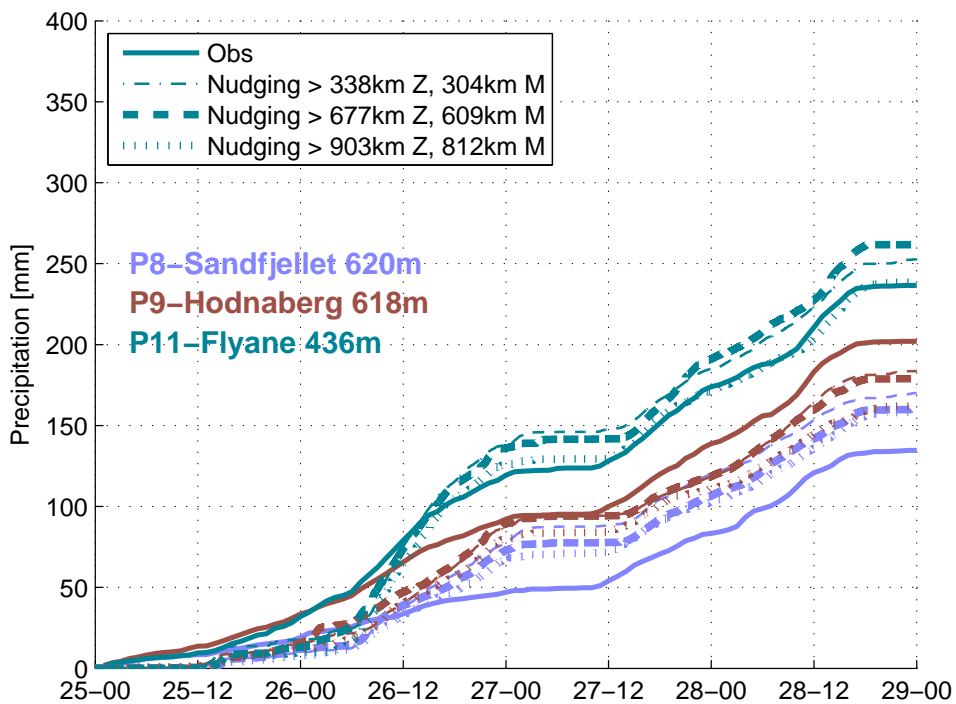
(a) Comparison for the two coastal stations.
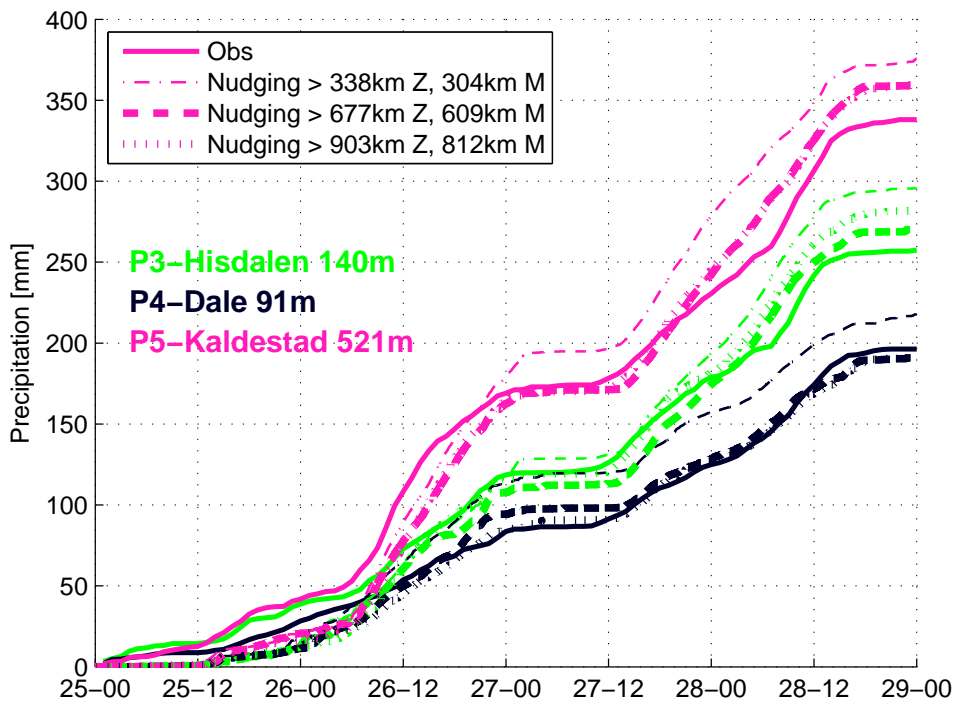
(b) Comparison for the three steep terrain stations.

(c) Comparison for the three stations north in the valley.

(d) Comparison for the three mountain stations.

Figure 6.7: Nudged wavelengths and its effect on point precipitation at the campaign stations.

6.3.3 Spectral nudging options - relaxation time effect

Model runs with three different relaxation times have been performed. The comparison of the results for the inner domain with a grid resolution of 1 km are presented in Figure 6.8. The figure shows all time steps for the three relaxation times. The model shows some sensitivity to the relaxation times. Generally the largest sensitivity is between the 1 hour and the 24 hour relaxation times. The model predicted precipitation varies with 3 % as a minimum at P3 to a maximum P11 where the 1 hour relaxation time produces 21 % more precipitation than the 24 hour option. The largest variations, all above 10 % are found at P1, P2, P10 and P11. At all these stations the 1 hour relaxation time produces the highest precipitation amounts. Comparing against the observed precipitation values, the 24 hour relaxation time run seems to perform poorest. The remaining two options show comparable performances, with a slightly better performance for the 1 hour relaxation time run.

Table 6.4 presents RMSE and ME for each station, including also a run without nudging. Judging by RMSE, 9 out of 11 stations gain predictability by the use of spectral nudging. 5 of those improve with the WRF standard nudging coefficient compared to a longer relaxation time. Only P12 lacks improvement in RMSE and ME when using nudging.

Table 6.4: RMSE and ME [%] for relaxation times, nudging coefficients in parenthesis. When applicable the wavelengths longer than 677 km zonally and 609 km meridionally were nudged. Lowest RMSE are marked in bold.

| Station	No nudging		24 h (1.16×10^{-5} s^{-1})		6 h (4.62×10^{-5} s^{-1})		1 h (3.0×10^{-4} s^{-1})	
	RMSE	**ME**	**RMSE**	**ME**	**RMSE**	**ME**	**RMSE**	**ME**
P1	12.55	-10.29	13.84	-11.90	**7.34**	-6.64	7.75	-6.46
P2	16.57	-14.34	16.13	-14.25	**10.48**	-9.71	12.81	-11.86
P3	6.68	-6.78	5.27	-3.90	5.72	-2.76	**5.19**	-2.76
P4	9.34	-8.26	5.41	-4.24	8.15	-7.32	**4.31**	-0.70
P5	5.38	-4.82	**5.05**	-3.94	6.48	-4.66	5.26	-1.27
P7	**3.86**	-0.68	5.00	+0.94	4.95	+0.47	5.32	-4.48
P8	19.69	+13.95	14.40	+9.04	13.90	+7.69	**13.77**	+8.54
P9	8.20	-7.10	11.46	-10.24	12.45	-11.36	**7.62**	-6.81
P10	5.24	-4.07	8.67	-7.64	5.98	-4.94	**4.06**	+0.43
P11	8.17	-6.94	10.79	-9.33	**6.03**	-5.31	6.80	+2.49
P12	**7.43**	-5.68	12.81	-10.76	10.89	-9.33	8.50	-6.77

6.3.4 WRF grid resolution

The ability of the model to reproduce local extremes is important for forecasting devastating events caused by heavy precipitation, as e.g. flooding and landslides. However the computational demands
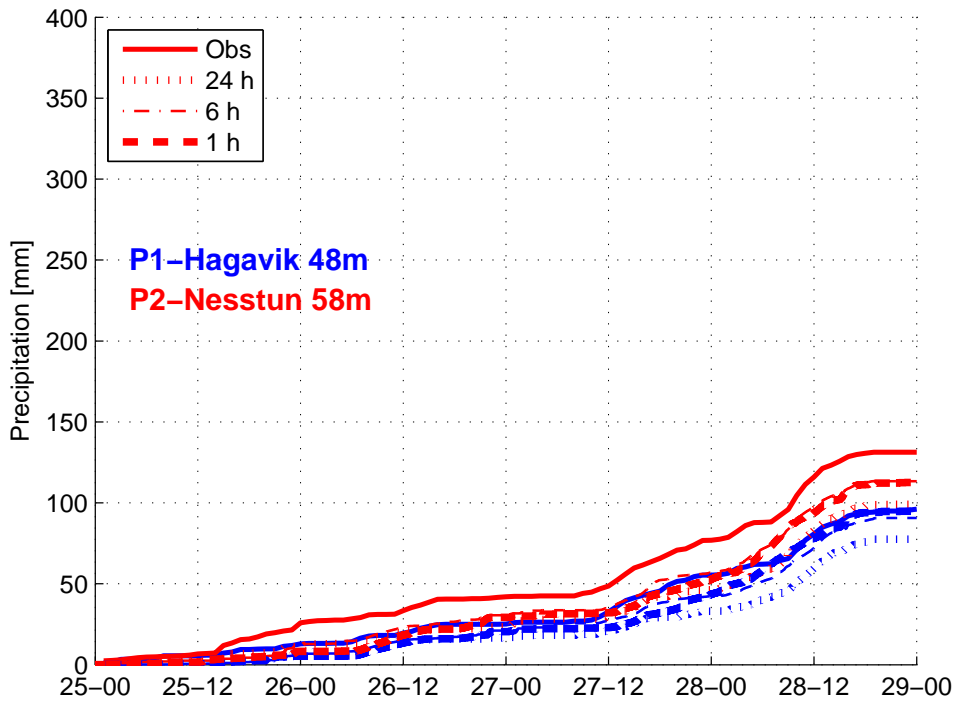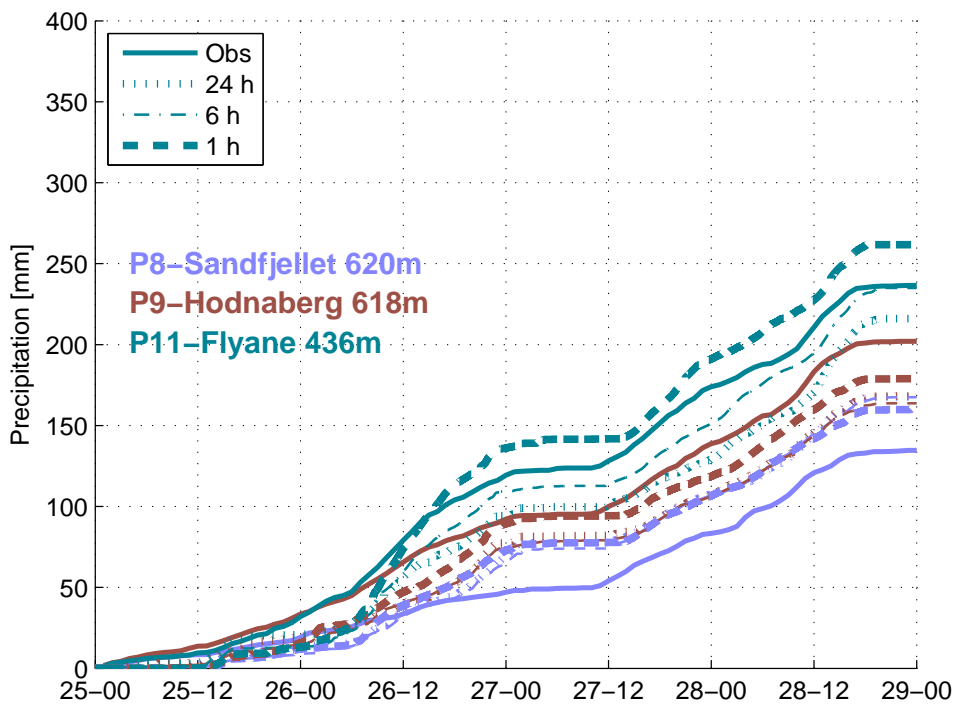
(a) Nudging comparison for the two coastal stations.
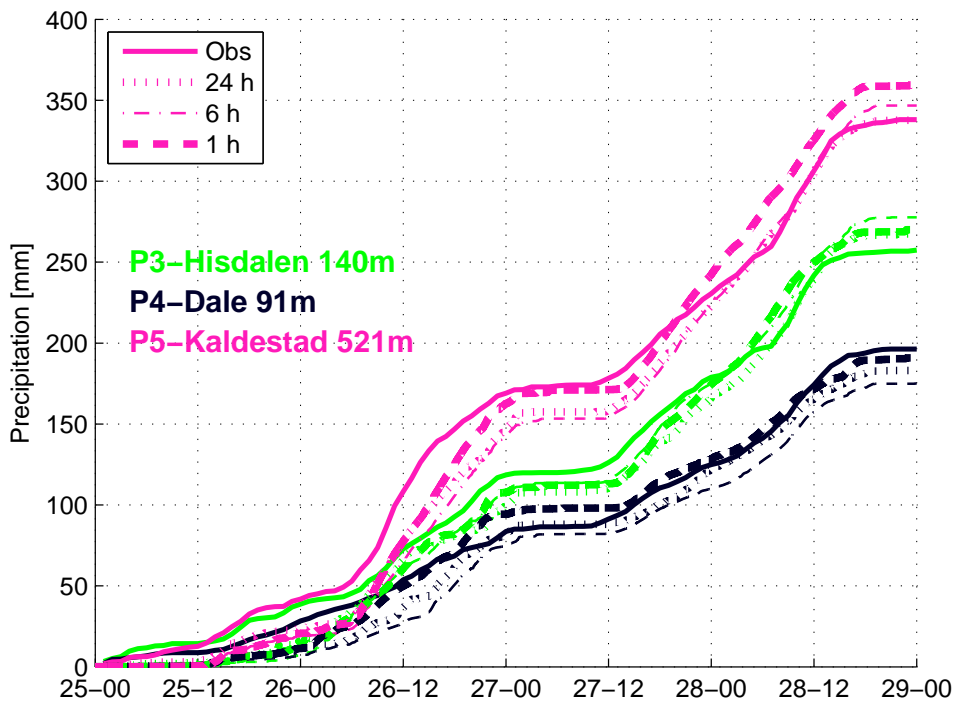
(b) Nudging comparison for the three steep terrain stations.
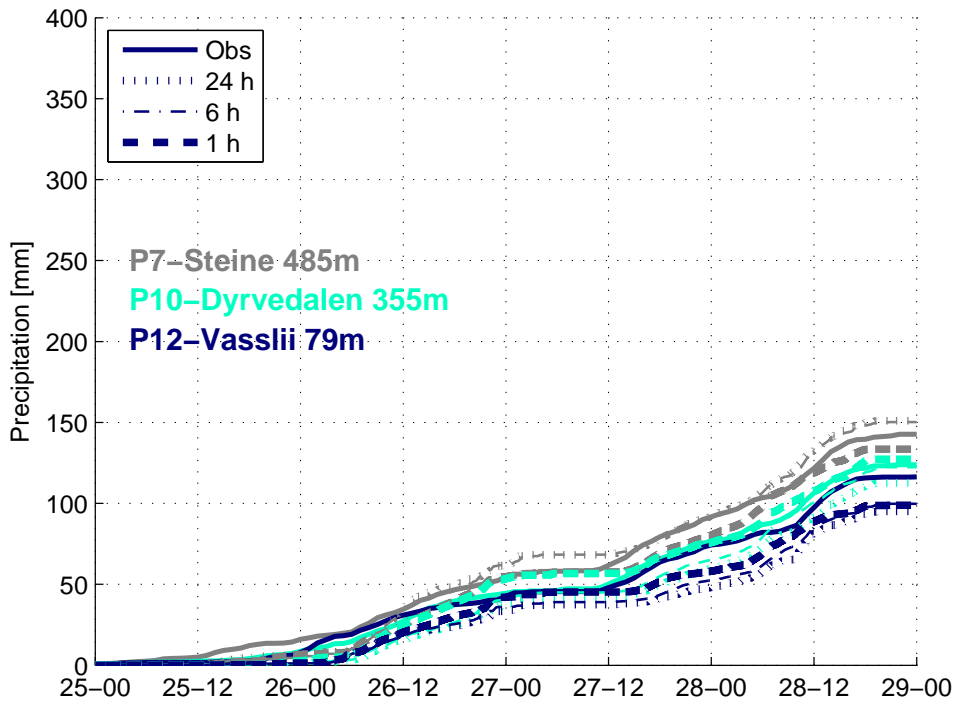
(c) Nudging comparison for the three stations north in the valley.

(d) Nudging comparison for the three mountain stations.

Figure 6.8: Different relaxation times and its effect on point precipitation.

are increasing by a factor of approximately 16 as the horizontal resolution is doubled[2]. It is therefore of great importance to determine the ideal grid resolution, reducing the computational demands, but yet still ensuring a model which is able to reproduce the extremes satisfactorily. In this paragraph the ERA-Interim reanalysis and 3 different grid resolutions from the WRF simulation are compared. Figure 6.9 presents the comparison of the observed precipitation on the stations versus the downscaled values for each resolution. The model run with a relaxation time of 1 hour and cut-off wavelengths of 677 km zonally and 609 km meridionally has been chosen because of its best overall performance presented in Section 6.5.

The model dependency on grid resolution is evident. Precipitation at stations, P2, P8, P10 and P12 is already well resolved in ERA-Interim and even deteriorates slightly when downscaled. These are all stations with a relatively low observed precipitation amount. For the steep terrain stations (P3 and P5) with large amounts of observed precipitation, the downscaling is crucial. The precipitation is more than doubled, and it corresponds well with observations in the 1 km resolution domain. Table 6.5 presents RMSE and ME. The stations with the highest amount of precipitation are best represented in the 1 km resolution. However the gain compared to the 3 km resolution is relatively small. The ERA-Interim underestimates precipitation considerably, shows large RMSE and fails to capture the lateral inhomogeneity in precipitation.

Table 6.5: RMSE and ME [%] for the different grid resolutions used. For all grid resolutions wavelengths larger than 677 km zonally and 609 km meridionally were nudged with a relaxation time of 1 hour. Lowest RMSE are marked in bold.

| Station	1 km		3km		9km		ERA-Interim	
	RMSE	ME	RMSE	ME	RMSE	ME	RMSE	ME
P1	**7.75**	-6.46	8.01	-6.84	8.05	-7.08	22.03	+16.35
P2	12.81	-11.86	15.09	-13.80	9.83	-8.63	**5.21**	-1.33
P3	**5.19**	-2.76	9.37	+3.66	10.87	-10.20	30.30	-25.79
P4	**4.31**	-0.70	5.24	+0.59	7.34	+1.80	19.31	-16.79
P5	**5.26**	-1.27	6.66	+1.32	9.33	-8.50	37.11	-31.20
P7	5.32	-4.48	**3.96**	-1.90	11.01	+6.94	8.30	-7.32
P8	13.77	+8.54	7.11	+1.63	15.55	+9.60	**5.93**	-4.89
P9	7.62	-6.81	9.77	-8.93	**6.45**	+0.64	24.44	-21.72
P10	4.06	+0.43	4.14	+0.63	37.43	+28.45	**2.05**	-0.00
P11	**6.80**	+2.494	11.92	+6.96	12.18	-11.36	30.72	-26.48
P12	8.50	-6.77	18.40	-15.20	42.68	+31.99	**3.02**	+0.00

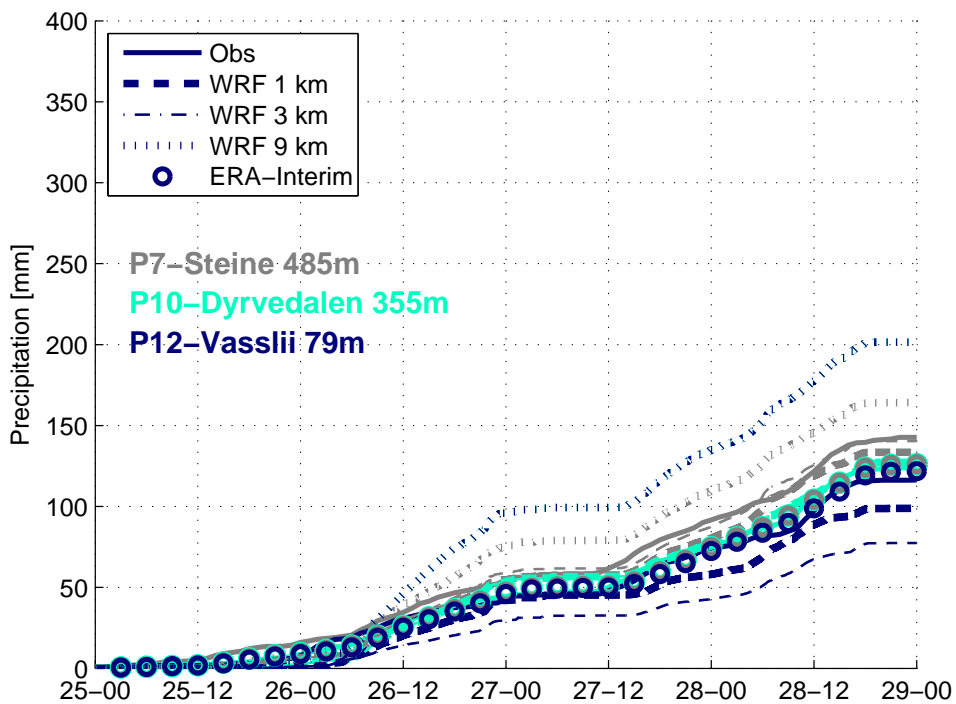[2]Horizontal × 2, vertical and temporal resolution increase.
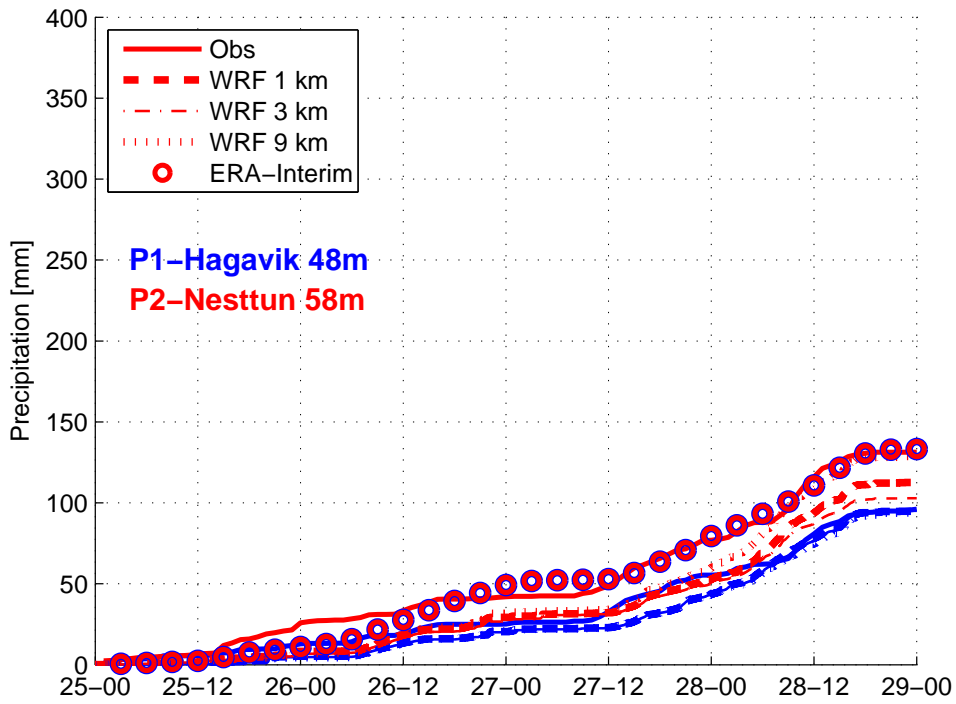
(a) Comparison of grid resolution for the two coastal stations.
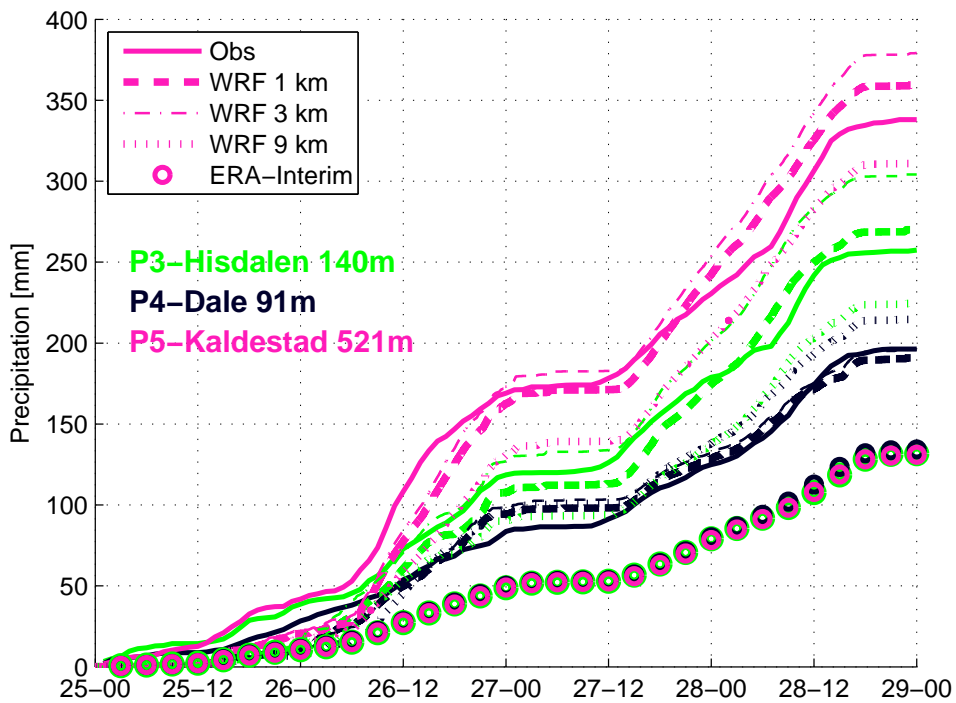
(b) Comparison of grid resolution at the three steep terrain stations.
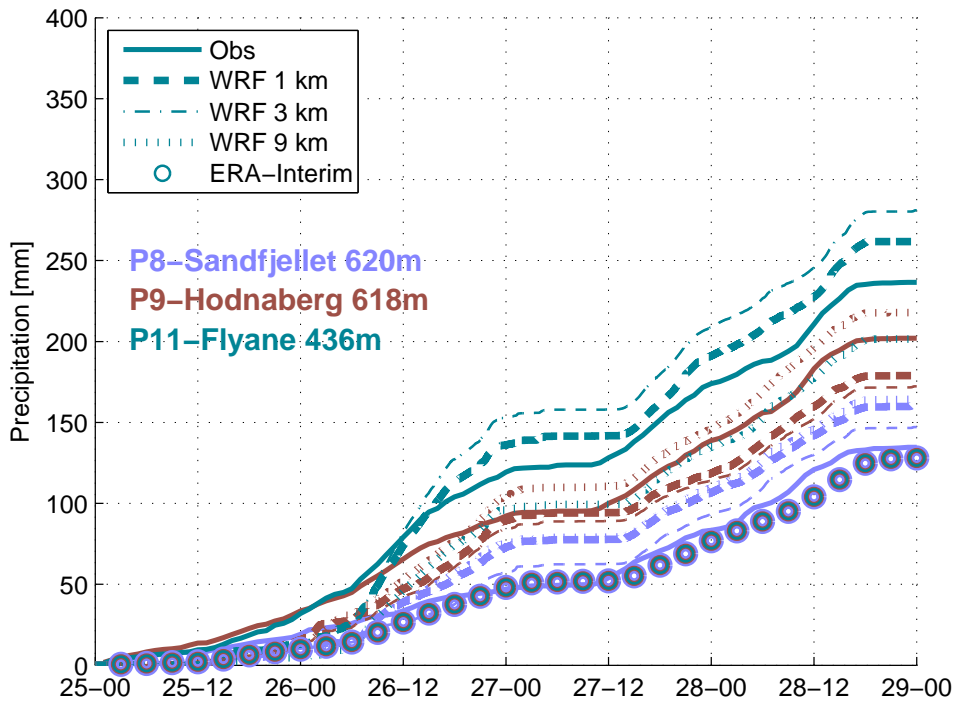
(c) Comparison of grid resolution at the three mountain stations.

(d) Comparison of grid resolution for the three stations north in the valley.

Figure 6.9: Comparison of grid resolution and the effect on point precipitation.

6.4 Waves and spill over effects

In the previous sections of this chapter a model sensitivity study has been presented to optimize the WRF setup for the campaign area. The 3D fields of the relevant parameters (i.e. humidity, temperature, horizontal and vertical wind) from the corresponding simulation will now be used for a detailed investigation of processes important for precipitation modification in the complex terrain of the study area. A cross section through the area from SW to NE has been chosen along the stations P1, P3, P5 and P7 (See Figure 6.10). The center point is at the station P5, and the direction corresponds with the dominant inflow direction of 220° during the case study period. The contour colors show the grid altitude in domain 3, and the operational HOBO rain gauges are marked with their respective colors. As previously the depicted model run is the run with a relaxation time of 1 hour because of its overall best performance as presented in Section 6.5.

An example of a vertical cross section for potential temperature and vertical velocity is shown in Figure 6.11. Well defined gravity waves are visible after the flow passes the coast line of Norway. The wavelengths at E 6.5 are approximately 12 km, even shorter wavelengths are present over the Hamlagrø plateau at E 6.2. This indicates the importance of small scales when studying orographic precipitation in complex terrain.
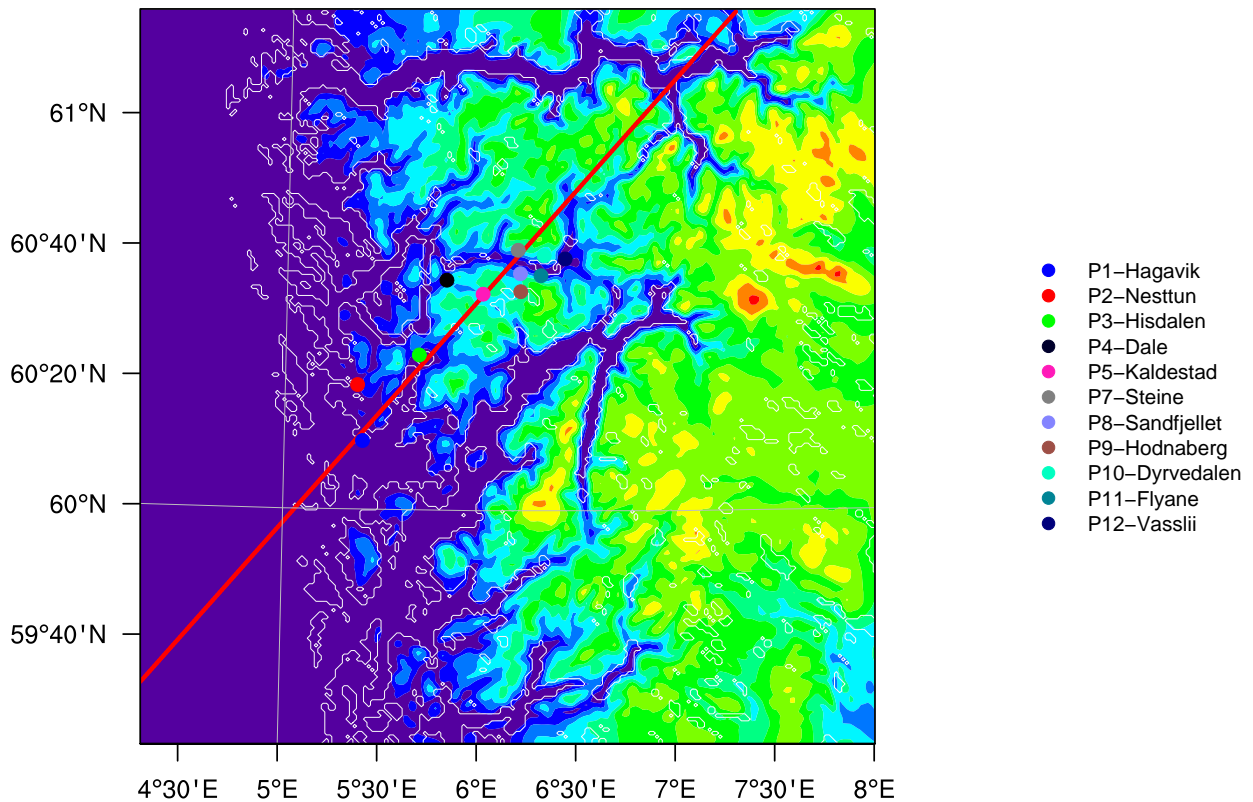

Figure 6.10: The cross section (SW to NE) used in the following, indicated by a red line. Altitude from the WRF domain 3 in colors, the operational station positions are marked.
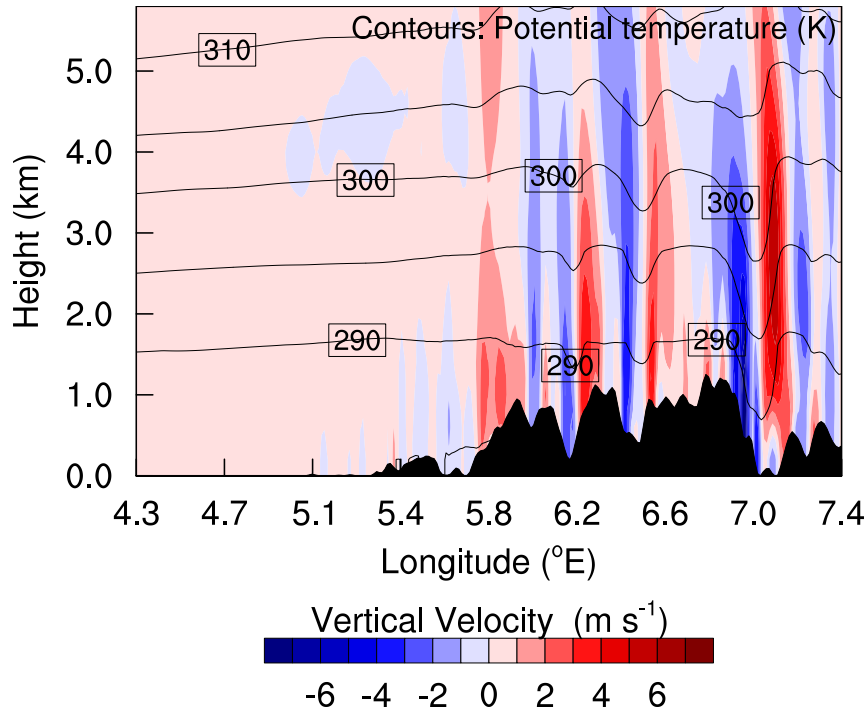
Figure 6.11: Vertical cross section of the vertical wind component in colors, and the potential temperature with contours, at 26th of October at 18 UTC.

For the following discussion, three model times have been selected for comparison. One during the first heavy precipitating period at 18 UTC October 26, the second in the dry period at 06 UTC October 27, and finally during the second heavy precipitation period at 06 UTC on October 28. A series of cross sections of the vertical velocity are presented in Figure 6.12. The air mass is slowly rising as it approaches the coast line. When the flow impinges topography higher than a few hundred meters, gravity waves form. The gravity waves are present at all time steps, though with less intensity at the last time step. There is no significant tilt in the wave crests with altitude. The potential temperature shows a clear terrain induced displacement, reducing only slightly with altitude. The atmosphere is stable, weakest stability is found at the first time step, though with the strongest wave activity. Strongest stability is seen during the dry period with accordingly strong wave activity, and an intermediate stability value is found for the second precipitation period.

The cross sections of the specific humidity at the three selected time steps are presented in Figure 6.13. The specific humidity is varying trough the period, with a minimum at the dry period and a maximum at the last time step selected. Vertical displacements of dryer air are visible downstream of the large mountains at all time steps. The major displacements caused by large mountains are detectable throughout the lower 5 km, whereas smaller hills only causes displacement in the lower few hundreds of meters of the atmosphere.

Figure 6.12 and Figure 6.13 together reveal some interesting features. The strong gravity wave activity in the first time step, together with moderate humidity corresponds with the large observed

precipitation variability amongst stations. The second time step, with slightly less wave activity, but considerably dryer air and the most stable atmosphere, corresponds with the non precipitating period. And finally, the third time step with weaker gravity waves, but very high humidity, results in a higher amount of observed precipitation, but with a smaller area inhomogeneity. It indicates the significant influence of the gravity waves, hence orographic modification, on the lateral precipitation distribution.

(a) 26/10 18 UTC   (b) 27/10 06 UTC   (c) 28/10 06 UTC
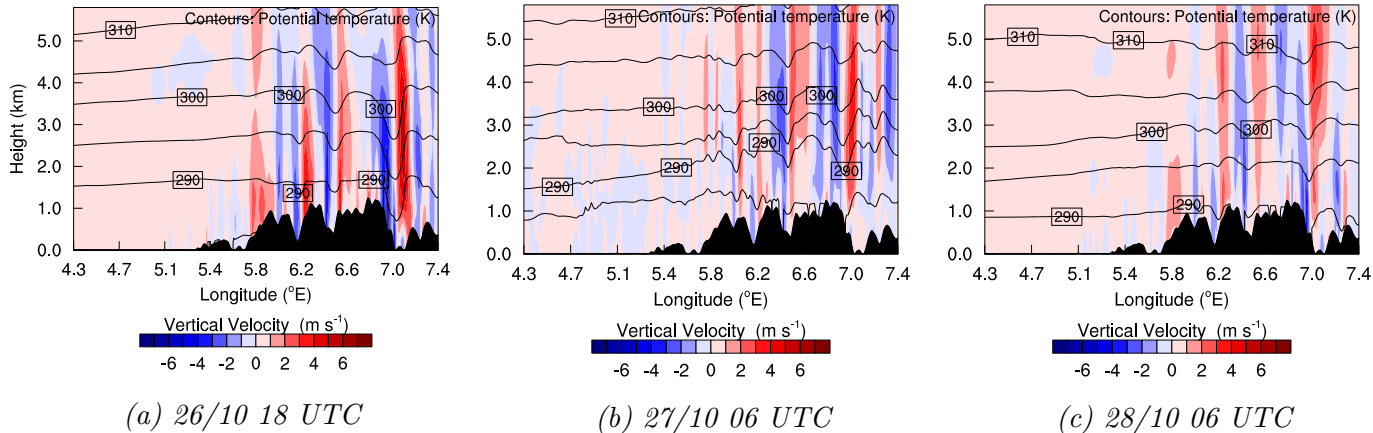
Figure 6.12: Cross section of vertical velocities at 3 selected times. 26th at 18 UTC, 27th at 06 UTC and 28th at 06 UTC. Colors are vertical velocity, contours are potential temperature.

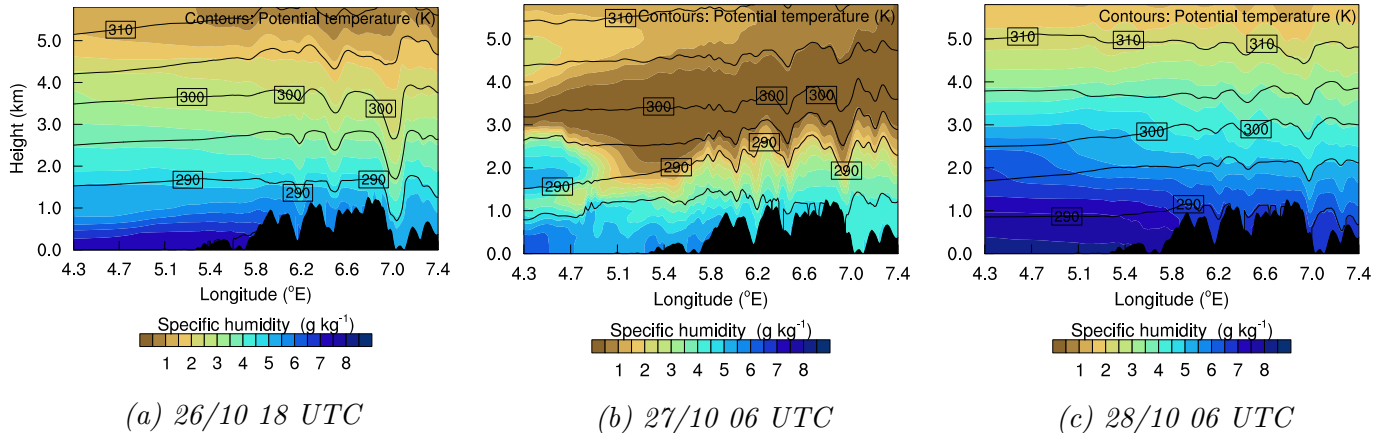(a) 26/10 18 UTC   (b) 27/10 06 UTC   (c) 28/10 06 UTC

Figure 6.13: Cross section of specific humidity at 3 selected times. 26th at 18 UTC, 27th at 06 UTC and 28th at 06 UTC. Colors are specific humidity, contours are potential temperature.

The liquid water content (LWC) and a summation of the ice water content (IWC) and LWC are shown in Figure 6.14 and Figure 6.15. In the first time step at E 5.9 the LWC clearly increases uphill and maximizes over the barrier crest. The spill over effect is visible as the continued high LWC level downslope. The large areal inhomogeneity in the observed precipitation may be related to the distinct differences in LWC. The same features are detectable on the following barriers, but not as intense. The final time step shows similar results for the first major barrier at E 5.9, but the LWC signals smooth over the remaining terrain features, distributing the precipitation more evenly. A reason for

this change may be found in Figure 6.15 where it is shown that the first period of precipitation is nearly unaffected by ice particles, whereas in the final period the atmosphere contains large amounts of those. The large continuous area of ice particles may act as a seeder for the lower layer cloud. The consequence of the homogeneous seeding is a faster growth of droplets, with a corresponding larger precipitation amount and less horizontal variability.

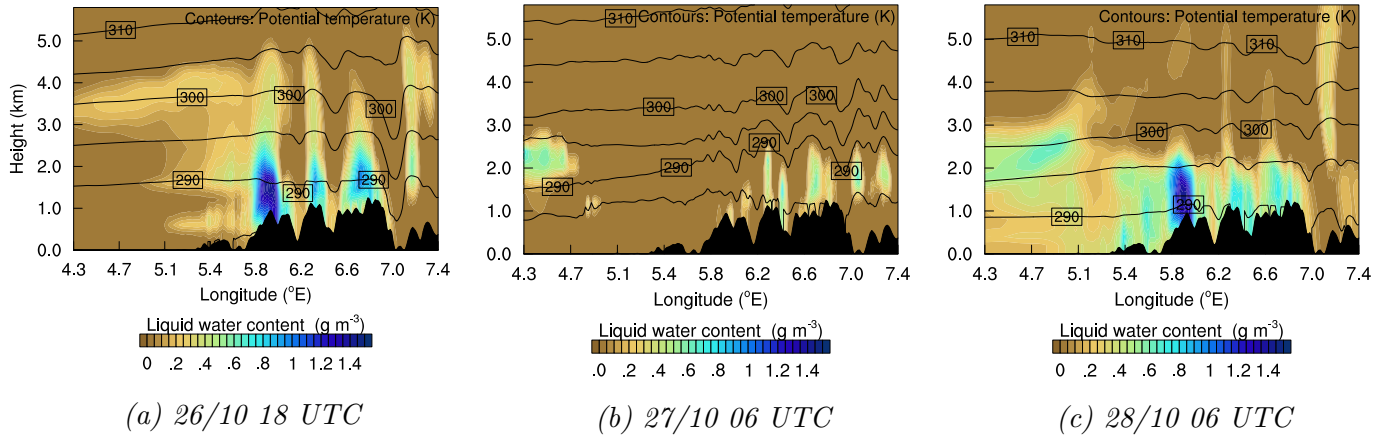*(a) 26/10 18 UTC* *(b) 27/10 06 UTC* *(c) 28/10 06 UTC*

Figure 6.14: Cross section of liquid water content (LWC) at 3 selected times. 26th at 18 UTC, 27th at 06 UTC and 28th at 06 UTC. Colors are LWC, contours are potential temperature.

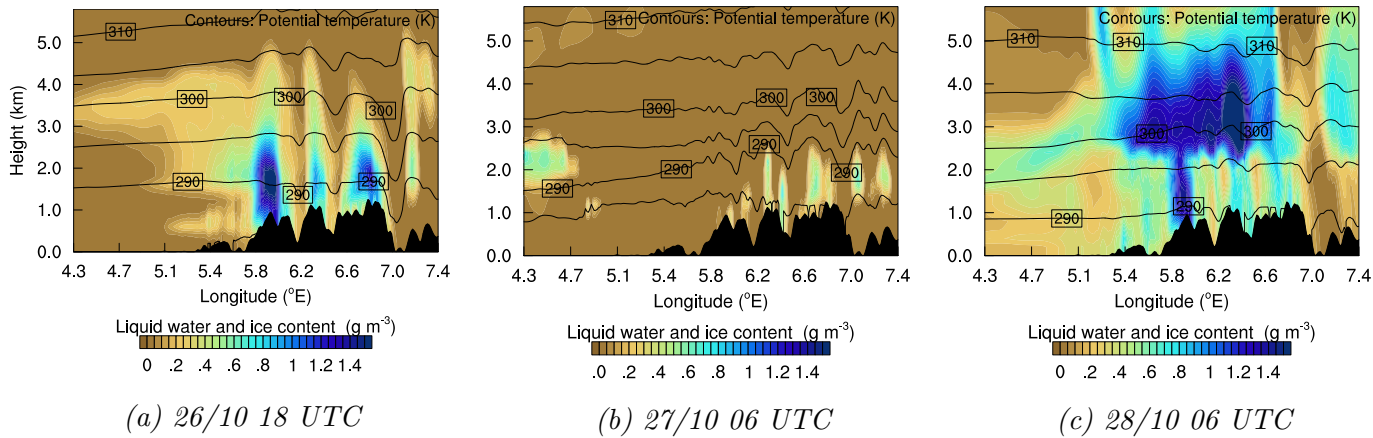*(a) 26/10 18 UTC* *(b) 27/10 06 UTC* *(c) 28/10 06 UTC*

Figure 6.15: Cross section of liquid water content (LWC) and ice water content (IWC) at 3 selected times. 26th at 18 UTC, 27th at 06 UTC and 28th at 06 UTC. Colors are LWC+IWC, contours are potential temperature.

Figure 6.16 presents the horizontal wind velocity at the selected times. Generally the precipitating periods have higher wind speeds, than the non precipitating period. The figure reveals deceleration of the horizontal wind upwind of topography and enhanced acceleration on the lee side of the terrain. A low level lee jet is detectable during precipitating events, especially at the first time step. Both deceleration and the acceleration jet are visible in altitudes up to 2-3 km. The vertical shear is increasing at the 27th, and remains high during the second precipitating event, this could have created

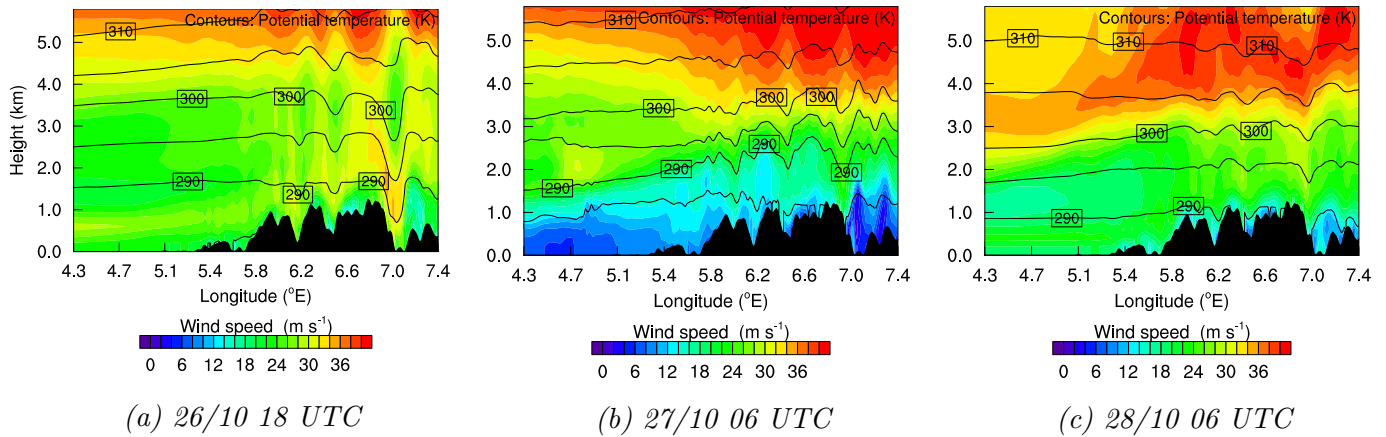*(a) 26/10 18 UTC*   *(b) 27/10 06 UTC*   *(c) 28/10 06 UTC*

Figure 6.16: Cross section of horizontal wind speed, 3 selected times. 26th at 18 UTC, 27th at 06 UTC and 28th at 06 UTC. Colors are wind speed, contours are potential temperature.

smaller areas of enhanced precipitation due to turbulent overturning in the shear layer (See Section 2.2.1). This effect is not detectable in Figure 6.13c, possibly because of the strongest shear is in 3 to 4 km altitude where the specific humidity has decreased significantly.

The horizontal distribution of the accumulated model precipitation during the four day case study period is presented in Figure 6.17. The campaign stations are marked on the map with their respective colors. Over the North Sea the precipitation distribution is homogeneous, and the amounts are relatively low. The synoptic scaled forced ascent increases precipitation amounts closer to the coast line. Further inland the precipitation amounts becomes inhomogeneous, confined areas of accumulated precipitation up to 600 mm can be depicted south of the campaign area. The station at Kaldestad (P5) is located at the edge of an area with large amounts of precipitation, situated overhead the first major terrain barrier of approximately 1000 m in the flow direction. Within 5 km the precipitation varies with as much as 300 mm during the four days of case study. The horizontal scale of 5 km corresponds to the scale of the gravity waves depicted in Figure 6.12.

The valley NE of P12 has markedly less precipitation than the steep and elevated terrain around. The area is approximately 100 km from the coast in the flow direction, situated in the synoptic scaled evaporation zone behind the elevated Hamlagrø plateau. The reduced precipitation is likely to be a result of this location and the enhancement around is caused by smaller scale orographic features. Outside the campaign area a large area of enhanced precipitation at N 60° and E 6.5° is of interest. The area is part of the inflow to the river Opo which removed the ground under five houses in Odda during the flooding event.

6.5   Model case summary and conclusions

Previously RMSE and ME have been presented for each station. Table 6.6 presents one overall value for each model run. They are calculated by the use of all co-existent time steps within the observational
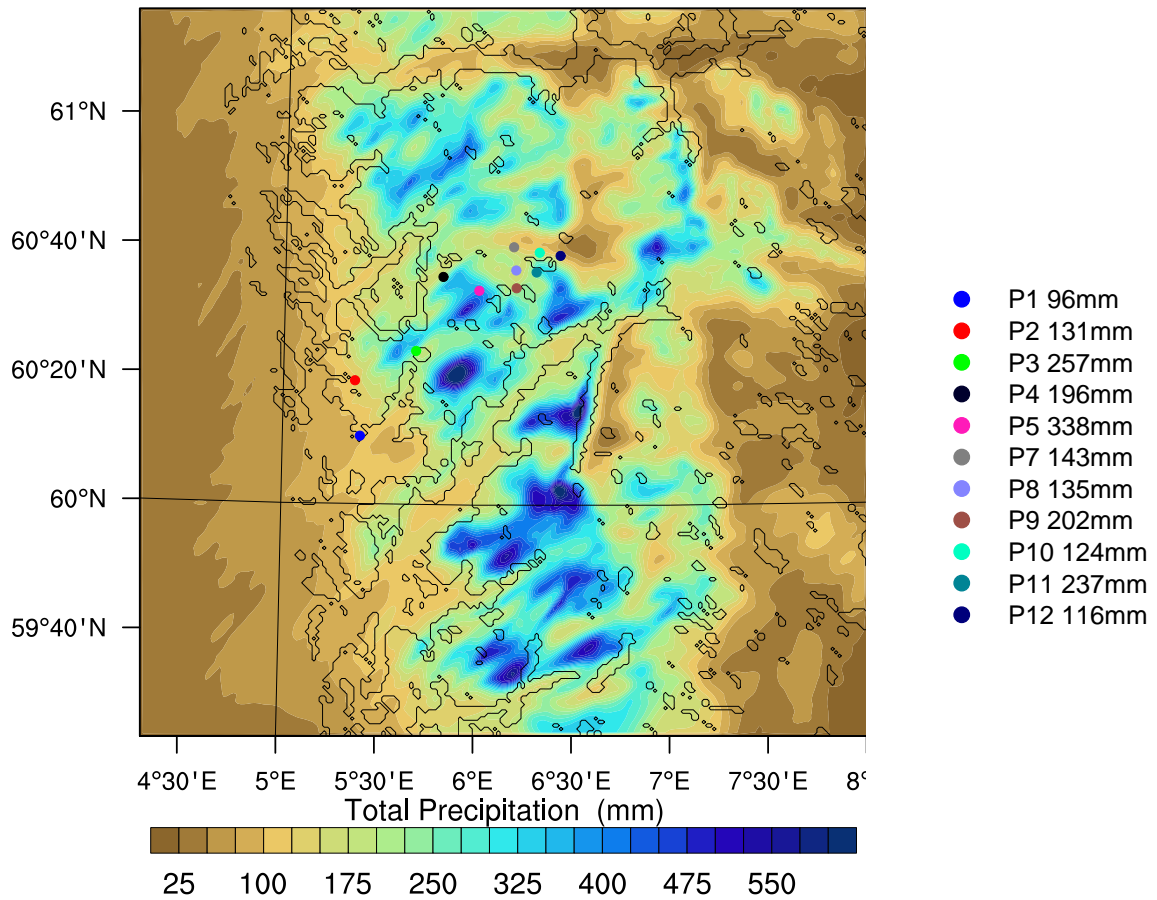
Figure 6.17: Accumulated precipitation in the innermost domain. Campaign stations are marked with their identification color and the observed accumulated precipitation amount in the legend.

values, which has a temporal resolution of 1 hour, and the compared dataset.

An overall lowest RMSE is found in the 1 km grid size with a relaxation time of 1 hour, and nudging applied on wavelengths longer than 677 km zonal and 609 km meridional respectively. For the 3 km grid size domain the lowest RMSE and MAE is found at the run with the more smoothed terrain. For the less smoothed option the lowest RMSE and MAE for the 3 km grid size is found when no artificial nudging terms are applied. All but one run has negative ME, that is the model is underestimating the precipitation observed. All negative ME are increasing when the grid size is reducing. This is somehow unexpected, but probably due to the cancellation of positive and negative errors in the larger domains. For the single run with positive ME, the error is reducing with increased horizontal resolution.

Overall the model result are representing the observations well. The first 12 to 36 hours are generally underestimated, but towards the end of the integration time, the total precipitation on each station is well captured. The timing of the precipitating events are good. All model runs have problems with

representing P8 and P9 correctly. P8 is continuously overestimated whereas P9 is underestimated in all runs. The modeled precipitation on these station sites is similar, but differ from the observations. The topography at the station sites is complex, and the stations may gain on a further increase in horizontal resolution. Why the model has issues with these stations in particular, compared to other mountainous stations in terrain of same complexity, is not clear.

The sensitivity studies on spectral nudging indicate that an appropriate choice of nudging can improve the model performance. Importantly there is no indication of reduced ability to represent extreme events. This is in agreement with the study of Glisan et al. (2013), but disagree with the study of Alexandru et al. (2009). Overall spectral nudging reduces the RMSE and the MAE in the 1 km grid domain. The studies show some sensitivity to relaxation time and cut off wavelengths. The overall lowest RMSE during this case study was the model run with WRF standard settings of relaxation time (1 hour), and nudging of wavelengths longer than 677 km zonally and 609 km meridionally. This is a larger nudging coefficient than Omrani et al. (2012a) found optimal for their studies.

Coastal station precipitation is mainly synoptic scale driven and well represented in the initial- and boundary conditions. Nudging towards the driving field for a large spectra of wavelengths improves the representation for those. The inland stations, with orographic effects on a smaller scale, showed larger variation and gain credibility when nudging, but for longer wavelengths only. The shorter wavelengths contributes to the fine scale precipitation and should be allowed to develop within the model itself. P12 was surprisingly well resolved in the ERA-Interim reanalysis. Due to its position it is believed to be affected strongly by orographic effects which was not expected to be resolved in the large scale ERA-Interim dataset. The precipitation amount is comparable with the coastal stations, but the important scale is believed to be much smaller. The station may be well represented because of its comparable precipitation amounts, but this could be just a coincidence.

The sensitivity to grid size is larger. The deviations from the observations found in the 9 km grid resolution runs and the ERA-Interim dataset confirm the importance for downscaling. However, for longer climate runs the computational savings by reducing grid resolution favorize the 3 km grid size, whereas for shorter runs the improvement received by the 1 km resolution is preferable.

The closer investigation of the best performing model run, judged on RMSE, indicates the importance of small scale features. The topography influence on a few kilometers scale is detectable in all analyzed variables and length scales in the order of 5-10 km seem crucial for local precipitation accuracy. Both gravity waves, forced upslope ascent and spill over effects have influence on these scales. The result indicates that strong gravity waves in conjunction with a low or non-existent seeder effect, enhances the inhomogeneity in precipitation distribution.

Table 6.6: *Statistical errors for the model runs, lowest errors [%] are marked in bold*

Topography smoothing	Nudging [s⁻¹]	Nudged wavelengths	Grid size	RMSE [%]	MAE [%]	ME [%]
1-2-1	$3.0{\times}10^{-4}$ s⁻¹	> 677km Z, 609km M	1km	7.41	**5.96**	-3.19
1-2-1	$3.0{\times}10^{-4}$ s⁻¹	> 677km Z, 609km M	3km	8.82	7.12	-2.48
1-2-1	$3.0{\times}10^{-4}$ s⁻¹	> 677km Z, 609km M	9km	14.45	10.97	-0.64
sds	$3.0{\times}10^{-4}$ s⁻¹	> 903km Z, 812km M	1km	7.84	6.11	-3.23
sds	$3.0{\times}10^{-4}$ s⁻¹	> 903km Z, 812km M	3km	10.32	7.86	-2.39
sds	$3.0{\times}10^{-4}$ s⁻¹	> 903km Z, 812km M	9km	14.89	11.39	-1.07
sds	$3.0{\times}10^{-4}$ s⁻¹	> 677km Z, 609km M	1km	**7.37**	6.07	-2.26
sds	$3.0{\times}10^{-4}$ s⁻¹	> 677km Z, 609km M	3km	9.85	7.57	-1.45
sds	$3.0{\times}10^{-4}$ s⁻¹	> 677km Z, 609km M	9km	15.49	11.80	**+0.00**
sds	$3.0{\times}10^{-4}$ s⁻¹	> 338km Z, 304km M	1km	9.62	7.39	+1.76
sds	$3.0{\times}10^{-4}$ s⁻¹	> 338km Z, 304km M	3km	12.56	9.52	+2.39
sds	$3.0{\times}10^{-4}$ s⁻¹	> 338km Z, 304km M	9km	16.55	11.90	+3.76
sds	$4.62{\times}10^{-5}$ s⁻¹	> 677km Z, 609km M	1km	8.63	7.01	-4.95
sds	$4.62{\times}10^{-5}$ s⁻¹	> 677km Z, 609km M	3km	9.99	7.76	-4.33
sds	$4.62{\times}10^{-5}$ s⁻¹	> 677km Z, 609km M	9km	14.38	10.96	-2.57
sds	$1.16{\times}10^{-5}$ s⁻¹	> 677km Z, 609km M	1km	9.44	7.68	-5.72
sds	$1.16{\times}10^{-5}$ s⁻¹	> 677km Z, 609km M	3km	10.20	8.05	-4.92
sds	$1.16{\times}10^{-5}$ s⁻¹	> 677km Z, 609km M	9km	14.51	11.00	-4.11
sds	No nudging	N/A	1km	9.46	7.50	-5.23
sds	No nudging	N/A	3km	8.85	7.07	-4.71
sds	No nudging	N/A	9km	15.45	11.81	-3.66
N/A	ERA-Interim	N/A	0.75°	29.89	18.04	-15.92

Chapter 7

Summary and outlook

The main aim of this thesis was to increase the insight into the fine scale distribution of precipitation in complex terrain. A well known hypothesis is that orographic effects have a large influence on the local precipitation distribution and it should be possible to measure variability within smaller horizontal scales. Therefore two observational campaigns have been conducted as part of this thesis, and together they form a valuable dataset for small scale precipitation tests and validation in complex terrain. The dataset includes, by chance, a major flooding event, and in that context it is unique with its high horizontal resolution.

The campaign dataset has shown a general high spatial variability of precipitation. During low wind situations however, the precipitation pattern was rather homogeneous and showed low variability between observed precipitation at inland stations. The coastal stations were affected by heavy convective situations, in particular during the summer months, resulting in a slightly higher variability. The high wind situations, appearing less frequently, were responsible for more than 60 % of the precipitation inland and the spatial inhomogeneity was significant. Horizontal distances between observation stations confirms the importance of scales down to 5 km. A wind direction dependency has also been found for some stations during high wind events. These variations are related to special topography features within 20 km of the station.

A case study of an extreme precipitation event has been performed by the use of the numerical model WRF. The event caused 200 year flooding several places on the west coast of Norway, and the economical consequences where large. The model has been validated against the observational dataset, and an optimal spectral nudging setting has been found for this case study. The model study confirms the importance of meteorological scales of 5 km or less, which corresponds well with the observational campaigns. The model reproduces gravity waves, the forced ascent and the spill over effect remarkably well and the point precipitation is well represented for most stations. Two mountainous stations have larger errors than the remaining stations, the reason is unknown.

By this it is clear that a combination of observational campaigns and model runs is a favorable method to increase our knowledge of orographic modification of precipitation. To decrease the computational demands in longer runs a 3 km grid resolution may be sufficient for climatological means, but for

shorter runs and a goal of increasing theoretical knowledge a further downscaling beyond 1 km should be considered in complex terrain. This could possibly have increased the representation of the two mountainous stations with reduced performance.

The added value from model simulations is beneficial, it enables 4D visualization of selected events. Interesting work in the future would include case studies of selected events to identify and investigate orographic modifications further.

For future observational campaigns a suggestion would be to have a denser observational network in a limited area. This setup would exclude the synoptic variability and thereby concentrate on the smaller scales. An interesting campaign setup would be a transect over a smaller hill in this complex terrain. The transect could follow the prevailing wind directions 210° to 240° and have a horizontal spacing as low as 1 km to catch fine scale variations. In addition to continuous precipitation and wind measurements, shorter campaigns with increased data collection e.g. stability and moisture measurements throughout the lower moist level of the atmosphere, would add value to a dataset. Longer or several campaign periods should be considered. With a larger dataset one could have attempted to categorize the events further and possibly found clearer signals. Longer campaign periods would also increase the statistical robustness.

Appendix A

Terrain profiles 200°-250° by station
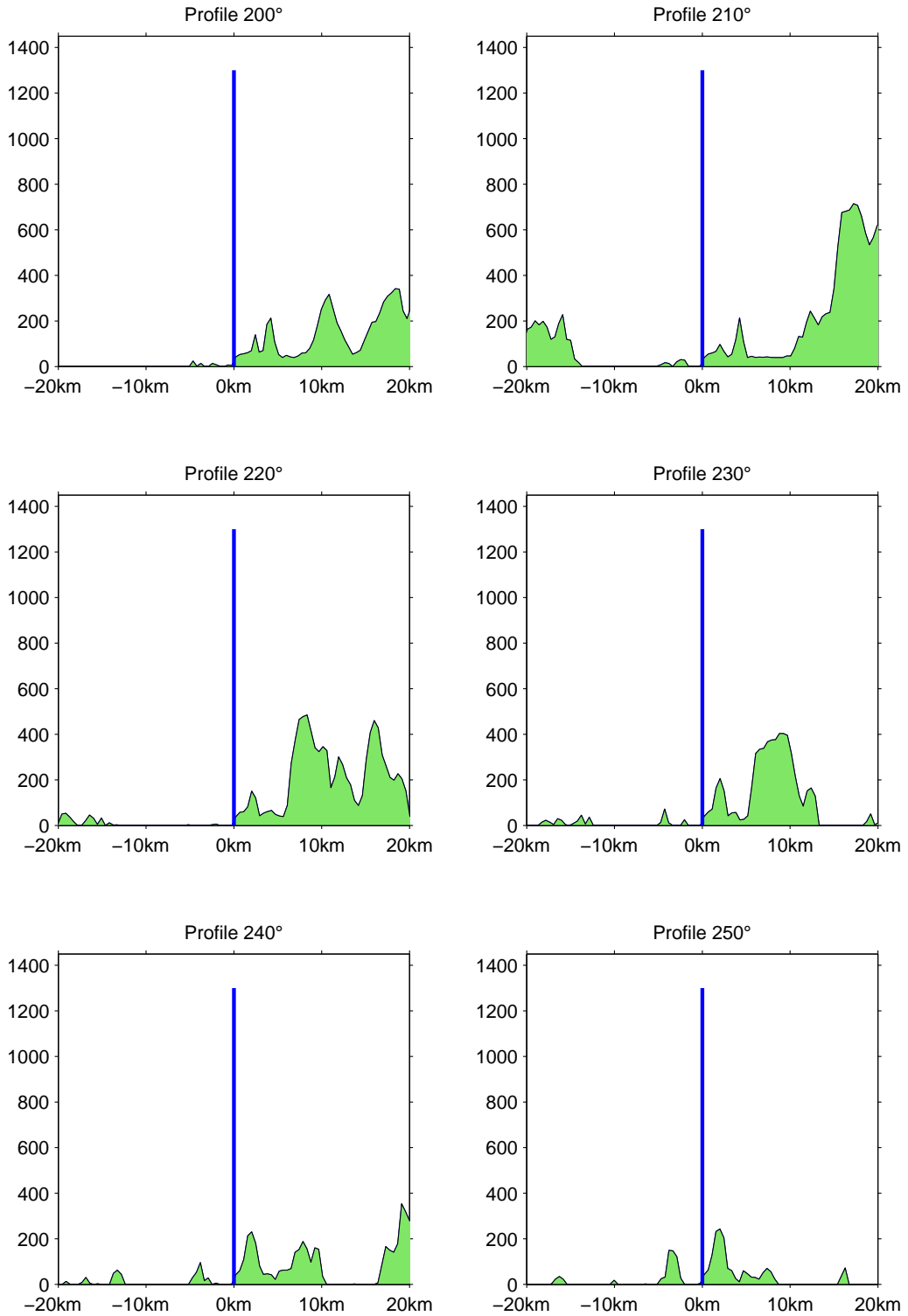
P1–Hagavik 48m

Figure A.1: Terrain profile 20 km upstream and downstream of the station.
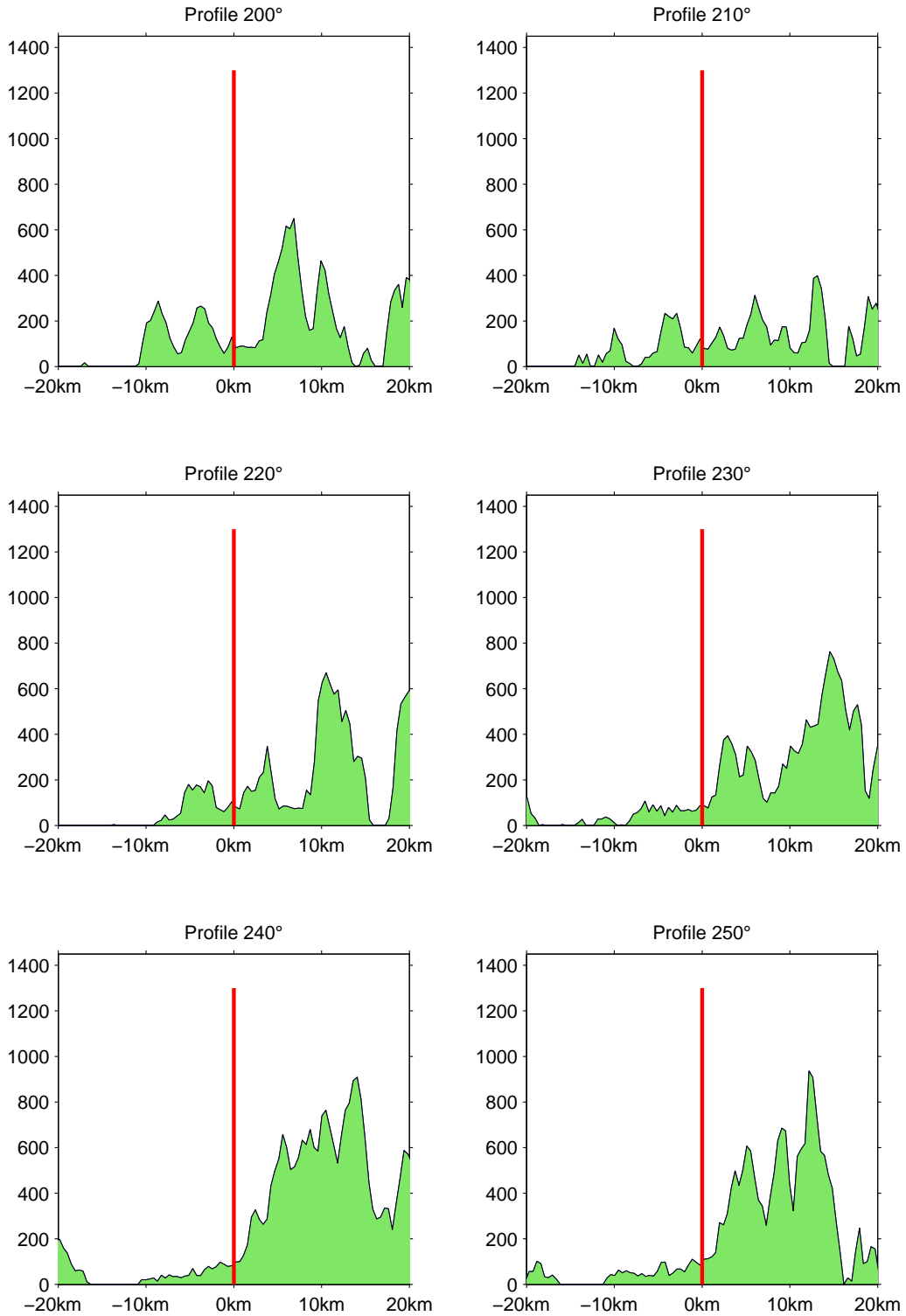
P2–Nesttun 58m

Figure A.2: Terrain profile 20 km upstream and downstream of the station.

P3–Hisdalen 140m

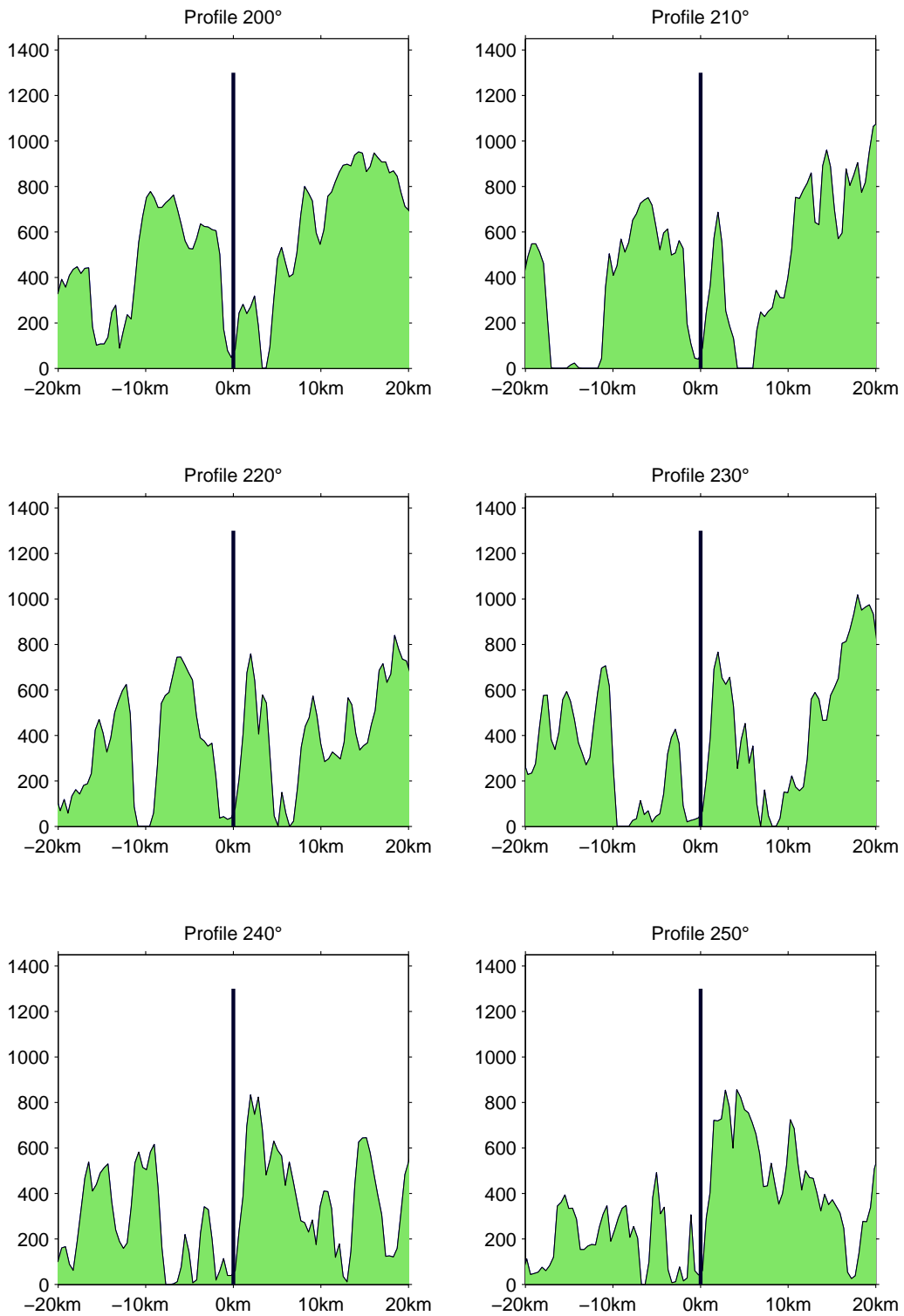Figure A.3: Terrain profile 20 km upstream and downstream of the station.

84

P4–Dale 91m

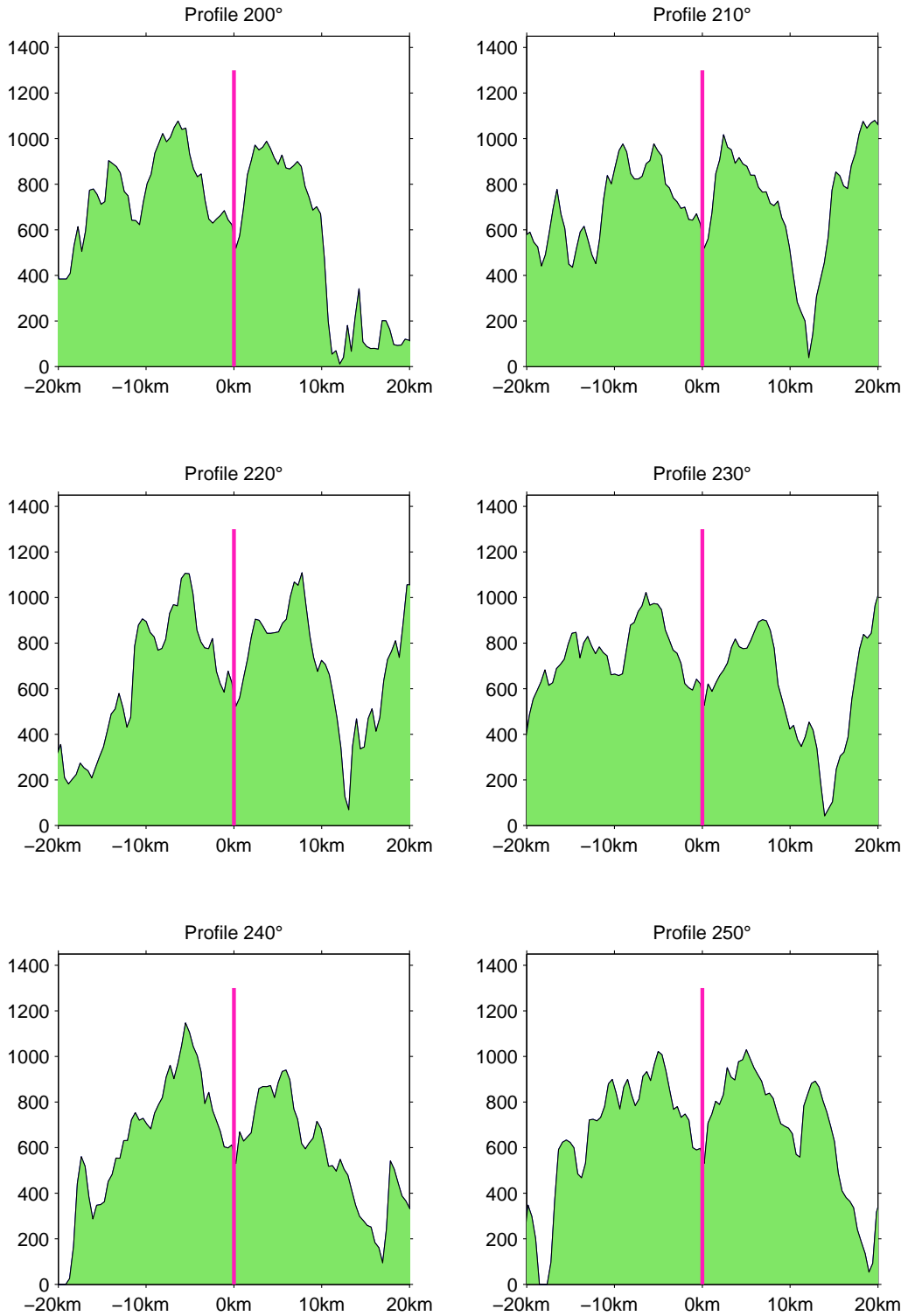*Figure A.4: Terrain profile 20 km upstream and downstream of the station.*

P5–Kaldestad 521m

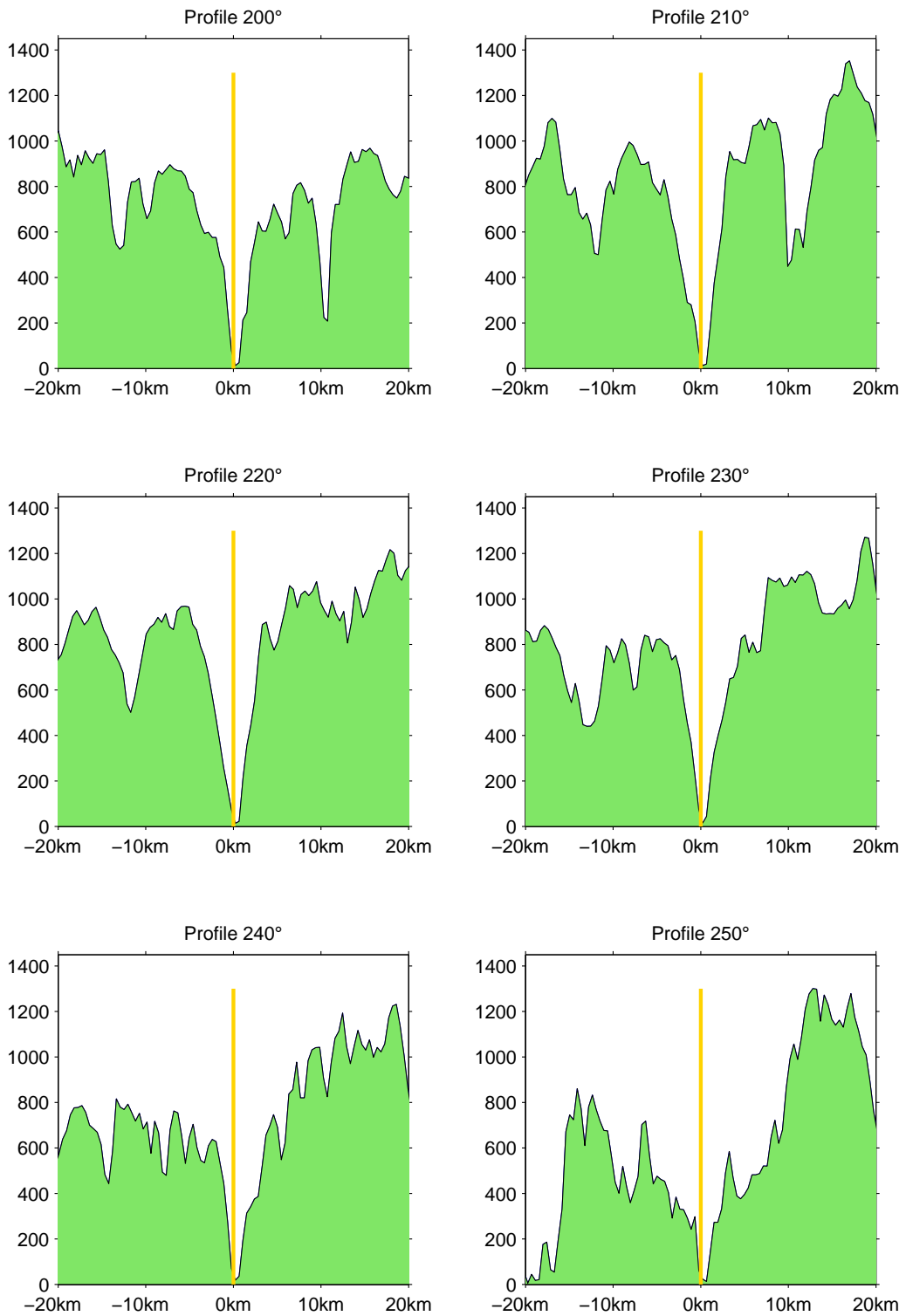Figure A.5: Terrain profile 20 km upstream and downstream of the station.

P6–Evanger 27m

Figure A.6: Terrain profile 20 km upstream and downstream of the station.
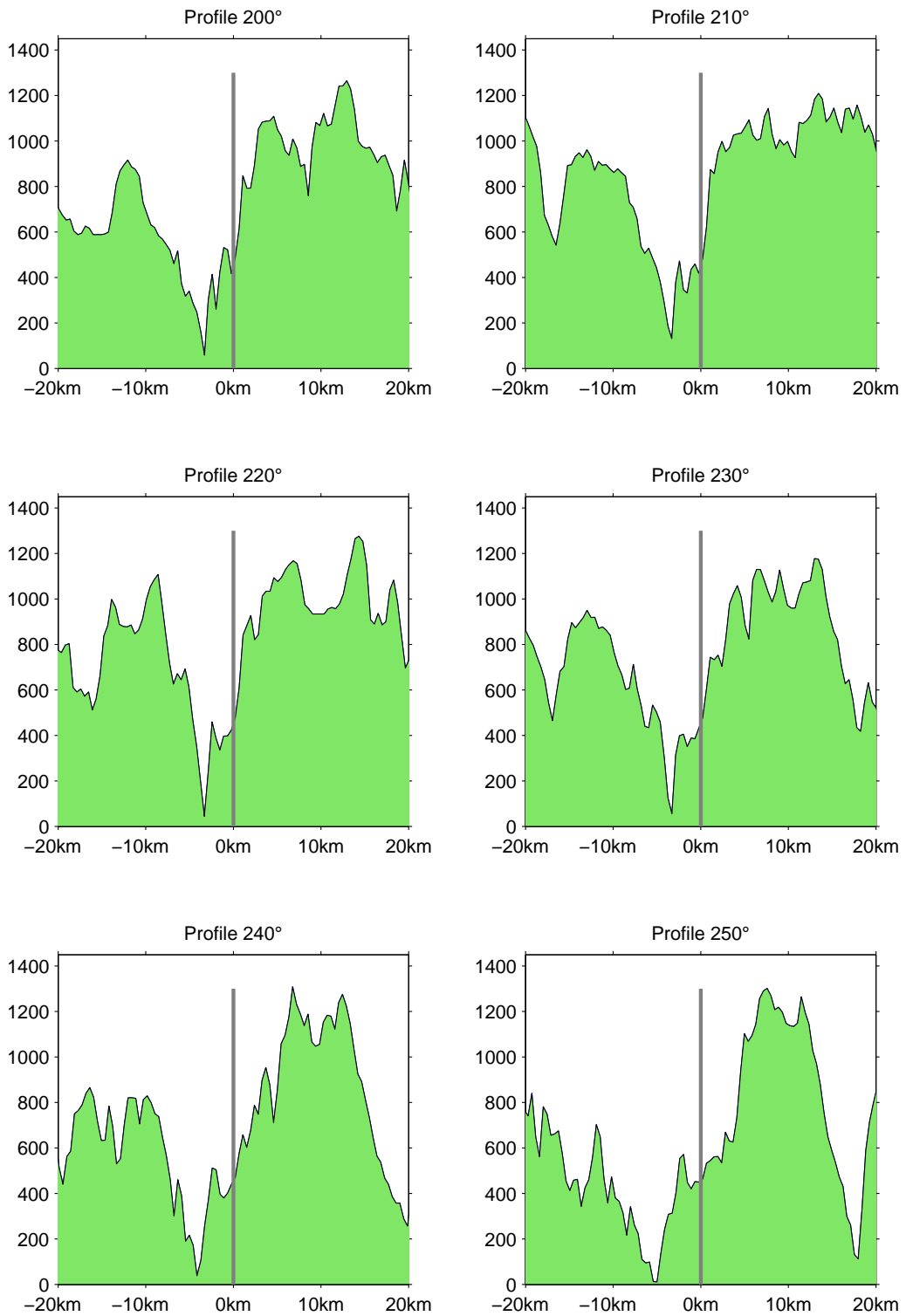
P7–Steine 485m

Figure A.7: Terrain profile 20 km upstream and downstream of the station.

P8–Sandfjellet 620m

Figure A.8: Terrain profile 20 km upstream and downstream of the station.
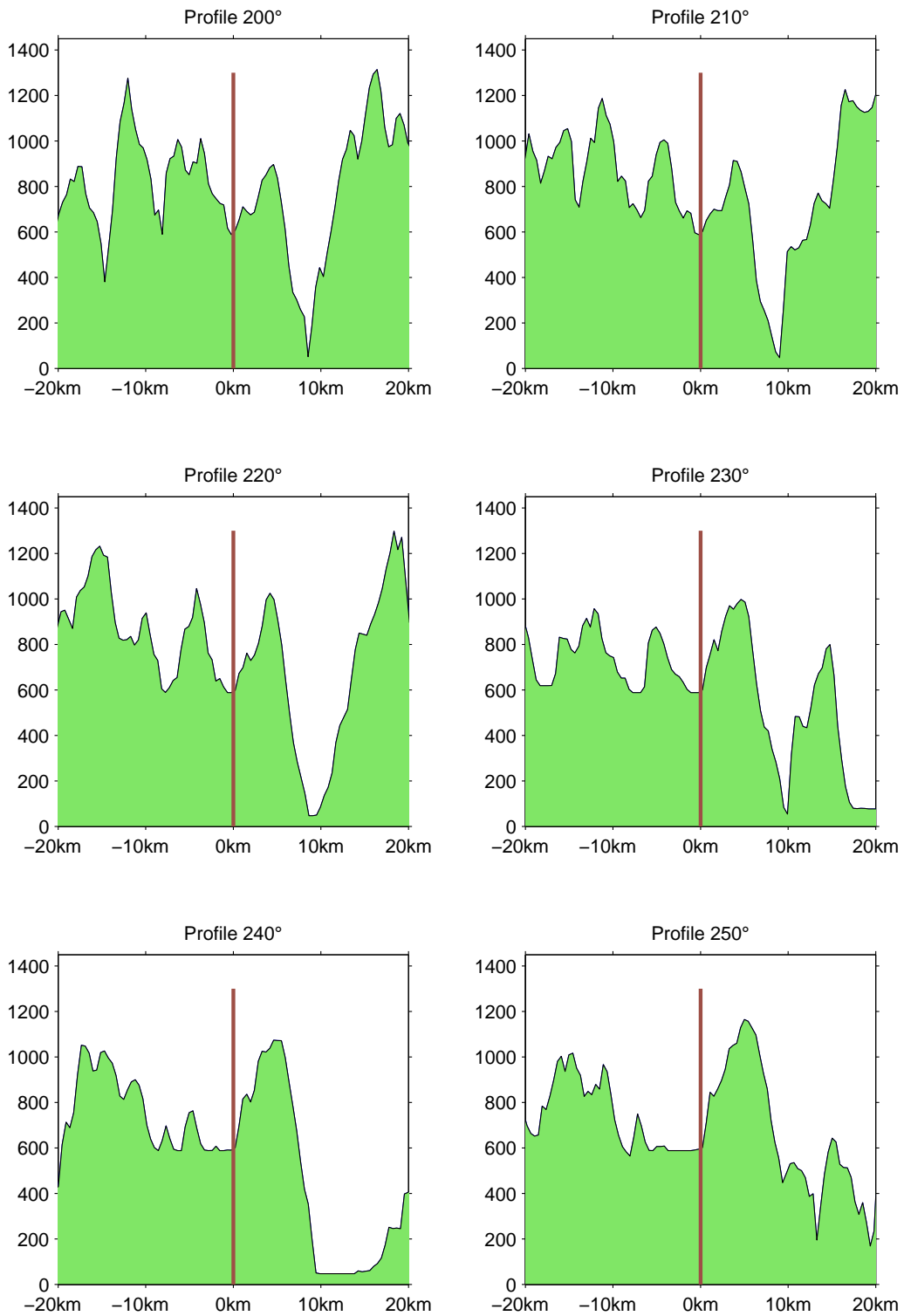
P9–Hodnaberg 618m

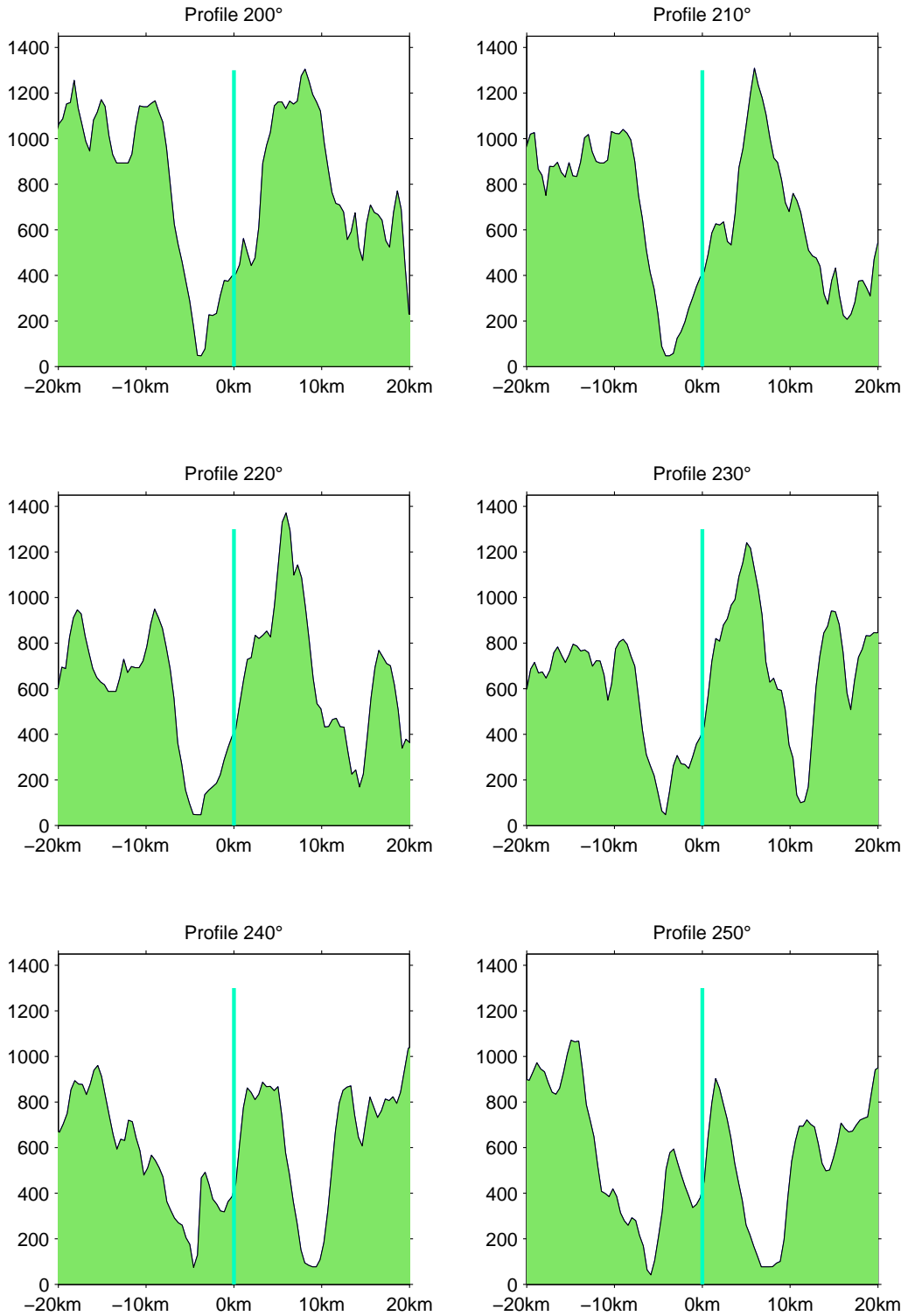Figure A.9: Terrain profile 20 km upstream and downstream of the station.

P10–Dyrvedalen 355m

Figure A.10: Terrain profile 20 km upstream and downstream of the station.

P11–Flyane 436m

Profile 200°

Profile 210°

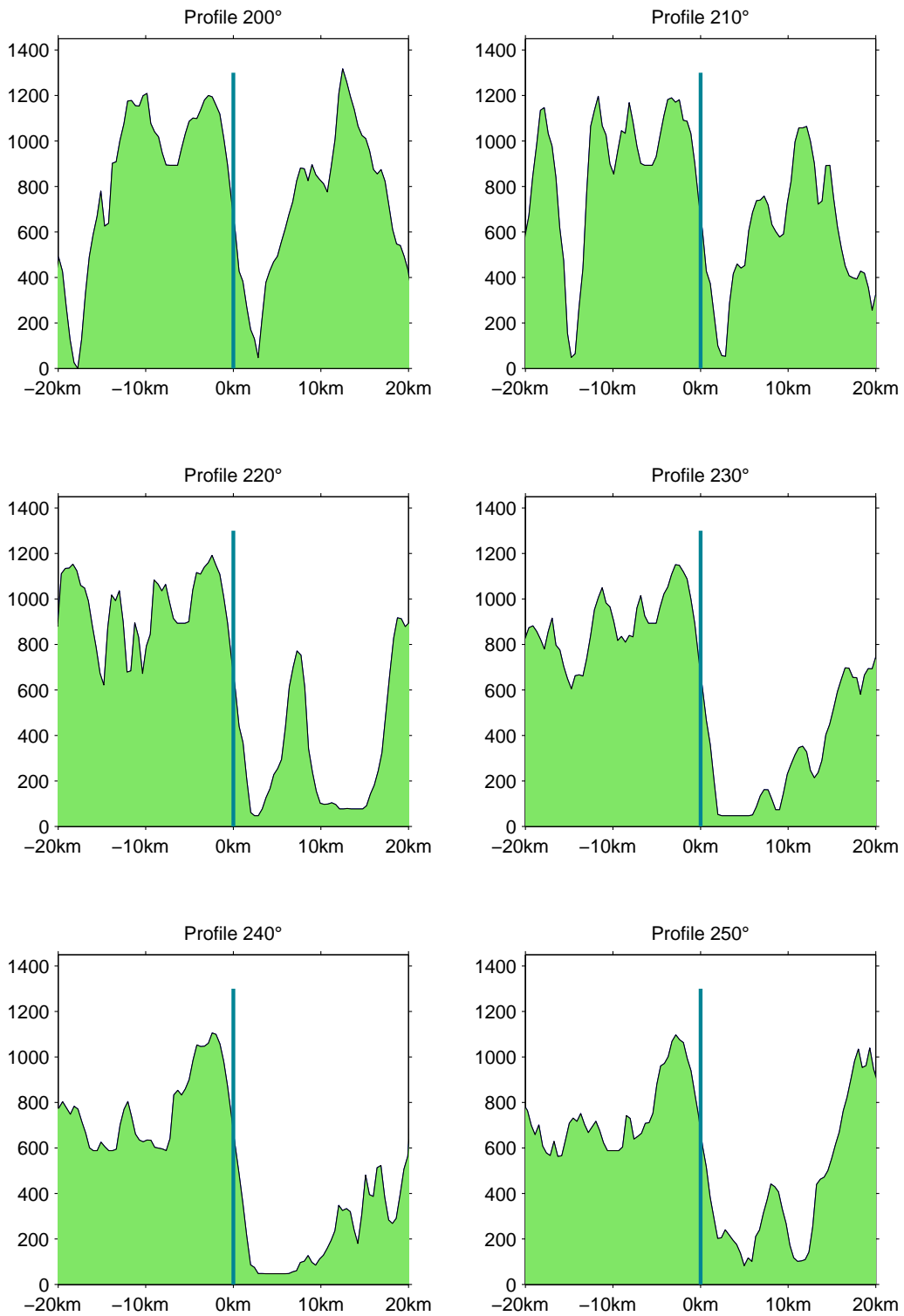Profile 220°

Profile 230°

Profile 240°

Profile 250°

Figure A.11: Terrain profile 20 km upstream and downstream of the station.
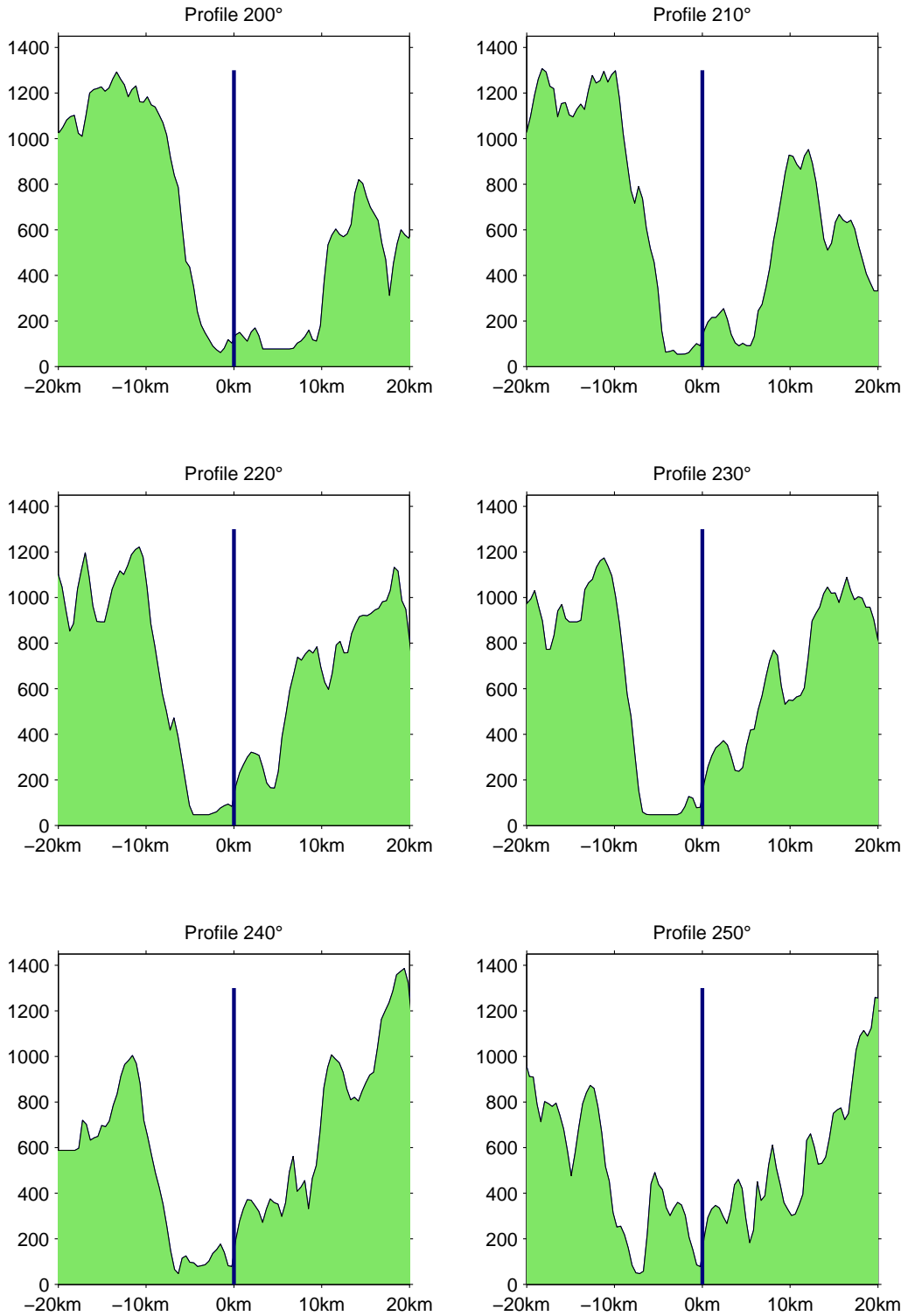
P12–Vasslii 79m

Figure A.12: Terrain profile 20 km upstream and downstream of the station.

Appendix B

Terrain profiles by direction

Profile direction 200° – 20°

Figure B.1: Terrain profiles for stations P1-P6, direction is 200°.

95

Profile direction 200° – 20°

Figure B.1: Terrain profiles for stations P7-P12, direction is 200°.

96

Profile direction 210° – 30°

P1–Hagavik 48m

P2–Nesttun 58m

P3–Hisdalen 140m

P4–Dale 91m

P5–Kaldestad 521m

P6–Evanger 27m

Figure B.2: Terrain profiles for stations P1-P6, direction is 210°.

97

Profile direction 210° – 30°

Figure B.2: Terrain profiles for stations P7-P12, direction is 210°.

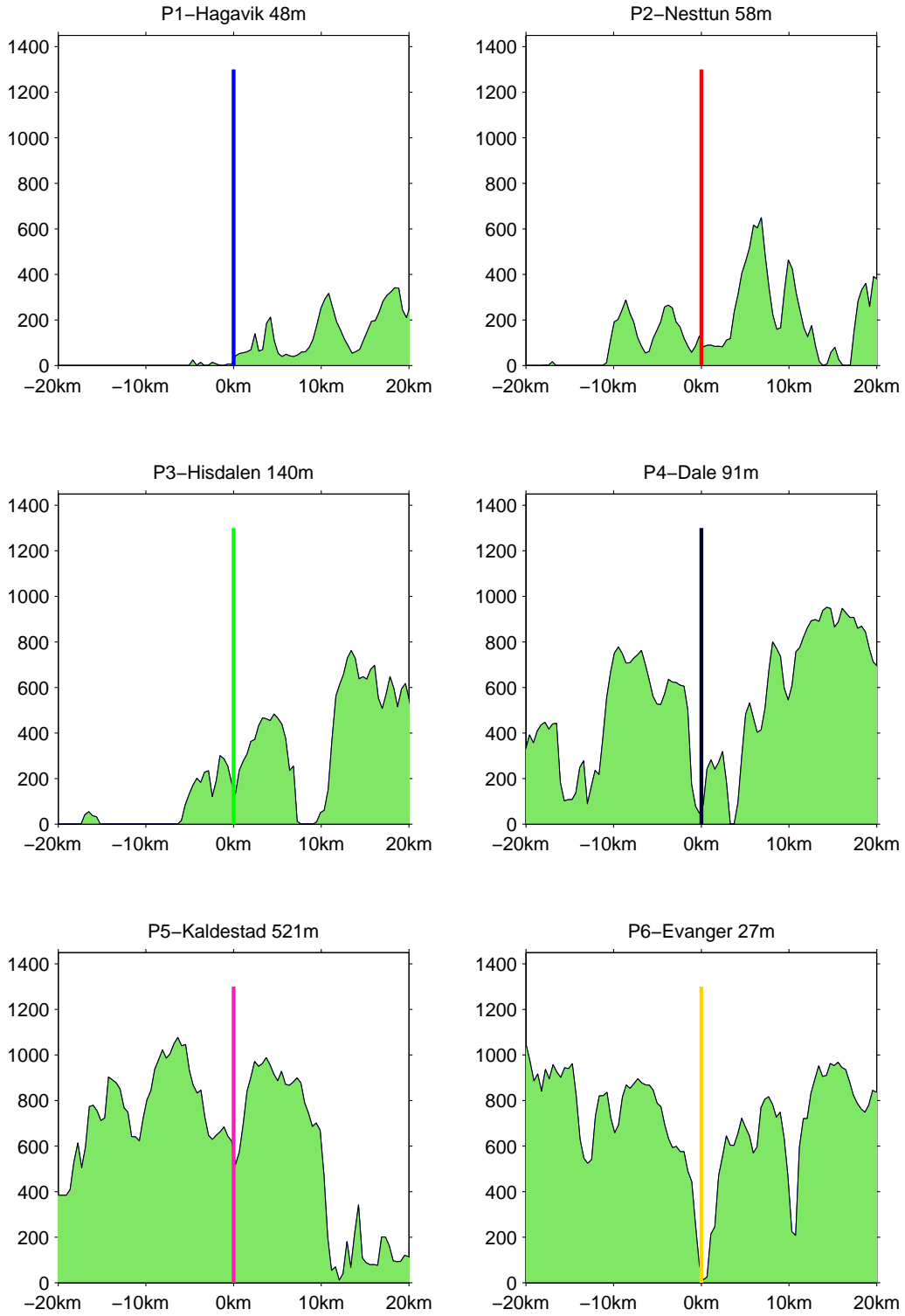**Profile direction 220° – 40°**
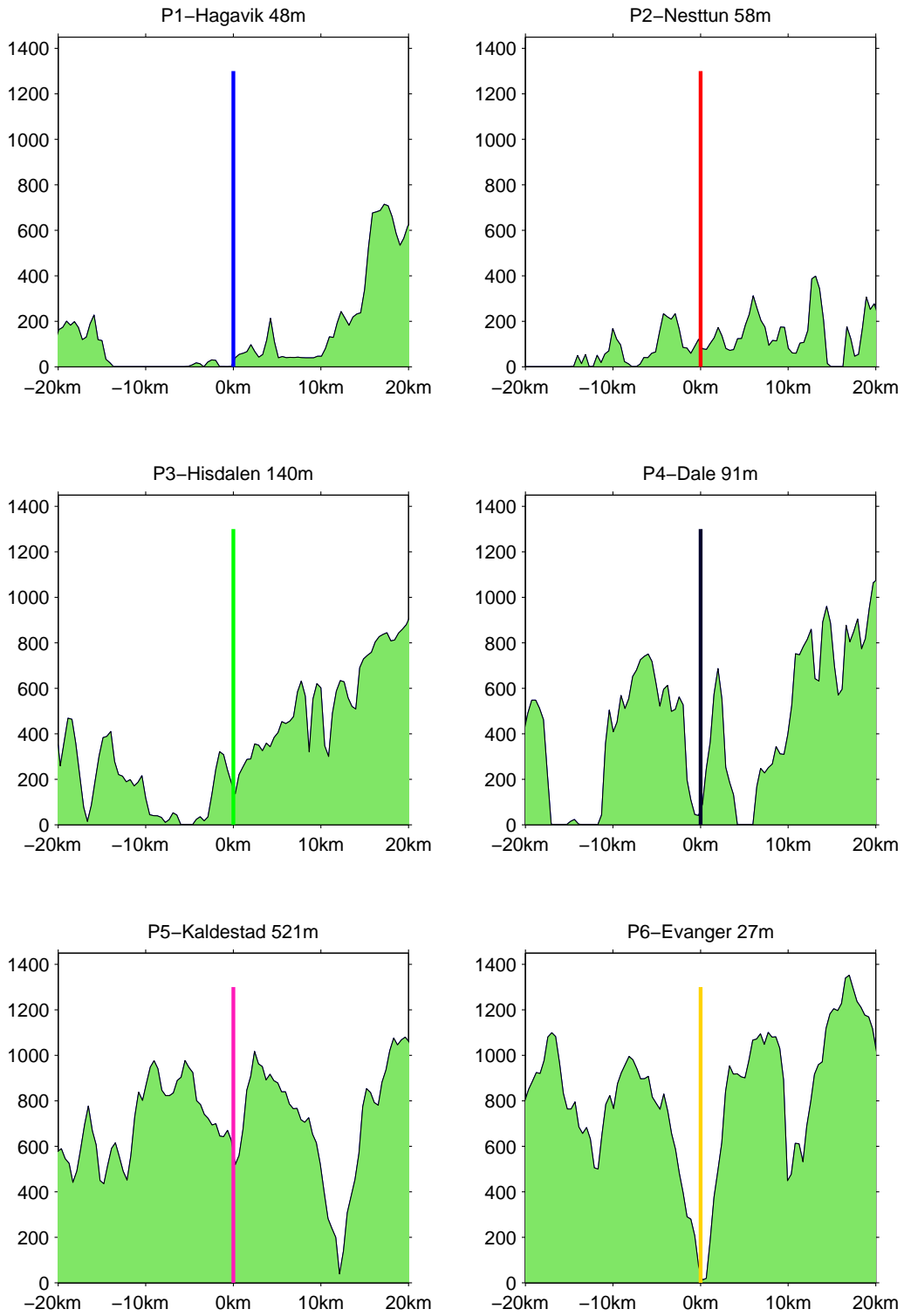

Figure B.3: Terrain profiles for stations P1-P6, direction is 220°.

Profile direction 220° – 40°

Figure B.3: Terrain profiles for stations P7-P12, direction is 220°.

100

Profile direction 230° – 50°

Figure B.4: Terrain profiles for stations P1-P6, direction is 230°.

Profile direction 230° – 50°

P7–Steine 485m

P8–Sandfjellet 620m

P9–Hodnaberg 618m

P10–Dyrvedalen 355m

P11–Flyane 436m

P12–Vasslii 79m

Figure B.4: Terrain profiles for stations P7-P12, direction is 230°.

Profile direction 240° – 60°

Figure B.5: Terrain profiles for stations P1-P6, direction is 240°.

Profile direction 240° – 60°
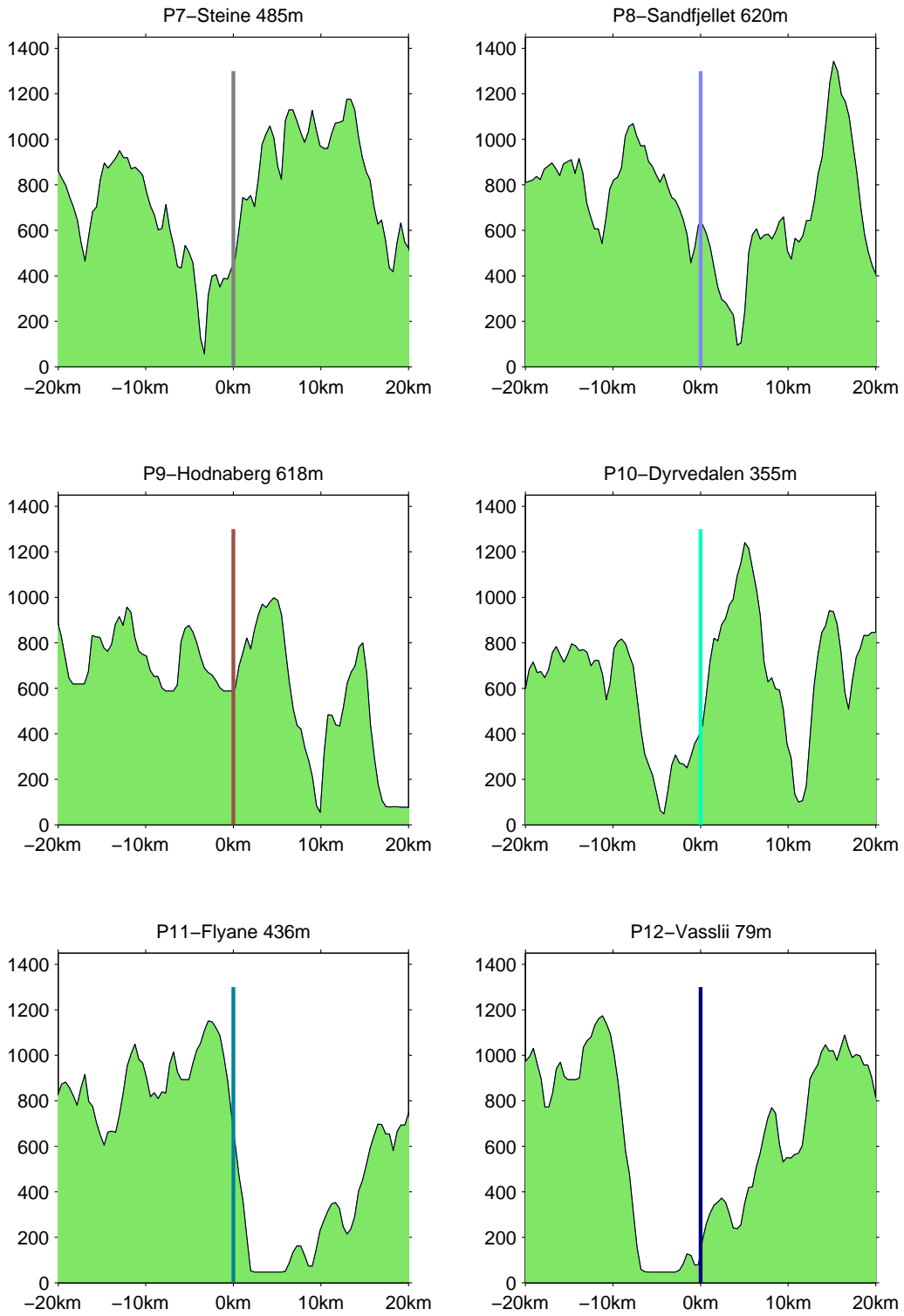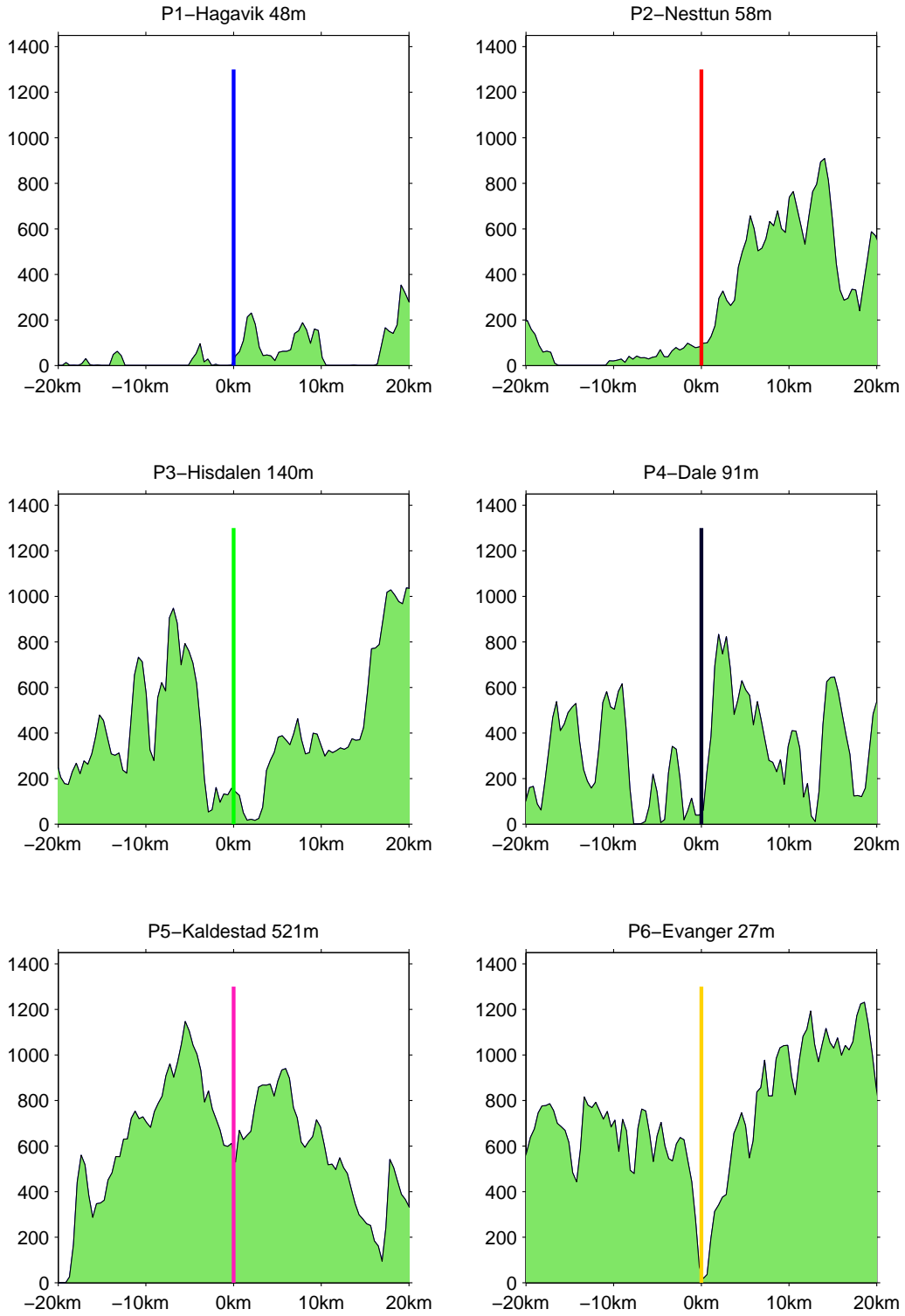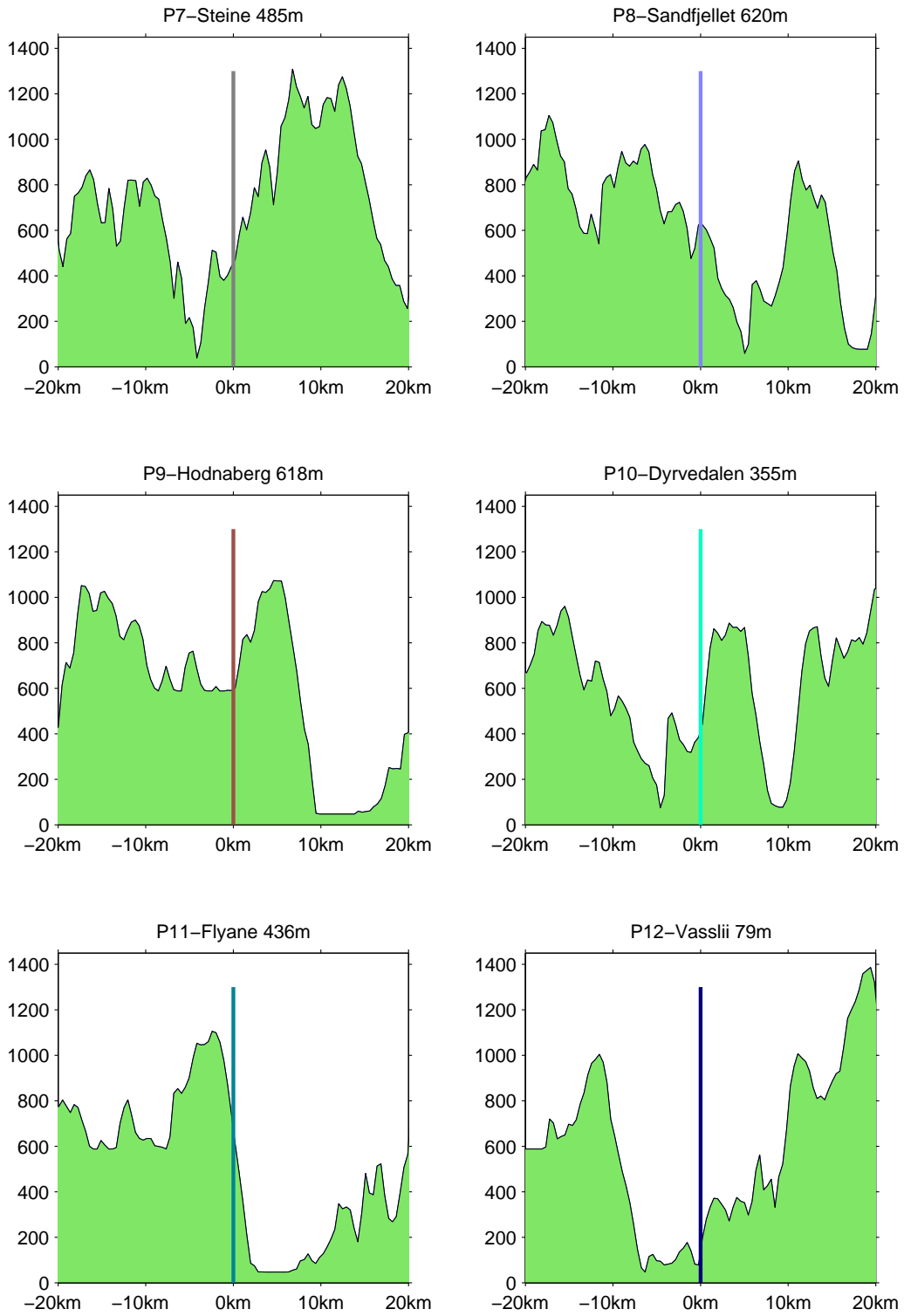
Figure B.5: Terrain profiles for stations P7-P12, direction is 240°.
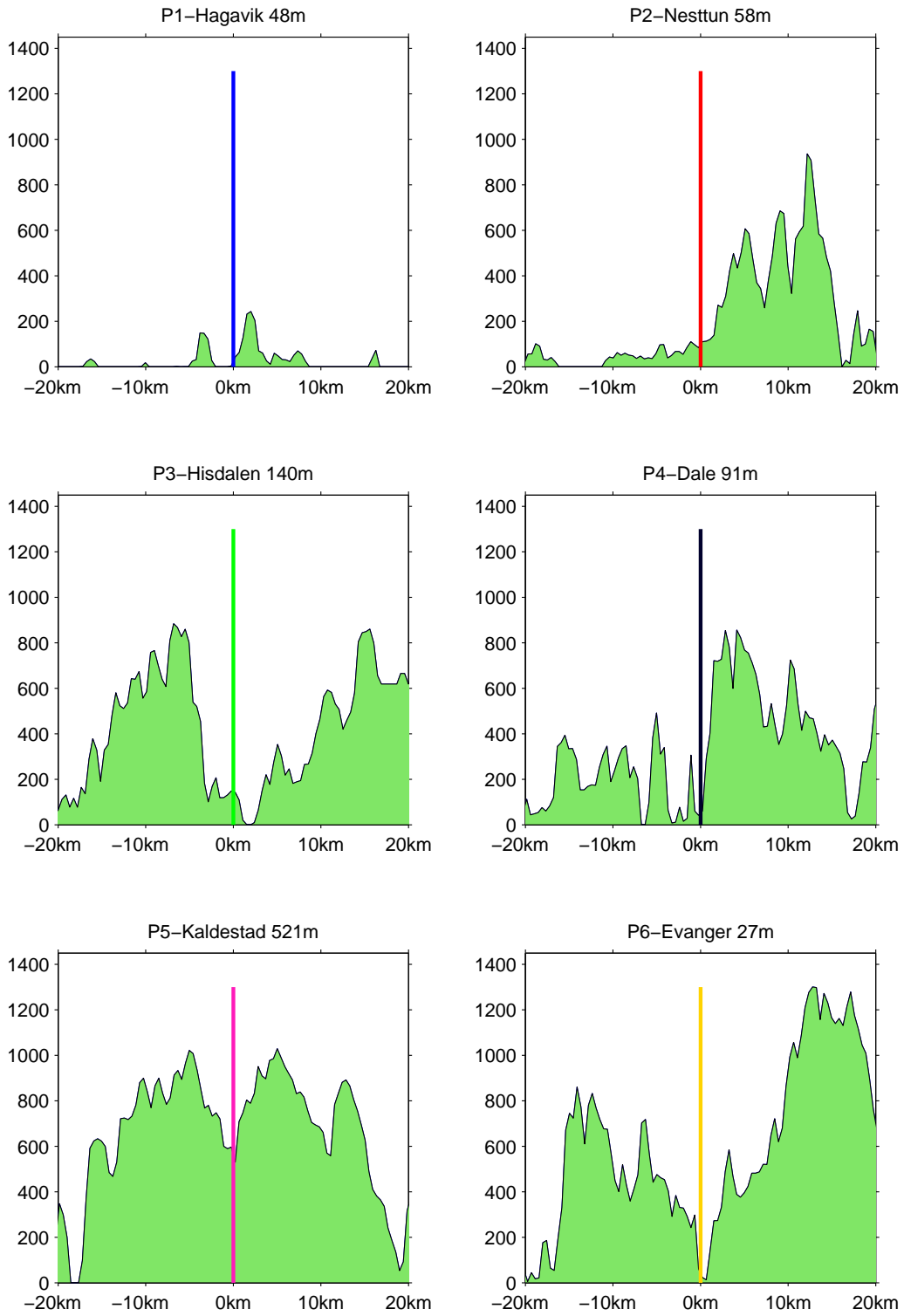
Profile direction 250° – 70°

Figure B.6: Terrain profiles for stations P1-P6, direction is 250°.

Profile direction 190° – 10°

Figure B.6: Terrain profiles for stations P7-P12, direction is 250°.

106

Bibliography

Alexandru, A., De Elia, R. and Laprise, R. (2009), 'Sensitivity study of regional climate model simulations to large-scale nudging parameters', *Monthly Weather Review* **137**, 1666–1686.

Barstad, I. and Caroletti, G. N. (2013), 'Orographic precipitation across an island in southern Norway: model evaluation of time-step precipitation', *Quarterly Journal of the Royal Meteorological Society* **139**(675), 1555–1565.

Barstad, I. and Smith, R. B. (2005), 'Evaluation of an orographic precipitation model', *Journal of Hydrometeorology* **6**(1), 85–99.

Colin, J., Déqué, M., Radu, R. and Somot, S. (2010), 'Sensitivity study of heavy precipitation in Limited Area Model climate simulations: Influence of the size of the domain and the use of the spectral nudging technique', *Tellus A* **62**(5), 591–604.

Colle, B. A. (2004), 'Sensitivity of orographic precipitation to changing ambient conditions and terrain geometries: An idealized modeling perspective', *Journal of the Atmospheric Sciences* **61**(5), 588–606.

Dee, D. P., Uppala, S. M., Simmons, a. J., Berrisford, P., Poli, P., Kobayashi, S., Andrae, U., Balmaseda, M. a., Balsamo, G., Bauer, P., Bechtold, P., Beljaars, a. C. M., van de Berg, L., Bidlot, J., Bormann, N., Delsol, C., Dragani, R., Fuentes, M., Geer, a. J., Haimberger, L., Healy, S. B., Hersbach, H., Hólm, E. V., Isaksen, L., Kå llberg, P., Köhler, M., Matricardi, M., McNally, a. P., Monge-Sanz, B. M., Morcrette, J.-J., Park, B.-K., Peubey, C., de Rosnay, P., Tavolato, C., Thépaut, J.-N. and Vitart, F. (2011), 'The ERA-Interim reanalysis: Configuration and performance of the data assimilation system', *Quarterly Journal of the Royal Meteorological Society* **137**(656), 553–597.

Dudhia, J. (1989), 'Numerical study of convection observed during the winter monsoon experiment using a mesoscale two-dimensional model', *Journal of the Atmospheric Sciences* **46**(20), 3077–3107.

Fagerlid, G. O. (2007), Small scale orographic precipitation: A study of phase I & II of the STord Orographic Precipitation EXperiment (STOPEX), Master's thesis, University of Bergen.

Glisan, J. M., Gutowski, W. J., Cassano, J. J. and Higgins, M. E. (2013), 'Effects of spectral nudging in WRF on Arctic temperature and precipitation simulations', *Journal of Climate* **26**(12), 3985–3999.

Habib, E., Lee, G., Kim, D. and Ciach, G. J. (2010), *Ground-based direct measurement, in rainfall: State of the science*, Vol. 191, American Geophysical Union.

Houze Jr., R. A. (2012), 'Orographic effects on precipitating clouds', *Review of Geophysics* **50**.

Hughes, M., Hall, A. and Fovell, R. G. (2009), 'Blocking in areas of complex topography, and its influence on rainfall distribution', *Journal of the Atmospheric Sciences* **66**(2), 508–518.

Janjic, Z. (2002), 'Nonsingular implementation of the Mellor-Yamada Level 2.5 scheme in the NCEP meso model', *National Centers for Environmental Prediction* p. 61.

Janjić, Z. I. (2000), 'Comments on "Development and evaluation of a convection scheme for use in climate models"', *Journal of the Atmospheric Sciences* **57**(21), 3686–3686.

Jiang, Q. (2003), 'Moist dynamics and orographic precipitation', *Tellus A* **55**(4), 301–316.

Kain, J. (2004), 'The Kain-Fritsch convective parameterization: an update', *Journal of Applied Meteorology* **43**(1980), 170–181.

Liu, P., Tsimpidi, a. P., Hu, Y., Stone, B., Russell, a. G. and Nenes, a. (2012), 'Differences between downscaling with spectral and grid nudging using WRF', *Atmospheric Chemistry and Physics* **12**(8), 3601–3610.

Medina, S., Smull, B. F., Houze, R. A. and Steiner, M. (2005), 'Cross-barrier flow during orographic precipitation events: Results from MAP and IMPROVE', *Journal of the Atmospheric Sciences* **62**(10), 3580–3598.

Mekonnen, G. B., Matula, S., Doležal, F. and Fišák, J. (2014), 'Adjustment to rainfall measurement undercatch with a tipping-bucket rain gauge using ground-level manual gauges', *Meteorology and Atmospheric Physics* **127**(3), 241–256.

Mellor, G. L. and Yamada, T. (1982), 'Development of a turbulence closure model for geophysical fluid problems', *Reviews of Geophysics* **20**(4), 851.

Mesquita, M. and Barstad, I. (2006), 'Precipitation downscaling on the west coast of Norway: Comparison with observational network', pp. 3–6.

Met.no (2015), 'http://sharki.oslo.dnmi.no/portal/page?_pageid=73,39035,73_39049&_dad=portal &_schema=PORTAL, accessed 12.02-2015'.

Miguez-Macho, G. (2004), 'Spectral nudging to eliminate the effects of domain position and geometry in regional climate model simulations', *Journal of Geophysical Research* **109**(D13), D13104.

Miguez-Macho, G. (2005), 'Regional climate simulations over North America: Interaction of local processes with improved large-scale flow', *Journal of Climate* **18**(8), 1227–1246.

Mlawer, E. J., Taubman, S. J., Brown, P. D., Iacono, M. J. and Clough, S. a. (1997), 'Radiative transfer for inhomogeneous atmospheres: RRTM, a validated correlated-k model for the longwave', *Journal of Geophysical Research* **102**(D14), 16663–16682.

Nešpor, V. and Sevruk, B. (1999), 'Estimation of Wind-Induced Error of Rainfall Gauge Measurements Using a Numerical Simulation', *Journal of Atmospheric and Oceanic Technology* **16**(4), 450–464.

Nugent, A. D., Smith, R. B. and Minder, J. R. (2014), 'Wind speed control of tropical orographic convection', *Journal of the Atmospheric Sciences* **71**(7), 2695–2712.

Omrani, H., Drobinski, P. and Dubos, T. (2012*a*), 'Optimal nudging strategies in regional climate modelling: investigation in a big-brother experiment over the European and Mediterranean regions', *Climate Dynamics* **41**(9-10), 2451–2470.

Omrani, H., Drobinski, P. and Dubos, T. (2012*b*), 'Spectral nudging in regional climate modelling: how strongly should we nudge?', *Quarterly Journal of the Royal Meteorological Society* **138**(668), 1808–1813.

Omrani, H., Drobinski, P. and Dubos, T. (2015), 'Using nudging to improve global-regional dynamic consistency in limited-area climate modeling: What should we nudge?', *Climate Dynamics* **44**(5-6), 1627–1644.

Onset (2001), Data logging rain gauge manual RG2 and RG2-M, Technical report, Onset Computer Corporation.

Pavelsky, T. M., Sobolowski, S., Kapnick, S. B. and Barnes, J. B. (2012), 'Changes in orographic precipitation patterns caused by a shift from snow to rain', *Geophysical Research Letters* **39**, L18706.

Pérez, J. C., Díaz, J. P., González, A., Expósito, J., Rivera-López, F. and Taima, D. (2014), 'Evaluation of WRF parameterizations for dynamical downscaling in the Canary Islands', *Journal of Climate* **27**(14), 5611–5631.

Reuder, J., Fagerlid, G. O., Barstad, I. and Sandvik, A. (2007), 'Stord Orographic Precipitation Experiment (STOPEX): an overview of phase I', *Advances in Geosciences* **10**, 17–23.

Roe, G. H. (2005), 'Orographic precipitation', *Annual Review of Earth and Planetary Sciences* **33**(1), 645–671.

Rogers, R. R. and Yau, M. K. (1989), *A short course in cloud physics*, 3. edn, Pergamon Press.

Sevruk, B., Ondrás, M. and Chvíla, B. (2009), 'The WMO precipitation measurement intercomparisons', *Atmospheric Research* **92**(3), 376–380.

Skamarock, W., Klemp, J., Dudhia, J. and Gill, D. (2008), A description of the advanced research WRF version 3, Technical report.

Skjerdal, M. S. (2009), Variability of precipitation in complex terrain and the investigation of representativeness of a single point measurement for the Matre Hydro System, Western Norway., Master's thesis, University of Bergen.

Smith, R. B. (1979), 'The influence on mountains on the atmosphere', *Advances in Geophysics* **21**, 87–230.

Smith, R. B. (1989), 'Mechanisms of orographic precipitation', *Meteorological Magazine* **118**(1401), 85–88.

Smith, R. B. (2003), 'A linear upslope-time-delay model for orographic precipitation', *Journal of Hydrology* **282**(1-4), 2–9.

Smith, R. B. and Barstad, I. (2004), 'A linear theory of orographic precipitation', *Journal of the Atmospheric Sciences* **61**(12), 1377–1391.

Spero, T. L., Otte, M. J., Bowden, J. H. and Nolte, C. G. (2014), 'Improving the representation of clouds, radiation, and precipitation using spectral nudging in the Weather Research and Forecasting model', *Journal of Geophysical Research* **119**(20), 11682–11694.

Stoelinga, M. T., Hobbs, P. V., Mass, C. F., Locatelli, J. D., Colle, B. a., Houze, R. a., Rangno, A. L., Bond, N. a., Smull, B. F., Rasmussen, R. M., Thompson, G. and Colman, B. R. (2003), 'Improvement of microphysical parameterization through observational verification experiment', *Bulletin of the American Meteorological Society* **84**, 1807–1826.

Sulen, I. Y. (2009), Predictability of precipitation in complex terrain. A comparison of high-resolution rain gauge measurements and fine-scale numerical simulations, Master's thesis, University of Bergen.

Tachikawa, T., Kaku, M., Iwasaki, A. and Gesch, D. (2011), ASTER Global Digital Elevation Model version 2 - Summary of validation results, Technical report, METI & NASA, 26pp.

Thompson, G. (2004), 'Explicit forecasts of winter precipitation using an improved bulk microphysics scheme. Part I: Description and sensitivity analysis', *Monthly Weather Review* **132**(2), 519–542.

Thompson, G., Field, P. R., Rasmussen, R. M. and Hall, W. D. (2008), 'Explicit forecasts of winter precipitation using an improved bulk microphysics scheme. Part II: Implementation of a new snow parameterization', *Monthly Weather Review* **136**(12), 5095–5115.

Warner, T. T. (2011), *Numerical weather and climate prediction*, Cambridge University Press, New York.

Weckwerth, T. M., Bennett, L. J., Jay Miller, L., Van Baelen, J., Di Girolamo, P., Blyth, A. M. and Hertneky, T. J. (2014), 'An observational and modeling study of the processes leading to deep, moist convection in complex terrain', *Monthly Weather Review* **142**(8), 2687–2708.

Wulfmeyer, V., Behrendt, A., Kottmeier, C., Corsmeier, U., Barthlott, C., Craig, G. C., Hagen, M., Althausen, D., Aoshima, F., Arpagaus, M., Bauer, H. S., Bennett, L., Blyth, A., Brandau, C., Champollion, C., Crewell, S., Dick, G., Di Girolamo, P., Dorninger, M., Dufournet, Y., Eigenmann, R., Engelmann, R., Flamant, C., Foken, T., Gorgas, T., Grzeschik, M., Handwerker, J., Hauck, C., Höller, H., Junkermann, W., Kalthoff, N., Kiemle, C., Klink, S., König, M., Krauss, L., Long, C. N., Madonna, F., Mobbs, S., Neininger, B., Pal, S., Peters, G., Pigeon, G., Richard, E., Rotach, M. W., Russchenberg, H., Schwitalla, T., Smith, V., Steinacker, R., Trentmann, J., Turner, D. D., Van Baelen, J., Vogt, S., Volkert, H., Weckwerth, T., Wernli, H., Wieser, A. and Wirth, M. (2011), 'The Convective and Orographically-induced Precipitation Study (COPS): The scientific strategy, the field phase, and research highlights', *Quarterly Journal of the Royal Meteorological Society* **137**, 3–30.